REPUBLIQUE DU CAMEROUN
Paix-Travail-Patrie

UNIVERSITE DE YAOUNDE I

CENTRE DE RECHERCHE ET DE FORMATION DOCTORALE EN SCIENCES, TECHNOLOGIES ET GEOSCIENCES

UNITE DE RECHERCHE ET DE FORMATION DOCTORALE EN PHYSIQUES ET APPLICATIONS

B.P 812 Yaoundé
Email: crfd_stg@uy1.uninet.cm

REPUBLIC OF CAMEROON
Peace-Work-Fatherland

THE UNIVERSITY OF YAOUNDE I

POSTGRADUATE SCHOOL OF SCIENCES, TECHNOLOGY AND GEOSCIENCES

RESEARCH AND POSTGRADUATE TRAINING UNIT FOR PHYSICS AND APPLICATIONS

P.O. Box 812 Yaoundé
Email: crfd_stg@uy1.uninet.cm

Laboratoire de Physique Nucléaire, Atomique, Moléculaire et Biophysique
Laboratory of Nuclear, Atomic, Molecular and Biophysics

DELAY-INDUCED OSCILLATIONS AND TRAVELLING WAVES IN THE FITZHUGH-NAGUMO NEURON WITH RELAXATION TIME

THESIS

Submitted in partial fulfillment of the requirements for the Degree of Doctor/PhD in Physics

Option: **Biophysics**

By

FORWAH AMSTRONG TAH

Registration Number: 12W1845

Master of Science in Physics

Supervisors

TABI Conrad Bertrand
Professor
Botswana International University of Science and Technology (BIUST)

And

KOFANE Timoléon Crépin
Professor
University of Yaoundé I

UNIVERSITE DE YAOUNDE I
UNIVERSITY OF YAOUNDE I

FACULTE DES SCIENCES
FACULTY OF SCIENCE

DEPARTEMENT DE PHYSIQUE
DEPARTMENT OF PHYSICS

ATTESTATION DE CORRECTION DE LA THESE DE DOCTORAT/Ph.D

Nous, Professeurs **BOUETOU BOUETOU Thomas, ZEKENG Serge Sylvain, DJUIDJE Kenmoe Germaine, FAUTSO KUIATE Gaétan** et Professeur **BOLIE Germain Hubert** , respectivement Examinateurs et Président du jury de la thèse de Doctorat/Ph.D de Monsieur **FORWAH Amstrong Tah** Matricule **12W1845**, préparée sous la co-direction du Professeur **KOFANE Timoléon Crépin** et du Professeur **TABI Conrad Bertrand,** intitulée : « **Delay-induced oscillations and travelling waves in the Fitzhugh-Nagumo neuron with relaxation time**», soutenue le **Mercredi, 21 Décembre 2022**, en vue de l'obtention du grade de Docteur/Ph.D en Physique, Spécialité **Physique des Rayonnements et Biophysique**, attestons que toutes les corrections demandées par le Jury de soutenance ont été effectuées.

En foi de quoi, la présente attestation lui est délivrée pour servir et valoir ce que de droit.

Fait à Yaoundé le ..... 12 JAN 2023 .....

Examinateurs

Pr. BOUETOU BOUETOU Thomas

Pr. ZEKENG Serge Sylvain

Le Président du Jury

Pr. BEN-BOLIE Germain Hubert

Pr. DJUIDJE Kenmoe Germaine

Pr. FAUTSO KUIATE Gaétan

Le Chef de Département de Physique

UNIVERSITE DE YAOUNDE I * FACULTE DES SCIENCES * DEPARTEMENT DE PHYSIQUE
Le Chef de Département

Professeur

Delay-induced oscillations and travelling waves in the Fitzhugh-Nagumo neuron with relaxation time

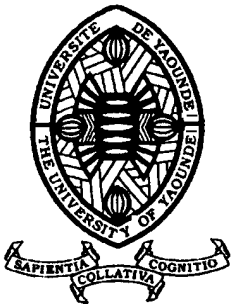

Forwah Amstrong Tah

Supervisors: Prof. T.C. Kofané
Prof. C.B. Tabi

Department of Physics
University of Yaounde I

This Dissertation is submitted in partial fulfillment of the requirements for the degree of
Doctor of Philosophy

Laboratory of Biophysics December 2022

I dedicate this thesis to all members of the Tah family.

Declaration

I hereby declare that except where specific reference is made to the work of others, the contents of this thesis are original and have not been submitted in whole or in part for consideration for any other degree or qualification in the university of Yaoundé I, or any other university. This thesis is my own work and contains nothing which is the outcome of work done in collaboration with others, except as specified in the text and Acknowledgements. This thesis does not exceed the prescribed word limit for the relevant Degree Committee.

Forwah Amstrong Tah
December 2022

Acknowledgements

I acknowledge the almighty creator, maker of all living and intelligent creatures.

A special thanks to my academic supervisors and reviewers ; Professors BEN-BOLIE Germain Hubert, Timoléon Crépin KOFANE, TABI Conrad Bertrand, BOUETOU BOUETOU Thomas, ZEKENG Serge Sylvain, DJUIDJE Kenmoe Germaine, FAUTSO KUIATE Gaéan, for their advice and critical analyses of thesis and the works from which this thesis was written. I thank Professor H. P. EKOBENA, chair of the Biophysics laboratory, for his guidance and management of the lab during my research studies.

I am grateful to the anonymous reviews of the publications derived from this work. I wish to thank Dr. DANG, Dr. ETEME, who have been very helpful in providing advice during my masters' thesis, and Dr. BELOBO, for organizing very informative seminars at the lab. I also wish to thank my classmates at the Biophysics laboratory who have been of tremendous moral support during my research studies.

Special thanks to my Mom, Angeline, my Dad, TAH Godlove, and my wife, Myriam for their love, advice, and care throughout my Ph.D. studies.

Abstract

Transmission delays are inherent to the propagation of nerve pulses across neural networks. For example, delays due to the relaxation time lead to finite propagation speeds along the neuron. In this thesis, we examined the effect of the time of relaxation on the stability and wave properties of a hyperbolic Fitzhugh-Nagumo neuron. We considered variants of the latter such as the continuous, discrete versions, and photosensitive variants.

We used multiple methods to establish the existence of delay-induced oscillations and study the effect of the time of relaxation on the wave properties of the system. We analyzed Hopf bifurcations and other relevant bifurcations using the center manifold theory, normal form reductions, and numerical continuation methods where suitable. Continuous hyperbolic models were discretized using finite differences. Analytical techniques were used to derive explicit solutions for fronts and oscillons of the wave system and study the influence of the time of relaxation on their profiles. Numerical simulations were used to study the synchronization of hyperbolic photosensitive neurons under different coupling schemes.

Our results can be summarized as follows: In the absence of diffusion, the time of relaxation induced Hopf bifurcations beyond a certain threshold. With diffusion in the system, the time of relaxation induced Hopf bifurcations of homogeneous and inhomogeneous-type. Furthermore, negative diffusion induces pitchfork bifurcations. The squared phase velocity of periodic and solitonic waves varies inversely with the time of relaxation. We showed that the amplitude of front waves is inversely proportional to the delay while that of the oscillon is directly proportional.The analyses of the discrete models showed that the local bifurcations exhibited by the continuous models are conserved by the corresponding discrete models. Results on the synchronization of hyperbolic photosensitive neurons showed that the prevalence of burst synchronization depends on the coupling scheme.

Keywords: Delay-induced oscillations, Relaxation time, Fitzhugh-Nagumo neuron, Patterns and waves

Résumé

Les retards de transmission sont inhérents à la propagation des impulsions nerveuses dans les réseaux neuronaux. Par exemple, les retards dus au temps de relaxation conduisent à des vitesses de propagation finies le long du neurone. Dans cette thèse, nous avons examiné l'effet du temps de relaxation sur la stabilité et les propriétés ondulatoires d'un neurone hyperbolique de Fitzhugh-Nagumo. Nous avons considéré des variantes de ce dernier telles que les versions continues, discrètes, et les variantes photosensibles.

Nous avons utilisé plusieurs méthodes pour établir l'existence d'oscillations induites par le retard et étudier l'effet du temps de relaxation sur les propriétés ondulatoires du système. Nous avons analysé les bifurcations de Hopf et d'autres bifurcations pertinentes à l'aide de la théorie des collecteurs centraux, des réductions de la forme normale et des méthodes de continuation numérique, le cas échéant. Les modèles hyperboliques continus ont été discrétisés à l'aide de différences finies. Des techniques analytiques ont été utilisées pour dériver des solutions explicites pour les fronts et les oscillons du système d'ondes et étudier l'influence du temps de relaxation sur leurs profils. Des simulations numériques ont été utilisées pour étudier la synchronisation des neurones photosensibles hyperboliques sous différents schémas de couplage.

Nos résultats peuvent être résumés comme suit : En l'absence de diffusion, le temps de relaxation induit des bifurcations de Hopf au-delà d'un certain seuil. Avec la diffusion dans le système, le temps de relaxation induit des bifurcations de Hopf de type homogène et inhomogène. De plus, une diffusion négative induit des bifurcations de type fourche. La vitesse de phase quadratique des ondes périodiques et solitoniques varie inversement au temps de relaxation. Nous avons montré que l'amplitude des ondes frontales est inversement proportionnelle au délai alors que celle de l'oscillon est directement proportionnelle.Les analyses des modèles discrets ont montré que les bifurcations locales exhibées par les modèles continus sont conservées par les modèles discrets correspondants. Les résultats sur la synchronisation des neurones photosensibles hyperboliques ont montré que la prévalence de la synchronisation des salves dépend du schéma de couplage.

Mots clés : Oscillations induites par le retard, temps de relaxation, neurone de Fitzhugh-Nagumo, motifs et ondes.

Contents

List of Figures

List of Tables

General introduction

In this thesis, we study the effect of the time of relaxation, induced by the finite speed of propagation, on the dynamics of a hyperbolic Fitzhugh-Nagumo (FHN) nerve model. More precisely, we study its role in the emergence of diverse bifurcation phenomena connected to traveling and stationary waves, mixed-mode oscillations, bistability, chaos, and a host of other dynamics. Furthermore, the effect of this time lag on the velocity profiles of traveling waves in the oscillatory and excitable regimes of the modified nerve model is studied. The aforenamed dynamics are conserved in a corresponding nerve model with space and time discretizations.

Signal transmission in spatially extended systems or systems with feedback is often accompanied by delays in transmission[1]. Shortly after scientists were successful in modeling natural phenomena via dynamical systems, it became necessary, where applicable, to extend these models to take into account delays. Such extensions often yield more realistic models which go beyond the simple qualitative description of the phenomenon at hand. In the propagation of action potentials across a network of neurons, delays occur naturally, during signal transmission along the nerve cable and during transmission at the synapse. Time delays are also present in networks of neurons in the peripheral nervous system such as the balance control system[2]. Delays may also occur when populations of neurons communicate with each other. Experiments reports that the magnitude of the delays between different regions of the brain is of the order of 10ms or more [3]. This value may vary depending on the conduction distance and velocity of propagation. Bigger delays may be involved in nonlocal interactions such as long-range coupling observed in neurons [4–6] and in propagation in unmyelinated intracortical neurons [7]. Roughly 20-40% of axons have a fine or absent myelin coating [8]. Demyelination in axons can sometimes result in a pathology known as multiple sclerosis (MS), where the lower conduction velocities lead to large propagation delays and ultimately propagation failure [9, 3]. Other pathologies related to propagation delays include Parkinson's disease and epilepsy. As such models of spatially extended neurons with delays may be suitable in modeling the dynamics of intracortical

neurons where lack of myelination leads to lower propagation velocities and ultimately larger delays.

A known phenomenon associated with delayed systems is delay-induced instability [8]: An occurrence whereby the steady solutions of the dynamical system become unstable to oscillatory and stationary bifurcations, beyond a threshold value of delay. Delay-induced instability is well-known in dynamical systems where it often leads to a Hopf bifurcation [10]. This corresponds to the appearance of a pair of purely imaginary roots of the characteristic equation. Multiple methods have been developed to determine the direction of the Hopf bifurcation and as a result, the stability of the periodic orbit[11–13]. Throughout most of this thesis, we make principal use of the center manifold reduction[14, 15] to assess the stability of the periodic orbit. A simple demonstration of delay-induced oscillations was studied by Plant et al.[16] who studied a delayed Fitzhugh-Nagumo (FHN) model with recurrent feedback. Junyi et al.[17] studied the critical values of delay for a system of two coupled FHN models. Delay-induced oscillations may also depend on the network architecture[18]. Time delays may also lead to the death of oscillations—a phenomenon known as amplitude death, multistability, delay-induced chaotic oscillations, and much more [8]. The mechanisms underpinning the creation of Periodic oscillations either in the form of large-amplitude periodic action potentials or small-amplitude waves are important in helping neuroscientists understand brain function and dysfunction. Small-amplitude oscillations—typical of those born via a supercritical Hopf bifurcation, play a vital role in synchronization by increasing the firing probability of neurons via subthreshold depolarization[19].

Classical models of delay differential equations are inherently infinite-dimensional and their solutions exist in some continuous function space. As a result, their analysis is quite involved. In this thesis, we study the impact of delay on an infinite-dimensional delay differential equation of hyperbolic type. In this case, the infinite-dimensional character arises only due to the diffusion term. The hyperbolic formulation is based on the Maxwell-Cattaneo modification of wave propagation [20], with finite speed effects. Although hyperbolic models of nerve propagation have been around for a long time[21], there seems to be a renewed interest in them as evidenced in recent publications[22–24], wherein the effect of the time of relaxation (delay) on the profile and stability of the action potential has been addressed. However, in these studies, the authors did not examine the effect of the relaxation time on the stability of fixed points of the system— the main subject of this thesis.

The general objectives for our research were as follows: firstly, we studied the impact of the time of relaxation and diffusion on the stability of the hyperbolic Fitzhugh-Nagumo model. Secondly, we assessed the nature and stability of these bifurcations including bifurcations of codimension-1 and -2. Thirdly, discretized the hyperbolic model to verify if the bifurcations

detected in the continuous model were preserved in the corresponding discrete models. Lastly, we investigate the impact of the time of relaxation on the profiles of front and oscillon waves of the system.

The outline of the rest of this thesis is as follows: In Chapter 1 we review the structure and function of neurons, neural coupling, as well as action potential generation and propagation. This is followed by a review of the classical Fitzhugh-Nagumo(FHN) model, hyperbolic formulation of diffusion, classical modeling of delays, and multiple local bifurcations of codimension-one and two, relevant to this thesis. We conclude this chapter with a brief review of bursting dynamics near a Bautin bifurcation. In Chapter 2 we review the hyperbolic Fitzhugh-Nagumo model and its variants. We also review the main methods (Analytical and numerical) used throughout this thesis and their applications. In Chapter 3 we present the main results of this thesis. These include results on the Hopf and Pitchfork bifurcations, exact front and oscillon solutions of the hyperbolic Fitzhugh-Nagumo model, and burst synchronization in two coupled photosensitive hyperbolic Fitzhugh-Nagumo models. We summarize our main findings in a general conclusion immediately after Chapter 3, in which we provide an outlook for future research our the applicability of our results.

Chapter 1

Review of models of neural spiking, bifurcations and normal forms

In this chapter, we review the neuron as the structural and functional unit of the nervous system. We provide a brief summary of the mechanism of generation of action potentials and their transmission from one neuron to the next. We also review briefly, some of the classical mathematical models of neurons from the point of view of dynamical systems, and discuss some of the bifurcation mechanism leading to periodic spiking, bursting, and traveling waves. Our discussion is restricted to conductance based models similar to the Hodgkin-Huxley(HH) model. We give a brief account of the properties of the Fitzhugh-Nagumo (FHN) model in relation to its oscillatory and excitability properties. We review the hyperbolic formulation of diffusion based on the Maxwell-Cattaneo formulation.

This chapter is structured as follows: In section 1.1, we give a brief literature review of the subject of modeling neurons and consider the state-of-the art. Section 1.2 gives a review of the structure of the neuron and the mechanisms of generation of action potentials. Section 1.3 considers the celebrated Hodgkin-Huxley (HH), and the classical Fitzhugh-Nagumo (FHN) models. This section also features a discussion on classical ways of modeling delays and the significance of the time of relaxation. Section 1.4 reviews the main bifurcations of codimension-one and -two, encountered in this thesis and concludes by discussing common mechanisms of bursting in neurons. A conclusion to the chapter is provided in section 1.5.

1.1 Introduction and background

The topic of mathematical modeling neurons via dynamical systems is very old and dates back to the early 1990's. It was midway into that century, precisely in 1952, that a successful

quantitative description of nerve impulse generation was given. This was the fruit of the works of Hodgkin and Huxley [25]. Following the success of the Hodgkin-Huxley model, a wealth of vector field-based models have been developed to address different qualitative (quantitative) features of neural spiking. These models can generally be classified as integrate and fire models [26], resonate and fire models [27], spike rate and mean field models [28]. Based on their bifurcation to periodic spiking, models of neurons may further be classified as models of bifurcation-type 1 and models of bifurcation-type 2 [29]. Models of neurons have also been modified to take into account stochastic phenomena [30–32] and recently delays have been included into these models to give a more realistic perspective on signal propagation in neural networks [33, 34]. It is often handy to reduce the dimension of the vector field of a given neural model. This is especially true if the vector field consists of hundreds or more, coupled neurons. Such reductions may lighten the computational burden of simulating such a system or ease analytical manipulations. In fact, the Fitzhugh-Nagumo model was proposed as a lower dimensional reduction of the Hodgkin-Huxley model, making it more tractable to mathematical manipulations. A common pattern employed over the decades has been the amplitude [35] and phase reduction [36] approaches in which the system is reduced to a lower dimensional manifold with the amplitude or phase as the main dynamical variable. In such a setting, the dynamics of the higher dimensional manifold can be inferred in the lower dimensional system. Near a bifurcation, a system can generally be reduced to a lower dimensional manifold known as the normal form of that bifurcation.

Bursting is a behavior sometimes exhibited by neurons in which groups of action potentials (spikes) are fired in quick succession followed by periods of quiescence[37]. Believed to have greater chances of crossing a synapse than a single spike, and to be a vehicle for complex information encoding, neural bursting continues to be an active area of research [38]. From a physiological standpoint, the transition from repetitive spiking to quiescence can be construed as a hyperpolarization current that gradually strengthens during spiking or a depolarization current that weakens during spiking. Examples of such currents include: the calcium-dependent currents [39], and M-current [40]. From a dynamical systems point of view, bursting is a manifestation of bistability in a system in which a system switches from a limit cycle motion to a fixed point. If this happens periodically then periodic bursting occurs. A standard model used to demonstrate spiking and bursting in neurons in which one of the aforementioned currents have been taken into account is the Hindmarsh-Rose neuron model[41]. Bursting may be initiated via a plethora of dynamical scenarios[29], corresponding to different types of bursting, some of which have been observed experimentally[42]. In this thesis, we focus on bursting around the Bautin bifurcation[43]; often called elliptic

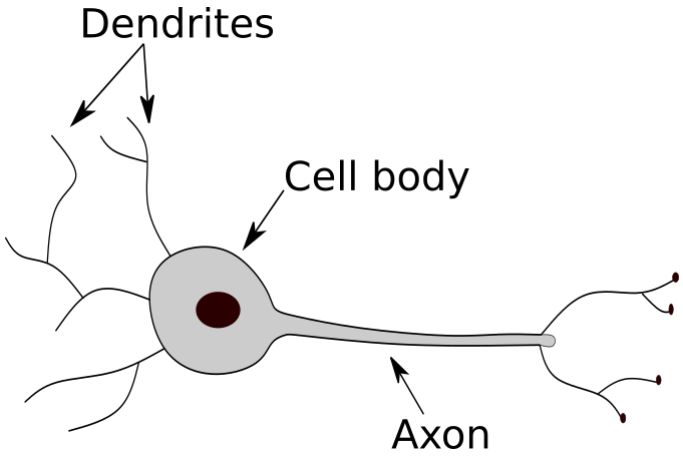

Figure 1.1 Caricature of a typical neuron, showing its main parts.

bursting. Here, bursting is initiated via a subcritical Hopf bifurcation and terminated via a fold bifurcation.

1.2 The neuron, structure and function

The brain is and for a long time, has been one of the most complex human organs ever studied by man. The average human brain consist of approximately one hundred billion neurons and a smaller number of glial cells [37]. Although the neurons in the brain represent a large chunk of all neurons in the nervous system, neurons are found almost everywhere in the body where sensitivity to stimulus is present. Ramon Cajal, in the nineteenth century [44], was the first to observe and describe the structure of the neuron. The neuron as we know it today is made up of three major parts; the cell body, axon, and dendrites (see Fig.1.1). Four major ions bathe in the intra- and extracellular contents of the neuron; sodium (Na^+), (K^+), calcium (Ca^{2+}), and chloride (Cl^-) ions. In the absence of a stimulus, the distribution of these ions across the cell membrane of the axon is uneven. This is in part due to passive, and active diffusion. Ions diffuse across the membrane via selective ion channels, some of which are specific to a single ion type. While passive diffusion occurs as substances naturally diffusive down their concentration gradients, active diffusion, is mediated by ion pumps located at various ion channels. The difference in concentrations of ions across the membrane results in a potential difference across the cell known as the resting potential. Fig.1.2 shows the concentration of ions across the membrane at rest. The concentrations of the various ions is as follows: $[Na^+]_{ex} \gg [Na^+]_{in}$, $[K^+]_{ex} \ll [k^+]_{in}$, $[Cl^+]_{ex} \gg [Cl^+]_{in}$, and $[Ca^{2+}]_{ex} \gg [Ca^{2+}]_{in}$. Here $[X]_{ex,in}$ refers to the concentrations in the extracellular and

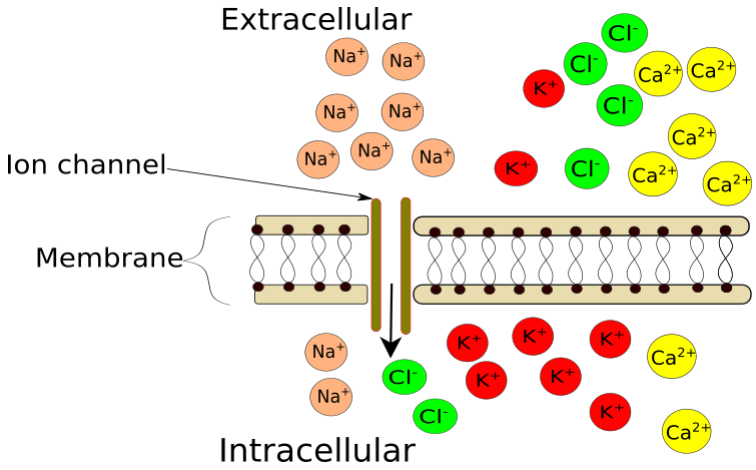

Figure 1.2 Distribution of ions across the membrane of the neuron at rest

intracellular contents of the species X. The numerical value of the resting potential of a typical neuron at rest is estimated to be $-70mV$; mV denoting millivolts.

The neuron is classified as an excitable cell because its membrane potential may experience brief voltage spikes in the presence of stimuli of sufficient strength. Such large excursions of the membrane potential, from the rest potential are called action potentials. Skeletal muscle cells, cardiac cells, and sensory cells are other examples of excitable cells. Because the stimulus must be of sufficient strength to elicit a spike in voltage, such cells are often referred to as "all-or nothing" cells. Fig.1.3 depicts the main steps involved in action potential generation and propagation in time. The generation of an action potential can be summarized in the following five steps:

1. **Resting**: At this stage, the cell is at the resting potential, $-70mV$.
2. **Depolarization**: When the cell is stimulated, the membrane potential may become more negative or positive. A stimulus is said to be *depolarizing* when it increases the membrane potential and *hyperpolarizing*, if it makes the membrane potential more negative. If a depolarizing signal drives the membrane potential past the threshold potential (approximately $-55mV$), Na^+ rush into the cell causing the potential to become more depolarized till it reaches a peak value of approximately $40mV$. This phase is known as the depolarization phase.
3. **Repolarization**: During this phase, Na^+ channels close and K^+ channels open and K^+ rushes out of the cell, hyperpolarizing the potential past the resting potential.
4. **Hyperpolarization**: At this stage, K^+ channels close and the potential begins a slow return to steady state. During this phase, the cell is unexcitable.
5. **Return to rest**: The potential returns to rest and the cell is once again excitable.

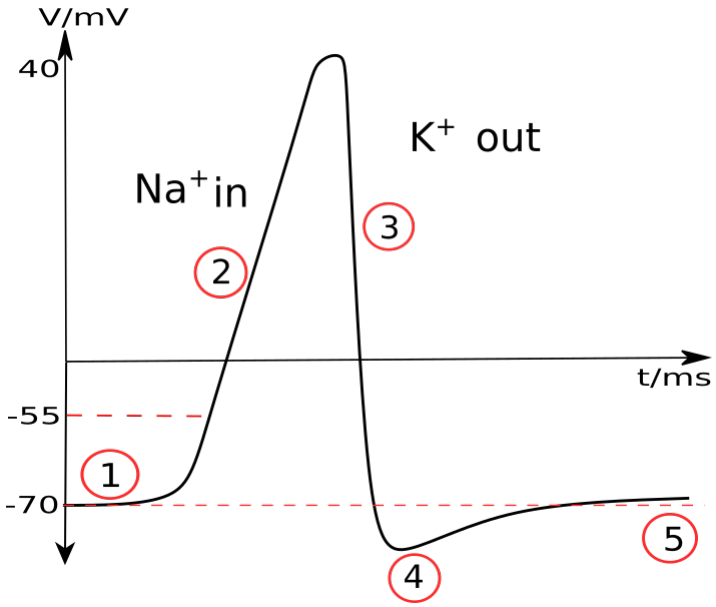

Figure 1.3 Main steps involved in action potential generation and propagation

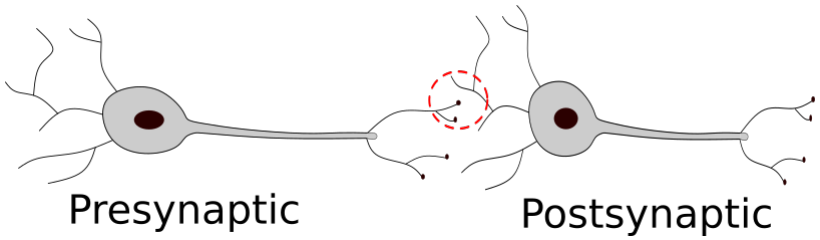

Figure 1.4 Sketch of pre- and post-synaptic neurons showing synapse in the red dashed circle.

Action potentials are usually generated beside the cell body in a location known as the axon hillock. Once they are generated, they travel down the length of the axon until they reach the axon terminals. These terminals are usually in close contact with the dendrites of other neurons. In such an arrangement, it is customary to refer to the neuron with the incoming spike as the *pre-synaptic* neuron and the receiving neurons are the *post-synaptic* neurons. The cleft between the axon terminals of one neuron and the dendrites of the next neuron is called the *synapse*, see Fig.1.4. Action potentials transit from the pre- to the post-synaptic neurons in two major ways; via chemical mediation or via direct contact. Synapses based on the former mode are called chemical synapses while those based on the latter are known as gap junction synapses. Chemical synapses depend on substances known as *neurotransmitters* for their function. In general, the pre-synaptic action potentials may trigger an *excitatory* or *inhibitory* response on the post-synaptic neuron. As such synapses are classified as excitatory

or inhibitory depending on the type of neurotransmitter released. Examples of excitatory and inhibitory synapses are glutamate and GABA (gamma-aminobutyric acid) respectively.

1.3 Conductance-based models of single neurons

Since the seminal work by Hodgkin and Huxley on the quantitative modeling of nerve pulse propagation in the giant squid axon, dozens of models known as “conductance-based" models have been proposed to model excitable cells in cardiac tissue, neurons, skeletal muscles and many more. In such models the capacitance of the excitable membrane is due to the charge separation across the membrane due to active and passive diffusion processes. When combined with ionic currents from several gated channels, the entire setup can be viewed as a capacitor in parallel with ionic channels, amenable to electrical circuit analysis. The Hodgkin-Huxley(HH) model has been successfully extended to model other types of neurons from the Reduced Traub-Miles Model (RTM), Wang-Buzsaki (WB) and Erisir models of rodent brains [37] to bursting pacemaker neurons in mammals [45].
In the presence of space-clamping, conductance-based models take the form:

$$\begin{aligned} C\dot{v} &= I_g(v,\mathbf{n}) + I_b + I_s(t) \\ \dot{\mathbf{n}} &= G(v,\mathbf{n}), \end{aligned} \tag{1.1}$$

where C is the capacitance of the membrane, v is the transmembrane potential, I_g is the sum of membrane currents, I_b is the constant baseline current, I_s is the stimulating current, $\mathbf{n}$ is the vector of gating variables and G is some vector field.
In the absence of space-clamping, the membrane membrane potential and gating variables depend on space. In this case a depolarization at a given location —an increase in the membrane potential, causes sodium channels in neighboring spatial locations to open while they are closed at the original location with the opening of potassium channels. As a result the membrane potential diffuses as a pulse. This diffusion is accounted for by the addition of a spatial term v_{xx} on the right hand side of Eq.(1.1). If the recovery phase of the membrane potential is neglected, the depolarization travels as a front.

1.3.1 The classical Hodgkin-Huxley model

The celebrated Hodgkin-Huxley (HH) equations take the general form:

$$C\dot{V} = I_b + I(t) - \bar{g}_{Na}h(V - V_{Na})m^3 - \bar{g}_K(V - V_K)n^4 - \bar{g}_L(V - V_L), \tag{1.2}$$
$$\dot{m} = \alpha_m(V)(1-m) - \beta_m(V)m, \tag{1.3}$$
$$\dot{h} = \alpha_h(V)(1-h) - \beta_h(V)h, \tag{1.4}$$
$$\dot{n} = \alpha_n(V)(1-n) - \beta_n(V)n, \tag{1.5}$$
$$\alpha_m(V) = 0.1(V+40)/(1-exp(-(V+40)/10)), \tag{1.6}$$
$$\beta_m(V) = 4exp(-(V+65)/18), \tag{1.7}$$
$$\alpha_h(V) = 0.07exp(-(V+65)/20), \tag{1.8}$$
$$\beta_h(V) = 1/(1+exp(-(V+35)/10)), \tag{1.9}$$
$$\alpha_n(V) = 0.01(V+55)/(1-exp(-(V+55)/10)), \tag{1.10}$$
$$\beta_n(V) = 0.125exp(-(V+65)/80). \tag{1.11}$$

Here, $V_{Na} = 50mV$, $V_K = -77mV$, $V_L = -54.4mV$ are the reversal potentials of the sodium , potassium and leakage channels respectively. $\bar{g}_{Na} = 120mS/cm^2$, $\bar{g}_K = 36mS/cm^2$, $\bar{g}_L = 0.3mS/cm^2$ are their respective conductances. The membrane capacitance has value $C = 1\mu F/cm^2$. It should be noted that the membrane potential as described in the original paper by Hodgkin and Huxley is related to that of Eq.(1.1) by $V_{HH} = -v + V_{eq}$, where V_{eq} is the equilibrium potential. It is self evident that the HH model as is presented here does not really lend itself to analytical manipulations. As such various two-dimensional reductions are usually sought: the so-called "slow-fast reductions". Examples of slow fast reductions derived from the HH model include the 2D-Hodgkin-Huxley model [44] and the FHN model which we explore in detail in the next subsection.

1.3.2 The classical Fitzhugh-Nagumo model

A popular two-dimensional neuron model derived from the HH model by exploiting the existence of different time scales, is the Fitzhugh-Nagumo model [46, 47]. In its general, dimensionless form, the FHN model takes the form:

$$\dot{u} = f(u,v) + I \tag{1.12}$$
$$\dot{v} = \varepsilon g(u,v), \tag{1.13}$$

where the variable u is known as the fast variable, v the slow variable, in reference to the scaling factor ε in its vector field, and I the external stimulating current. The functions $f(u,v)$ and $g(u,v)$ determine the dynamics of the model; their zeros determine the quality and quantity of equilibria located in the system. The function f can vary depending on the variant of the FHN model being considered. We note the classic form

$$f(u,v) = Au(u-\alpha)(1-u) - v, \tag{1.14}$$

with $0 < \alpha < 1$, as well as the McKean form :

$$f(u) = H(u-\alpha) - u - v, \tag{1.15}$$

where H is the Heaviside function. The latter form is suitable for a piece-wise construction of analytical solutions. In this study we shall use the forms:

$$f(u,v) = u - \frac{u^3}{3} - v, \tag{1.16}$$

$$g(u,v) = u + a - bv, \tag{1.17}$$

from Ref.[48], where a and b are constants.
Although simpler than the HH model, the FHN can reproduce some of the key features of the HH model, including propagation of nerve pulses in space. Other variants of the FHN model include the Van der pol oscillator [49].
We shall briefly review some of the key behaviors of the classical FHN as a fucntion of I, and its nullclines $f(u,v) = 0$ and $g(u,v) = 0$, by exploring its phase plane dynamics. Consider the FHN model:

$$\dot{u} = u - \frac{u^3}{3} - v + I, \tag{1.18}$$

$$\dot{v} = \varepsilon(u + a - bv), \tag{1.19}$$

with $I = 0$. Fig.(1.5) shows the three different ways in which the nullclines of the system can intersect; corresponding to a maximum of up to three equilibria. The cubic (N-shaped) nullcline corresponds to $f(u,v) = 0$ while the monotone nullcline corresponds to $g(u,v) = 0$. For each intersection the system can have either mono(bi)- stable excitable or oscillatory kinetics:

— In Fig.(1.5.a), the two nullcines intersect on the left side (but close to) the minimum of the cubic nullcline. If the resulting equilibrium is stable, then strong perturbations

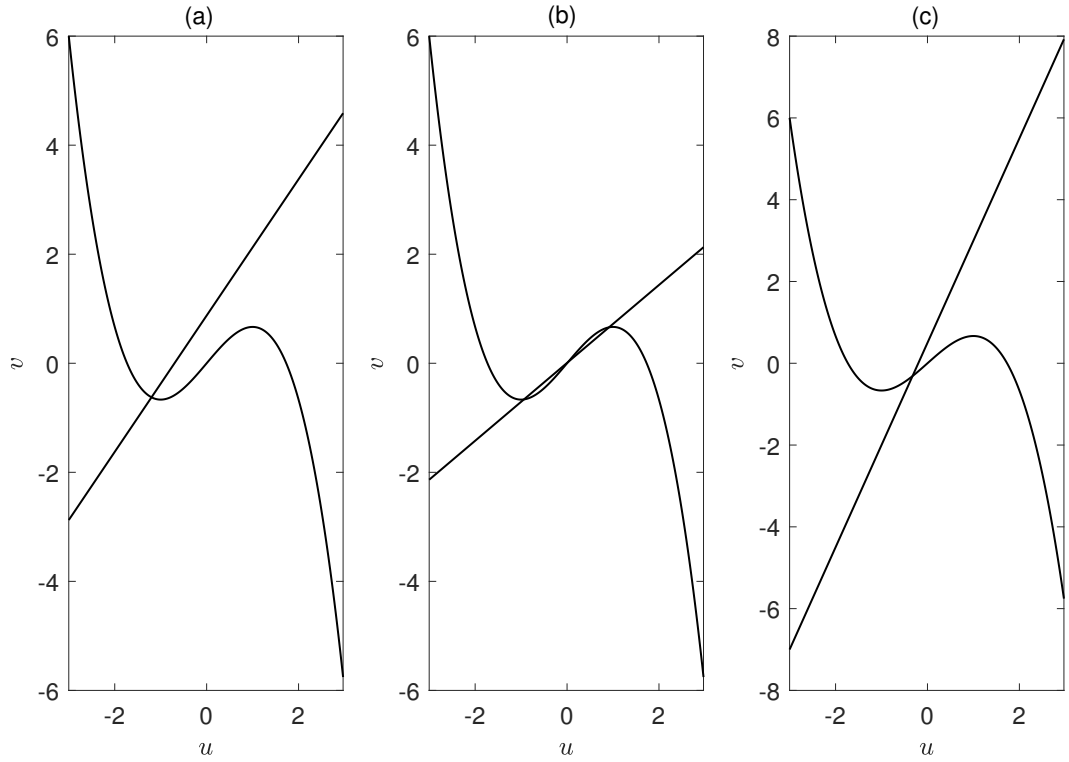

Figure 1.5 Nullclines of the classical FHN system showing three different ways in which the curves $f(u,v) = 0$ and $g(u,v) = 0$ intersect. Setting: (a) $a = 0.7$, $b = 0.8$ could result in a monostable excitable system , (b) $a = 0.01$, $b = 1.4$ with possible bistable excitable kinetics and (c) $a = 0.2$, $b = 0.4$, may result in oscillatory kinetics. For all plots $I = 0$.

around this equilibrium might drive the system into a large excursion around the phase plane and back to the starting point. This excitable behavior might lead to a traveling pulse (action potential) in the corresponding spatially extended system.

— In Fig.(1.5.b), the nullclines intersect at three different points which are monotonically increasing in the v-variable: $v_1 < v_2 < v_3$. It is usually the case that the equilibria with v_1 and v_3 are stable while that with v_2 is unstable. In this case, a heteroclinic orbit may be formed connecting v_1 and $v_3$or connecting $v_1(v_3)$ and v_2. This heteroclinic orbit corresponds to a travelling front or shock wave.

— In Fig.(1.5.c), the nullcines intersect on the right side of the minimum of the cubic nullcline. Under parameter variation, this equilibrium may become unstable and surrounded by a stable limit cycle. This limit cycle corresponds to periodic oscillations in the space-clamped model and to periodic traveling waves in the model with diffusion.

1.3.3 Modeling delays in neuron models

The evolution of a dynamical system need not only depend on the current state of the system but could also depend on its history. For example, in a predator-prey system, the growth rate of a species may depend on the current availability of food and also on the past quantities of food [50]. Other systems where such a dependence may be obvious include: feedback control systems [51], where information is processed and transmitted at finite speeds, human motion control systems with reflex delays [52] and in neural networks [53]. The dependence of a system on its history is usually expressed as a delayed term. In order to account for propagation delays, three main approaches have been adopted over the years: The addition of a constant delay term through a hyperbolic time derivative due to Cattaneo [54–56], the space dependent delay of neural fields [57, 58], and constant state dependent delay [59]. The first approach has been extensively applied to model extended irreversible thermodynamics [60], Bernard convection [61] and much more [62, 63]. Depending on the nature of the delay term, the resulting delay differential equation may belong to one of the following three types [64]: retarded functional differential equations (RFDE) or simply delay differential equations (DDE), in which the rate of change of the system depends on past states of the system; neutral functional differential equations (NFDE) in which the rate of change of the system depends on its own past values and advanced functional differential equations (AFDE) in which the rate of change depends on higher order derivatives of past values. In this study we study the effect of delay introduced by finite speed of propagation in a reaction-diffusion FHN model of advanced type.

The generic form of a system of delayed coupled neurons take the form

$$\dot{X}_i = F(X_i) + \sum_{j=1}^{N} g_{i,j} f(X_i, X_j(t-\tau_{i,j})), \tag{1.20}$$

where X_i (X_j) represents the state of the i^{th} (j^{th})-neuron, $g_{i,j}$ is a coupling function and $N \in \mathbb{Z}^+$ is the number of neurons in the network. $\tau_{i,j} = \frac{\chi_i - \chi_j}{v}$ is the delay introduced by a propagation traveling at finite speed v between neuron i located at χ_i and neuron j, located at χ_j. We shall assume that all neurons are equidistant from one another so that we may consider $\tau_{i,j} = \tau$.
For N-coupled FHN neurons with delay, Eq.(1.20) has the following representation:

$$\dot{u}_i = u_i - \frac{u_i^3}{3} - v_i + I + D \sum_{j=1}^{N} g_{i,j} \left[u_j(t-\tau) - u_i(t) \right], \tag{1.21}$$

$$\dot{v}_i = \varepsilon(u_i + a - b v_i), \tag{1.22}$$

assuming local coupling of the membrane potentials via gap junctions.
Unlike differential equations without delay, there is a possibility that systems with delay may experience oscillating solutions, induced by the delay. This phenomenon is widely known and has been observed in many dynamical systems with delay [65, 66]. Detail analysis and a survey of delay differential equations are covered in Refs.[64, 12]. In Ref.[18] delay in Hopfield coupled neurons was shown to induce a supercritical Hopf bifurcation. Furthermore, the occurrence of such oscillations was characterized in terms of the network topology. Ref.[57] studied the onset of delay-induced instability in an integro-differential model of intracortical neurons as well as the impact of delay on the pattern formation of the system. In Ref.[17], the authors studied the effect of delay on the linear stability of system of coupled FHN neurons of the kind shown in Eq.(1.22). Likewise it was shown that when the time delay exceeds a certain threshold, a Hopf bifurcation occurs. The direction of the Hopf bifurcation was computed using normal form and center manifold techniques. This thesis addresses a problem similar to the aforementioned references but considers a semi-infinite-dimensional system in contrast to the classical infinite dimensional delay systems. The main model we use throughout this thesis is a hyperbolic delayed differential equation of advanced-type. The latter also has the advantage of being tractable and computationally efficient to simulate.

1.3.4 Hyperbolic diffusion and finite propagation speed effect

The previous subsection highlighted some of the traditional ways in which delays are incorporated into models of spatially extended neurons. In this section, we explore delays due to finite speed of propagation first proposed by Cattaneo. This effect is based on the fact that the classical law of diffusion:

$$\mathbf{J}(x,t) = -D\nabla u, \tag{1.23}$$

known as Fick' law, where $\mathbf{J}(x,t)$ represents the flux, u the diffusing species, and D a diffusion matrix can be modified by considering that a finite time τ, known as the relaxation time, is required for propagation to move from one spatial location to the nearest neighbor. If $\mathbf{J}(x,t+\tau)$ represents the actual flux of the diffusing quantity—in this case the membrane potential, then it can be expanded in a Taylor series:

$$\mathbf{J}(x,t+\tau) = \mathbf{J}(x,t) + \tau\frac{\partial \mathbf{J}}{\partial t} + \mathscr{O}(\tau^2), \tag{1.24}$$

assuming a small $\tau \geq 0$. This modification, when combined with Fick's law and the continuity equation:

$$\frac{\partial u}{\partial t} = f - \nabla.\mathbf{J}, \tag{1.25}$$

where f represents the location production of the field u, gives the hyperbolic reaction diffusion equation

$$\tau\frac{\partial^2 u}{\partial t^2} + \frac{\partial u}{\partial t} = D\nabla^2 u. \tag{1.26}$$

Note that this equation resembles Maxwell's equation of propagating waves in space where the square of the speed of the waves is inversely proportional to the relation time. For this reason, the hyperbolic formulation of diffusion is called the Maxwell-cattaneo equation, in some academic spheres.

1.3.5 Significance of the relaxation time

Equation (1.26) is a second order wave equation with nonlinear forcing and damping. As such this system supports damped waves propagating at speeds $v \propto \frac{1}{\sqrt{\tau}}$. As $\tau \to 0$, the wave speed approaches infinity while for a finite $\tau > 0$, the wave speed is finite. Furthermore, let's consider an electrical analogy— the telegrapher's equations [67]:

$$\frac{\partial^2 V(x,t)}{\partial x^2} - LC\frac{\partial^2 V(x,t)}{\partial t^2} = (RC+GL)\frac{\partial V(x,t)}{\partial t} + GRV(x,t), \tag{1.27}$$

which represents the propagation of the potential V along a unit length of a cable of resistance R, self capacitance C, self inductance L and leakage conductance G. We see that τ in Eq.(1.26) plays the same role as inductance (inertia) and capacitance in Eq.(1.27). As such an increase in τ corresponds to an increase in voltage inertia or an increase in the self capacitance of the neuron. In each case, the net effect is a voltage which rises (falls) at a slower speed—the wave propagates at a finite speed. When the inductance of the cable is neglected, we recover the classical parabolic propagation. The time τ can also be shown to be related to the relaxation time or time constant of fading memory [68]. That is, propagation media with very small τ have extremely short memory — the flux at any moment t depends less on flux from a previous time. Examples of such materials are pure metals or materials with a homogeneous inner structure. On the other hand, media with long memory such as materials with inhomogeneous inner structures, will have a very large τ. Most biological tissue fall into the latter category. A full discussion on the scale of the relaxation time τ for various materials and media can be found in Ref.[68].

1.4 Local bifurcations of vector fields

We begin our discussion of nonlinear oscillations and waves by reviewing some of the bifurcation mechanisms that give rise to these states as well as their theoretical underpinnings. We focus on bifurcations of a time-continuous vector field in the vicinity of some critical parameter. A neuron can be regarded as a dynamical system with some initial and or boundary constraints. In this setting, the membrane potential and other phenomenological variables can be represented by a state space variable, whose evolution in space and time is dictated by some differential equation of the form:

$$\frac{du}{dt} = f(u,\mu), \tag{1.28}$$

where the unknown u is the time-dependent state variable, $f(u,\mu)$ the vector field, and μ is some time-independent vector of system parameters of interest.

The stationary states or equilibria of Eq.(1.28) are given by the equilibrium manifold $f(u_0,\mu) = 0$. The stability of an equilibrium is determined by the eigenvalues of the Jacobian maxtrix $A = \frac{df}{du}(u_0,\mu)$, for an ordinary differential equation and by the eigenvalues of a linear operator $\mathscr{L}$, in some function space, if Eq.(1.28) is a partial differential equation. Let n_-, n_+ and n_0 be the eigenvalues of the linearized operator with negative, positive and zero real parts respectively.

Definition 1. *An equilibrium is said to be hyperbolic if $n_0 = 0$. A hyperbolic saddle equilibrium is that for which $n_+ n_- \neq 0$.*

Near a hyperbolic equilibrium, a system is topological equivalent to its linearization (Hartman-Grobman Theorem). However by varying the parameter set μ, it is possible for an equilibrium to become nonhyperbolic and lose its stability as μ crosses some critical value with $n_0 \neq \emptyset$. It follows that other attracting states may then emerge with qualitatively different dynamics than former state.

Definition 2. *The appearance of a topologically nonequivalent phase portrait under variation of parameters is called a bifurcation.*

Examples of attracting states that might be observed beyond criticality are: stationary, periodic, quasi periodic and chaotic states. Near criticality, Eq.(1.28) may be reduced to a simplified equation for critical amplitudes known as the normal form.

1.4.1 Codimension-one bifurcations

In what follows we will assume that μ is one-dimensional such that the stability properties of u change only under the influence of one parameter. The bifurcations induced in this case are known as codimension-one bifurcations. We shall also assume that u_0 is the origin and μ_c the corresponding critical parameter. When u_0 is nontrivial, we may translate it to the origin with the help of the transformation: $u \to u - u*$. Furthermore let $\alpha = \mu - \mu_c$, be the distance to the bifurcation point.

Saddle-node and Pitchfork bifurcation

Assume the vector field in the neighborhood of $(u, \alpha) = (0,0)$ is of class C^k, $k \geq 2$ with the following properties:

$$f(0,0) = 0, \quad \frac{\partial f}{\partial u}(0,0) = 0. \tag{1.29}$$

The first condition of Eq.(1.29) implies that the origin is an equilibrium at $\alpha = 0$ while the second signals a nonhyperbolic equilibrium with a zero eigenvalue. According to the implicit function theorem [69], the equilibrium $u_0(\alpha)$ is discontinuous in the neighborhood $(0,0)$ —that is a bifurcation takes place.

We now consider the first and simplest mode through which an equilibrium might lose its hyperbolicity:

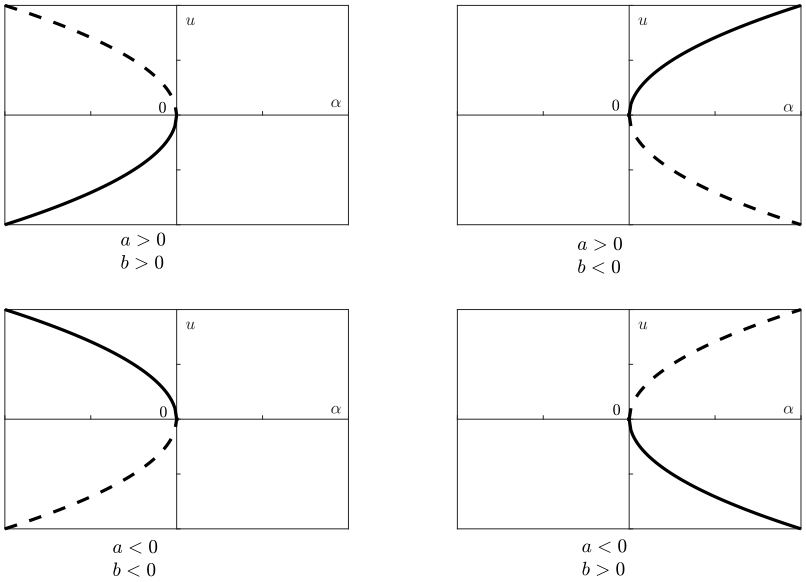

Figure 1.6 Saddle node bifurcation diagram as a function of normal form parameters. Solid curves indicate stable equilibria while dashed curves denote unstable equilibria.

Definition 3. *The appearance of a simple zero eigenvalue of the vector field upon variation of a parameter is known as a fold or saddle-node bifurcation.*

Close this this point, Eq.(1.28) has the normal form:

$$\frac{du}{dt} = a\alpha + bu^2, \tag{1.30}$$

where a and b are real constants. The equilibrium manifold of Eq.(1.30) are given by the parabola $\alpha = -\frac{b}{a}u^2$ and have the following properties depending on the values of a and b:

— If $ab\alpha > 0$, there are no equilibria.

— If $\alpha = 0$, there exist one equilibrium

— If $ab\alpha < 0$ there exist two equilibria $u = \pm\sqrt{\frac{-a\alpha}{b}}$.

The stability properties of the pair of equilibria which emerge beyond threshold are summarized in Fig.(1.6). The fold bifurcation is popularly known as the “ blue sky bifurcation" because it leads to the creation of a stable and unstable attractors out of no existing attractor.

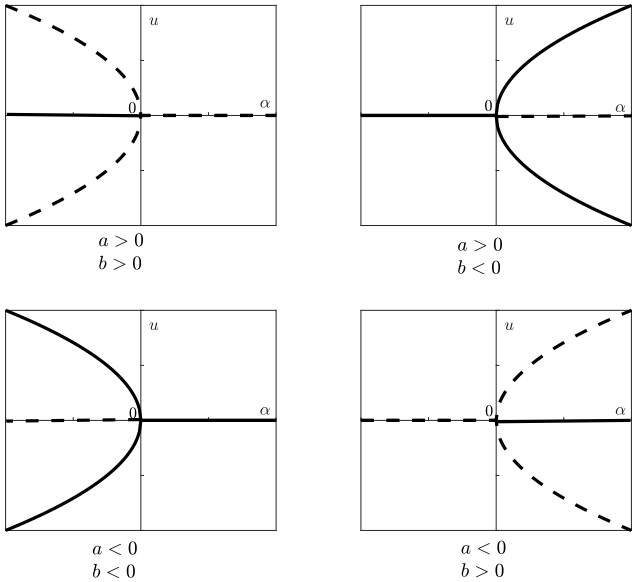

Figure 1.7 Pitchfork bifurcation diagram as a function of normal form parameters. Solid curves indicate stable equilibria while dashed curves denote unstable equilibria.

Now suppose that in addition to the conditions in Eq.(1.29), the vetor field further satisfies:

$$f(u,\alpha) = -f(-u,\alpha), \tag{1.31}$$

$$\frac{\partial^2 f}{\partial \alpha \partial u}(0,0) \neq 0 \qquad \frac{\partial f}{\partial u^3}(0,0) \neq 0. \tag{1.32}$$

It follows that Eq.(1.28) in the neighborhood of $(0,0)$ has the normal form:

$$\frac{du}{dt} = a\alpha u + bu^3. \tag{1.33}$$

The dynamics of the normal form as a function of its parameters is as follows:

— If $ab\alpha \geq 0$, there is always one equilibrium point $u_0 = 0$.

— If $ab\alpha < 0$ there exist two additional equilibria $u = \pm\sqrt{\frac{-a\alpha}{b}}$ with opposite stability to u_0.

These conditions indicate the presence of a Pitchfork bifurcation. When the emerging equilibria are stable we refer to the bifurcation as supercritical Pitchfork and subcritical Pitchfork, when the emerging equilibria are unstable. Refer to Fig.(1.7) for the full bifurcation diagram of the Pitchfork bifurcation. The pitchfork bifurcation is commonly encountered in

spatially extended systems with reflexive symmetry ($u \mapsto -u$). Like the fold bifurcation, it is associated with a simple zero eigenvalue of the vector field but unlike the fold bifurcation, there exist an equilibrium $u_0 = 0$ for all α so that the additional pair of equilibria is not created out of thin air.

Hopf bifurcation

Definition 4. *A Hopf bifurcation occurs when the linear operator of the vector field about an equilibrium has a pair of purely imaginary eigenvalues as a parameter is varied.*

The Hopf bifurcation generically occurs in systems in two dimensions [70] but can also occur in dimensions greater than two [71]. Suppose the vector field of Eq.(1.28) is of class C^k, $k \geq 5$ and satisfies:

$$f(0,0) = 0, \quad \frac{\partial f}{\partial u}(0,0) \neq 0, \tag{1.34}$$

such that the linear operator has eigenvalues $\pm i\omega$, $\omega > 0$. In the neighborhood of $(u,\alpha) = (0,0)$, Eq.(1.28) is topologically equivalent to the dynamics with normal form:

$$\frac{dz}{dt} = i\omega z + a\alpha z + bz|z|^2, \tag{1.35}$$

along with its conjugate counterpart. Note that here , a and b are complex numbers. The real part of b(b_r) at $\alpha = 0$ is also referred to as the first Lyapunov coefficient ($l_1(0)$). The corresponding bifurcation diagram can be deduced from the following conditions:

— If $a_r b_r \alpha > 0$, Eq.(1.28) has precisely one equilibrium $u(\alpha)$ which is stable for for $b_r < 0$ and unstable for $b_r > 0$.

— If $a_r b_r \alpha < 0$, Eq.(1.28) has a unique periodic orbit which surrounds the unique equilibrium $u(\alpha)$. The periodic orbit is stable for $b_r < 0$ and unstable for $b_r > 0$ while the equilibrium has opposite stability.

— At $\alpha = 0$ the unique equilibrium is unstable if $b_r > 0$ and is a focus if $b_r < 0$. The former case is referred to as subcritical hopf bifurcation while the latter is termed supercritical.

The bifurcation diagram of the normal form of Eq.(1.35) is similar to that of the Pitchfork bifurcation shown in Fig.(1.7), if we replace a and b in Eq.(1.33) with a_r and b_r respectively. Equation.(1.35) is a canonical model for single and strongly coupled oscillators near a Hopf bifurcation. For strongly coupled oscillators, this normal form is usually referred to as the Stuart-Landau equation [72]. If the coupling between oscillators is weak, then diffusion

could play a significant role in which case the resulting normal form would be of the form

$$\frac{dz}{dt} = i\omega z + a\alpha z + bz|z|^2 + \frac{\partial^2 z}{\partial \xi^2}, \tag{1.36}$$

known as the complex Ginzburg-Landau (CGL) equation [72]. In this thesis, we derive this equation from normal form arguments using the center manifold theory (see section2.3.1) due to Iooss [73]. Note that the CGL may also be derived by realizing that the dynamics on the center manifold is slower than on the remaining manifolds. This difference in time scales may be exploited to derive reduced order models of a system near a bifurcation point. This approach, known as the multiple scales perturbation method, is applied in section 3.5.

Local bifurcation of maps and cycles

Suppose Eq.(1.28) has some periodic solution corresponding to a limit cycle. It is possible to study the stability of this cycle under parameter variations by considering the dynamics of a Poincaré map across this orbit. let this map be of the form:

$$u \mapsto f(u, \alpha). \tag{1.37}$$

A fixed point of such a map corresponds to a periodic orbit in Eq.(1.28) while its bifurcations corresponds to bifurcations of the cycle. If u_0 is a hyperbolic fixed point of Eq.(1.37) at some α then the stability of u_0 is determined by the Floquet multiplier $\mu_1 = f_x(u_0, \alpha)$.

Definition 5. *The bifurcation associated with $\mu_1 = 1$ is called the saddle node of fixed points.*

Remark 1. *When the fixed point is a cycle, this bifurcation is referred to as limit point of cycles (LPC). A Limit point of cycles implies the birth (destruction) of a stable and an unstable limit cycle as a parameter is varied. The normal form of the fold of maps has the same structure as Eq.(1.30):*

$$u \mapsto u + a\alpha + bu^2. \tag{1.38}$$

Definition 6. *The bifurcation associated with $\mu_1 = -1$ is called the flip or period-doubling (PD) bifurcation of fixed points.*

Remark 2. *At the flip bifurcation of a cycle, a period-n cycle, $n \in \mathbb{N}^*$, switches to a period-2n cycle. The flip bifurcation has normal form*

$$u \mapsto -(1 + a\alpha)u + bu^3. \tag{1.39}$$

Definition 7. *The bifurcation associated with $\mu_{1,2} = e^{\pm\theta_0}$, $0 < \theta_0 < \pi$, and no other eigenvalues on the unit circle is called the Neimark–Sacker bifurcation.*

Remark 3. *A Neimark–Sacker (NS) bifurcation corresponds to the birth (destruction) of an invariant circle or torus if the bifurcating fixed point is a cycle. The NS bifurcation has normal form*

$$z \mapsto (1+\alpha)e^{i\theta_0}z + c_1^0 z|z|^2 + \mathscr{O}(|z|^4), \tag{1.40}$$

where $z \in \mathbb{C}$. Like Hopf bifurcations, NS bifurcations can be super- or subcritical depending on the sign of c_1^0.

1.4.2 Codimension-two bifurcations

If one relaxes the one-dimensional constraint imposed on the parameter vector α and considers it to be two dimensional (α_1, α_2), then a host of new bifurcation phenomena could be exhibited by Eq.(1.28) as the two parameters are varied simultaneously across the (α_1, α_2)-plane. Detection and continuation of codimension-two (codim-2) bifurcations are usually performed starting from a saddle node point or a Hopf point. Suppose at $\alpha = 0$, Eq.(1.28) has a eigenvalue $\lambda_1 = 0$. Continuation of the saddle node curve along the (α_1, α_2)-plane can yield the following bifurcations: Bogdanov-Takens bifurcation ($\lambda_1 = \lambda_2 = 0$), fold-Hopf bifurcation ($\lambda_1 = 0$ and $\lambda_{2,3} = \pm i\omega$) and cusp bifurcation ($b = 0$). Now suppose we begin the continuation from a Hopf bifurcation point instead ($\lambda_{1,2} = \pm i\omega$), then the following bifurcations may take place: Hopf-Hopf bifurcation ($\lambda_{1,2} = \pm i\omega_1$, $\lambda_{3,4} = \pm i\omega_2$), and Bautin or generalized Hopf bifurcation (GH) bifurcation ($b_r = 0$). Across the GH point, the Hopf bifuration switches from supercritcal to subcritical, along the Hopf curve. Due to its relevance to our research, we shall focus only on the Bautin bifurcation and discuss the phase portrait around this point. For a complete derivation and analysis of all the codimension-2 bifurcations listed above refer to Ref.[74]

Generalized Hopf (GH) bifurcation

Suppose system (1.28) has a pair of purely imaginary eigenvalues and a corresponding normal with $l_1(0) = 0$. Furthermore assume the second Lyapunov coefficient $l_2(0) \neq 0$ (See Ref.[43]), then the system has normal form:

$$\dot{z} = (\beta_1 + i)z + \beta_2 z|z|^2 + \beta_3 z|z|^4, \tag{1.41}$$

where β_1, β_2, and β_3 are real coefficients. We shall focus on the case with $\beta_3 = -1$, corresponding to the case with a negative second Lyapunov coefficient. The phase portrait

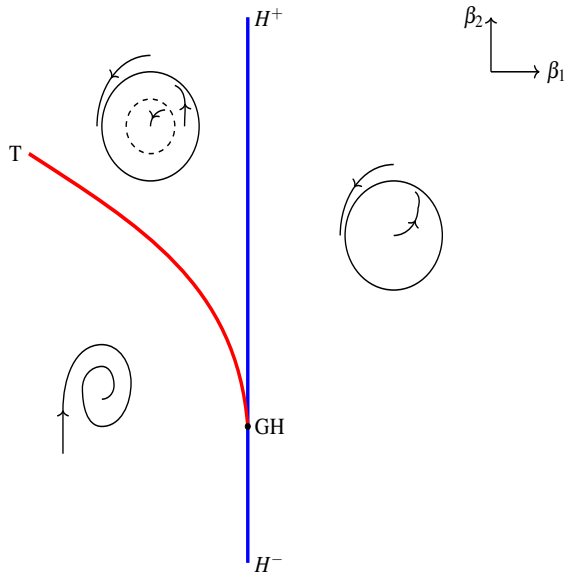

Figure 1.8 Bifurcation diagram of Bautin bifurcation. Blue curve represents the Hopf bifurcation curve along which the equilibrium has eigenvalues $\lambda_{1,2} = \pm i\omega$. H^+ and H^- represents the subcritical and supercritical branches of the Hopf curve while GH represents the Bautin bifurcation. The red curve represents the LPC curve along which a stable and unstable cycles collide.

around the GH point can be traced by transforming Eq.(1.41) to polar coordinates $z = \rho e^{i\phi}$:

$$\dot{\rho} = \rho(\beta_1 + \beta_2\rho^2 - \rho^4), \tag{1.42}$$

$$\dot{\phi} = 1. \tag{1.43}$$

Eq.(1.43) has a trivial equilibrium and a maximum of two equilibria corresponding to cycles ($\rho = constant$). These cycles branch from the trivial solution along the curves:

— $H^+ = \{(\beta_1, \beta_2) : \beta_1 = 0, \beta_2 > 0\}$, corresponding to an unstable limit cycle and

— $H^- = \{(\beta_1, \beta_2) : \beta_1 = 0, \beta_2 < 0\}$, corresponding to a stable limit cycle.

They collide and disappear in a saddle node bifurcation of cycles (LPC) along the curve:

$$T = \{(\beta_1, \beta_2) : \beta_2^2 + 4\beta_1 = 0, \beta_2 > 0\}.$$

The GH point partitions the (β_1, β_2)-plane into three distinct regions depicted in Figure.(1.8). The dynamics around the GH point is as follows:

— Crossing the curve H^- from left to right, generates a unique stable limit cycle around the trivial equilibrium.

— Crossing the curve H^+ from left to right leads to the collision of an unstable cycle and the trivial equilibrium, leading to an instability of the latter.

— Crossing the curve T from left to right (resp. right to left), leads to the creation (resp. annihilation) of a stable and unstable limit cycles.

Designing a burster around a GH point

Note that the parameter β_1, in Eq.(1.41), controls the stability of the trivial equilibrium of Eq.(1.41). The latter is stable (resp. unstable) for $\beta_1 < 0$ (resp. $\beta > 0$). As such it is possible to construct bursting dynamics around the GH point by having β_1, or more variables of the pair (β_1, β_2), periodically oscillate in time [75]. Up to four types of bursting[29] may be constructed in this case:

— Hopf-Hopf bursting, in which variable oscillates along path 1 in Fig.1.9 while the other is held fixed.

— SubHopf-fold bursting, in which one variable oscillates along path 2 while the other constant.

— SubHopf-Hopf corresponding to the pair (β_1, β_2) oscillating along path 3.

— Hopf-fold corresponding to the pair (β_1, β_2) oscillating along path 4.

Of all possible bursting mechanisms, the SubHopf-Fold bursting also known as elliptic bursting, is the most studied in relevant literature. This is because its dynamics is easily amenable to analytical studies. The canonical form for such an elliptic burster is given by

$$\begin{aligned} \dot{z} &= (u+i)z + \beta_2|z|^2 z + \beta_3|z|^4 z \\ \dot{u} &= \eta(s - |z|^2), \end{aligned} \tag{1.44}$$

where z contains information about the fast variable and fast current, u is analogous to the slow adaptation current and η controls the ratio of the fast and slow times scales of bursting with $0 < s < 1$. Detail analysis and synchronization of elliptic bursters of this type have been examined by Izhikevich [76] and Azad et al.[77], under different coupling schemes.

Codimension-two bifurcation of maps and cycles

There are far more codimension-two bifurcations of maps than there are in continuous systems. This is true even for the simplest 1D maps. To name a few: the cusp (CP), generalized period doubling (GPD), resonances, and Chenciner bifurcations. As we did for the continuous case, we shall briefly discuss the bifurcations which are relevant to this thesis.

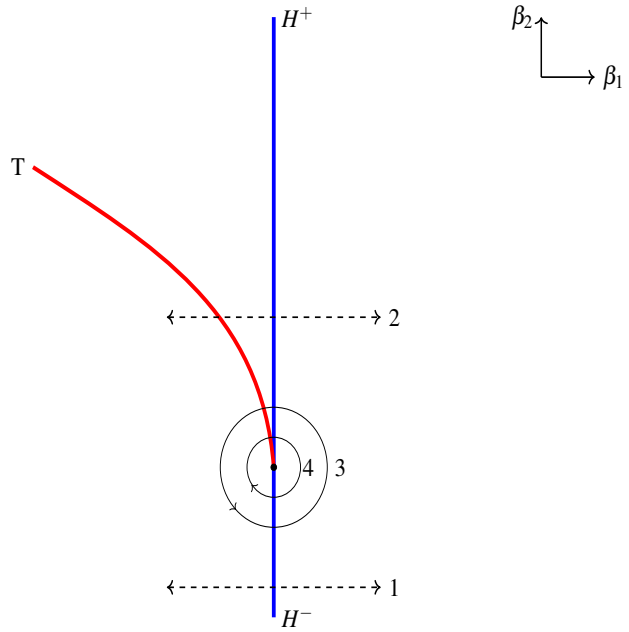

Figure 1.9 Illustration of different paths for bursting mechanisms in the neighborhood of a GH point.

A full classification of codimension-two bifurcations of maps as well as their reduced and full normal forms can be found in Ref.[78].

In discrete ODE's, the equivalent of the GH bifurcation is the Chenciner bifurcation (CH) or generalized Neimark-Sacker, with a similar bifurcation diagram. Surrounding this bifurcation are two principal curves, the Neimark-Sacker curve and Limit point curve. Details about the bifurcation diagram of this bifurcation can be found in Chapter 3 of Ref.[78]. The generalized period doubling bifurcation (GPD) is the period doubling equivalent of the GH and CH bifurcations. Table 1.1 summarizes the conditions on the multipliers and normal form coefficients, necessary to observe these bifurcations.

Label	**Name**	**Conditions**
CH	Chenciner	$\mu_{1,2} = e^{i\theta_0}$, $c_1^0 = 0$
GPD	Generalized period doubling	$\mu_1 = -1$, $b = 0$

Table 1.1 Some codimension-two bifurcations of maps relevant to this thesis. Here, b and c_1^0 are given by Eq.(1.39) and Eq.(1.40) respectively, and play the role of the first Lyapunov coefficient for maps.

1.5 Conclusion

In summary, we have reviewed the main features of the neuron, action potential generation and propagation as well as some mathematical models that form corner stones of mathematical neuroscience. Some elementary bifurcations that are common to most mathematical neuron models and relevant to this thesis have also been reviewed. By considering a neuron model as a vector field or a dynamical system, the mathematical theories of linear stability analysis, invariant manifolds, bifurcation theory and many more, may be appropriately applied to study the qualitative and quantitative features of a neuron model.

Chapter 2

Hyperbolic Fitzhugh-Nagumo models and methods

This chapter is a review of the various mathematical models and methods used throughout this thesis. A succinct description of the implementation of these methods is given, with examples of applications provided where necessary. These methods, including analytical and numerical methods, can be grouped into three main classes: analytical and numerical methods for equilibria location and stability analysis, methods for reduction to normal-form, and methods for building exact traveling wave solutions. This chapter is organized as follows: Section 2.1 provides a brief survey of the literature on the different models and methods used in this thesis. In section 2.2, we present the two main models used in this thesis notably the hyperbolic FHN model in section 2.2.1, and the hyperbolic photosensitive FHN model in section 2.2.2. In section 2.3, we review the main methods and their implementation. In this section, analytical methods are considered in section 2.3.1 while numerical methods are considered in section 2.3.2. In section 2.4 we give a summary of the chapter.

2.1 Introduction and background

The idea of a hyperbolic FHN model is not new and was initially derived decades ago using arguments of internal variables[21], wherein the construct of a hyperbolic model of nerve propagation is shown to be thermodynamically consistent. In that same study, the authors demonstrated that such an equation still possesses solitonic and dissipative structures. In recent times, the hyperbolic FHN model was studied in multiple studies [22–24] in the context of existence and stability of traveling wave solutions. These studies demonstrated

the existence of various stable solitonic structures admitting a maximum speed for nontrivial values of the relaxation time.

External currents having the appropriate characteristics can stimulate a variety of dynamical behaviors in neurons, sometimes in combination with other parameters. For example, photosensitive neurons convert light signals into electrical pulses that fine-tune the spiking activity of these neurons [79, 80]. While most experiments involving the effect of light on neural spiking have been based on biological photosensitive neurons, recent attempts have been made to this effect using models amenable to mathematical analysis and capable of being implemented electronically. Using the celebrated Fitzhugh-Nagumo neuron[48] as a basis, Liu et al. [81] proposed a novel photosensitive Fitzhugh-Nagumo neuron using a phototube as a transducer. The photocurrent which drives the circuit or the model is produced by the photoelectric effect [82, 83] taking place inside the phototube or a similar photosensitive device. The idea of a photosensitive FHN model is quite new and could prove relevant in future research. For this reason, we included this model in this thesis, modified accordingly, to include the effects of hyperbolic diffusion.

Although most of the bifurcations covered in the Chapter 1 occur in generic systems of finite dimension, equal to the dimension of the normal form equations, these bifurcations can be shown to occur in systems with higher dimensions. In the case of the Hopf bifurcation, the dynamics and stability of the periodic orbit can be assessed on a two dimensional manifold known as the center or critical manifold. Formulas for orbital stability on such a manifold have been derived since decades and are easy to implement [84]. However, when dealing with systems of dimensions greater than two, a reduction of the asymptotic dynamics to that of the center manifold is indispensable if one wishes to obtain information about the stability of limit cycles. Such dimensional reduction at nonhyperbolic points can be achieved using techniques such as the Lyapunov-Schmidt method [85], Hopf's power series method, averaging theory, Lyapunov functions [86] and center manifold theory [87]. For systems in Jordan form, the application of the center manifold reduction is straightforward. Even without reduction to the Jordan form, the projection method [74] may be applied to achieve similar results. For a good introduction to the theory and proofs, refer to Refs.[88] and [89].

Solitary waves or solitons [90] are solutions of certain PDE's which are uniformly translating in space and maintain a fixed shape due to balances between dispersion and nonlinearity for Hamiltonian systems or gain and loss for dissipative systems. In biological neurons, solitons are traveling fronts and pulses (action potentials). Exact solitary solutions, may be constructed directly from a PDE via analytical techniques such as the G'/G-method [91, 92], Tanh-method [93], Hirota bilinear method [94] , direct integration method [95] and many more. Exact solutions to solitary waves may also be obtained from canonical

models such as the complex Ginzburg-Landau [36] of dissipative systems or the non-linear Shrödinger equation (NLS) [96] of Hamiltonian systems. A popular method of deriving these models is by reductive perturbation [97]. This consists of approximating the behavior of the system, very close to a bifurcation point with a power series expansion in a perturbation parameter, and studying different behaviors at different orders of this parameter. This technique has been used extensively to construct solitary solutions in models of single neurons [98–100].

Although nerve pulse propagation is traditionally modeled by continuous differential equations, in some cases, it may be more appropriate to use a system of discrete equations. For example, in myelinated axons, propagation occurs in a saltatory manner, from one node of Ranvier to the next [101]. In this case, it makes sense to view the diffusion as discrete in space. Such models, like continuous models, have been shown [102, 103] to bear traveling wave solutions of the same quality as the continuous model. Another instance in which it makes sense to use a discrete model is during modeling processes that change only after discrete time intervals. For example, we may be interested in tracking the membrane potential only after discrete time intervals. For instance, when performing parameter estimation from experimental data [104]. An easy wave to implement discretizations in space and in time is via finite difference approximations which are relatively easy to implement and provide rapid convergence to the desired solutions (if implemented correctly).

Bifurcation analyses via analytical methods is quite an involved process for most differential equations. This complex analysis if further compounded by the nonlinearity present in PDE's describing real systems or practical scenarios. As a result, numerical bifurcation analyses is often the preferred method for bifurcation analyses. Many software tools have been developed to detect and continue various bifurcations of differential equations. These software have mostly been developed for ordinary differential equations. Examples of such software include: AUTO [105], MATCONT [106], XPPAUT, COCO and many others. Recent software such as pde2path [107], based on MATLAB, have been developed to address bifurcation analyses of PDE's.

2.2 Modified Fitzhugh-Nagumo models

2.2.1 The hyperbolic FHN Model

The hyperbolic diffusion formulation described in Chapter 1 forms the basis for all models used throughout this thesis. When applied to the classical FHN model (1.19), the

result is the system of equations:

$$\begin{aligned} \tau u_{tt} + u_t &= d u_{xx} + u - \frac{u^3}{3} - v + I \qquad in\ \ \Omega = [0,\ell], \\ v_t &= \varepsilon(u + a - bv), \\ u_x(0) = u_x(\ell) &= v_x(0) = v_x(\ell) = 0, \end{aligned} \tag{2.1}$$

defined on a one-dimensional bounded domain $\Omega = [0,\ell]$, representing a neuron of length ℓ. u_t and u_{tt} represent respectively first and second order partial time derivatives of u. We impose suitable boundary conditions on the system, of Neumann-type. Here, d is the diffusion coefficient. For analytical stability analysis, we neglect the term I.

We may further recast the system (2.1) as a system of autonomous differential equations having the structure of Eq.(1.28), as follows:

$$\begin{aligned} u_t &= w, \\ w_t &= \frac{1}{\tau}(d u_{xx} + u - \frac{u^3}{3} - v - w + I) \qquad in\ \ \Omega = [0,\ell], \\ v_t &= \varepsilon(u + a - bv), \\ u_x(0) = u_x(\ell) &= v_x(0) = v_x(\ell) = 0, \end{aligned} \tag{2.2}$$

where the new variable $w = u_t$ has been introduced to bring the equations to a parabolic form.

To use the center manifold reduction (detailed subsequently) on Eq.(2.2), we need the equilibrium to be located at the origin (0,0,0). If the system is already at the origin, the reduction is easier otherwise the nonhyperbolic equilibrium needs to be translated to the origin. If the steady state of the system is independent of the bifurcation parameter, the nontrivial equilibrium may be translated to the origin before bringing the system to a nonhyperbolic equilibrium. Let $U^* = (u^*, w^*, w^*)$ denote a nontrivial steady state of Eq.(2.2). We may translate the latter to the origin as : $X = u - u^*$, $Z = v - v^*$, $Y = w - w^*$. Secondly, we may re-scale the length of the neuron by transforming the space variable $x \to \frac{\pi}{\ell}x$, to obtain the matrix equation:

$$\begin{aligned} U_t &= \mathscr{L}U + F(U,\delta) \qquad \hat{\Omega} = [0,\pi], \\ U_x\big|_{x=0} &= U_x\big|_{x=\pi} = 0, \end{aligned} \tag{2.3}$$

where

$$U = \begin{pmatrix} X \\ Y \\ Z \end{pmatrix}, \quad F(U,\delta) = \begin{pmatrix} 0 \\ -\delta u^* U_1^2 - \frac{\delta}{3} U_1^3 \\ 0 \end{pmatrix},$$

and $\mathscr{L} = D\Delta + A$, is a formal linear operator (Δ being the laplacian operator). The terms D and A are matrices defined as

$$D = \begin{pmatrix} 0 & 0 & 0 \\ \frac{d\delta\pi^2}{\ell^2} & 0 & 0 \\ 0 & 0 & 0 \end{pmatrix}, \text{and} \quad A = \begin{pmatrix} 0 & 1 & 0 \\ \delta(1-u^{*2}) & -\delta & -\delta \\ \varepsilon & 0 & -\varepsilon b \end{pmatrix},$$

where $\delta = \frac{1}{\tau}$.

The linear operator is defined such that

$$\mathscr{L} : \mathscr{Y} \to \mathscr{X}, \tag{2.4}$$

with domain

$$\mathfrak{D}(\mathscr{L}) = \{U \in \mathscr{Y},\ U'(0) = U'(\pi) = 0\}, \tag{2.5}$$

where

$$\mathscr{Y} = (H^2(\Omega) \cap H^1(\Omega)) \times \mathbb{R}^2, \tag{2.6}$$

$$\mathscr{X} = L^2(\Omega) \times \mathbb{R}^2. \tag{2.7}$$

The operator $\mathscr{L}$ defines a closed compact linear operator in the Hilbert space $\mathscr{X}$. $H^2(\Omega)$ and $H^1(\Omega)$ are respectively second and first order Sobolev spaces. $L^2(\Omega)$ is the Hilbert space of square integrable functions while $\mathbb{R}$ is the space of real numbers. The operator $\times$ defines the direct product of two vector spaces.Precise definitions for these function spaces are found in Appendix B.

Notice that D is an asymmetric diffusion matrix, A, the Jacobian of the system (2.3) around the uniform steady state, and $F(U,\delta)$ is assumed to be a smooth function with $D^j F(U,\delta) = 0$, $|j| \leq 1$. Furthermore, D is inversely proportional to the relaxation time and length. As such, larger values of τ or large ℓ, will induce slow spatial variations and vice-versa. If the diffusion is to be interpreted as local coupling between different interacting oscillators then a large τ would mean the system approaches the limit of weakly coupled oscillators. In this setting, the synchronous state can be lost to long wave perturbations.

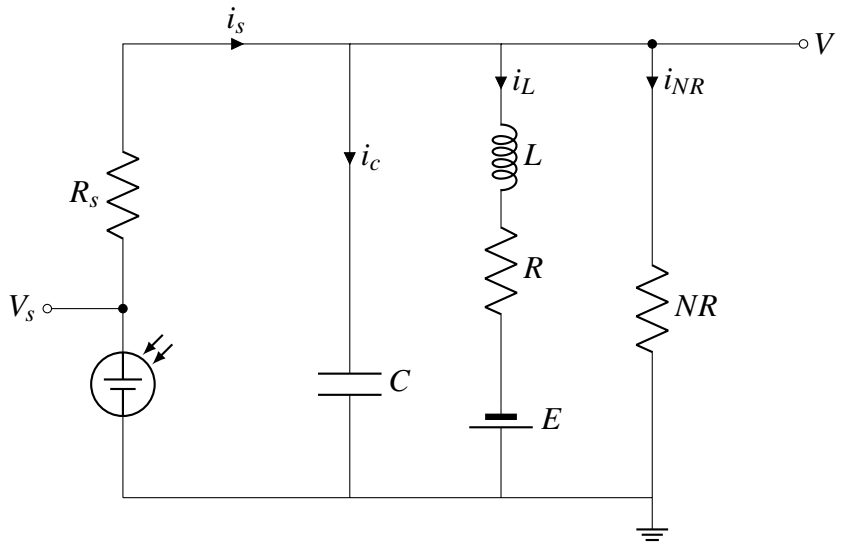

Figure 2.1 Schematic of photoelectric cell connected to the Fitzhugh-Nagumo setup showing various relevant voltages, and components: V_s is the output of the photoelectric cell, V the membrane potential across the neuron, C the membrane capacitance, and NR a nonlinear resistance.

In the absence of diffusion ($D = 0$), Eq.(2.3) defines in a natural way, a dynamical system in $\mathbb{R}^3$. In the presence of D, it has been shown that such a system defines an infinite dimensional time-continuous dynamical system in $\mathscr{X}$, a function space, see Ref.[74, 15].

2.2.2 A hyperbolic photosensitive neuron

The entire schematic for the classical FHN model coupled with a photosensitive device and input resistance is displayed in Fig.2.1. According to kirchhoff's law, the voltages and currents in Fig.2.1 are related as follows:

$$\begin{aligned} C\frac{dV}{dt} &= i_s - i_L - i_{NR}, \\ L\frac{di_L}{dt} &= V + E - Ri_L, \end{aligned} \tag{2.8}$$

where V_s represents the voltage across the photoelectric cell, and $i_s = \frac{V_s - V}{R_s}$, represents the induced photocurrent. The latter is related to the intrinsic properties of the photoelectric cell as

$$i_s = \frac{2I_H}{\pi}\arctan(V_s - V_a),$$

where I_H and V_a are the saturation current and normalized parameter associated with the photoelectric cell. The current i_{NR}, through the nonlinear resistor is related to the voltage

across it as follows [46]:

$$i_{NR} = -\frac{1}{\rho}\left(V - \frac{V^3}{3V_0^2}\right), \tag{2.9}$$

where ρ and V_0 are normalization parameters of the nonlinear resistor.

From Eq.(2.8) the following nondimensionalized system is obtained

$$\begin{aligned} \dot{u} &= f(u,v), \\ \dot{v} &= g(u,v), \end{aligned} \tag{2.10}$$

where $\dot{u}$ and $\dot{v}$ represent the time derivatives of the respective functions with

$$\begin{aligned} f(u,v) &= u(1-\xi) - \frac{u^3}{3} - v + u_s, \\ g(u,v) &= \varepsilon(u + a - bv), \end{aligned} \tag{2.11}$$

where the following transformations have been employed:

$$\begin{gathered} u \to \frac{V}{V_0},\ v \to \frac{\rho i_L}{V_0},\ t \to \frac{t}{\rho C},\ a \to \frac{E}{V_0}, \\ b \to \frac{R}{\rho},\ \varepsilon \to \frac{\rho^2 C}{L},\ \xi \to \frac{\rho}{R_s},\ u_s \to \frac{\rho V_s}{R_s V_0}. \end{gathered}$$

If one considers an ensemble of photosensitive neurons coupled by diffusion, then the local dynamics of each neuron may be described by a hyperbolic system of ODE's, assuming non-negligible relaxation time. It follows that Eq.(2.10) can be recast as

$$\begin{aligned} \dot{u} &= h(u,w,v), \\ \dot{w} &= \frac{1}{\tau}(f(u,w,v) - w), \\ \dot{y} &= g(u,w,v), \end{aligned} \tag{2.12}$$

where $h(u,w,v) = w = \dot{u}$.

2.3 Methods and applications

2.3.1 Analytical methods

Equilibria and invariant sets

Quantitative and qualitative information about the equilibria of Eq.(2.2) can be obtained from the equations

$$\mathscr{L}U + F(U,\delta) = 0, \tag{2.13}$$

$$U_x(0) = U_x(\pi) = 0. \tag{2.14}$$

these equilibria can be spatially uniform or inhomogeneous. For example, the spatially homogeneous equilibria, U_0 are obtained by solving the system of equations:

$$\begin{aligned} w &= 0, \\ u - \frac{u^3}{3} - v - w &= 0, \\ u - bv &= -a, \end{aligned} \tag{2.15}$$

which leads to the polynomial equation

$$u^3 + \frac{3(1-b)}{b}u + \frac{3a}{b} = 0. \tag{2.16}$$

This equation has up to three equilibria [47]. We used the following lemma, based on Vieta's formulas to obtain information about the quantitative nature of the different equilibria:

Lemma 1 ([108]). *A cubic polynomial of the form: $x^3 + a_2x^2 + a_1x + a_0 = 0$, $x \in \mathbb{C}^1$, has discriminant*

$$D = a_2^2a_1^2 - 4a_1^3 - 4a_2^3a_0 - 27a_0^2 + 18a_2a_1a_0. \tag{2.17}$$

Furthermore,
if $D > 0$, then the polynomial has three distinct real roots corresponding to three fixed points.
if $D = 0$, the polynomial has multiple roots.
if $D < 0$, the polynomial has a unique real root and two complex conjugate roots.

Linear stability analysis

In this thesis we were interested in the local stability of the system around a trivial equilibrium. Linear stability analysis is ubiquitous in the study of dynamical systems and is

a very powerful tool used to obtain information about the stability of dynamical states (fixed point, limit cycle, solitary wave etc), in their neighborhood. In fact, the Hartman–Grobman theorem [84] asserts that linearization about a hyperbolic equilibrium is sufficient to infer its global stability. For nonhyperbolic equilibria, linearization may not provide useful information about the local stability since nonlinear terms in Eq.(2.2) need to be taken into account. Linearization in this case, may be used to infer information about the dimension of the center manifold.

In the absence of diffusion the formal operator $\mathscr{L}$ is equivalent to the Jacobian around the origin. In this case the linear stability of the system can be obtained from the equation

$$U_t = AU. \tag{2.18}$$

Assuming eponentially growing or decaying solutions of the form $U = Ue^{\lambda t}$, and substituting this trial solution into Eq.(2.18) we obtain

$$det(A - \lambda I) = 0. \tag{2.19}$$

In the presence of diffusion $(D \neq 0)$, Eq.(2.18) is equivalent to

$$\mathscr{L}U = \lambda U, \tag{2.20}$$

where the solutions U are now of the form $U\phi_k e^{\lambda t}$, ϕ_k being a function which satisfies the boundary conditions, and k, the wavenumber. Eq.(2.20) is sometimes referred to as the Sturm-Liouville problem; with the corresponding boundary conditions.

Eqs.(2.19) and (2.20), upon simplification, yield a polynomial eigenvalue problem of the form

$$\chi(\lambda) = a_0\lambda^n + a_1\lambda^{n-1} + \cdots + a_n, \tag{2.21}$$

where $a_0 \ldots a_n$ are constants with $a_0 > 0$. Eq.(2.21) may be studied for sufficient and necessary conditions for the Hopf bifurcation with an attracting center manifold. In this thesis, we made use of the following useful theorem :

Theorem 1 ([109]). *$\chi(\lambda)$ has a pair of distinct roots, $i\omega$ and $-i\omega$ on the imaginary axis and all other roots in the left half plane if and only if $a_n > 0$, $\Delta_{n-1} = 0 \quad \Delta_{n-2} > 0, \ldots, \Delta_1 > 0$,*

where Δ_i represents the i^{th}-order principal minor or i^{th} Hurwitz determinant of H (χ) given by

$$H(\chi) = \begin{pmatrix} a_1 & a_3 & a_5 & \dots & \dots \\ a_0 & a_2 & a_4 & \dots & \dots \\ 0 & a_1 & a_3 & a_5 & \dots \\ 0 & a_0 & a_2 & a_4 & \dots \\ & & & & \ddots \end{pmatrix}. \tag{2.22}$$

Center manifold theory

In what follows, we briefly describe the center manifold theory and provide necessary conditions for the existence of a center manifold. Due to its ease of implementation and analytical tractability, we chose the center manifold reduction for the analysis of the stability of nonhyperbolic fixed points, throughout this thesis.

Let Eq.(1.28) at a nonhyperbolic equilibrium (u,α)=(0,0) be written as

$$\frac{du}{dt} = \mathscr{L}u + F(u,\alpha), \tag{2.23}$$

where $\mathscr{L}$ and $F(u,\alpha)$ are operators.

Hypothesis 1. *Assume $\mathscr{L}$ and $F(u,\alpha)$ satisfy the following:*

1. *$\mathscr{L}$ is a bounded linear operator in some Hilbert space $\mathscr{H}$ with domain $\mathfrak{D}$.*
2. *$F(u,\alpha)$ is a nonlinear function of class C^k, $k \geq 2$, satisfying:*

$$F(0,0) = 0 \quad DF(0,0) = 0. \tag{2.24}$$

Here, $DF(0,0)$ represents the Jacobian of the vector field of Eq.(2.23) at $(0,0)$.

Hypothesis 2. *Consider the spetrum of $\mathscr{L}$ at criticality: $\sigma = \sigma_+ \cup \sigma_0 \cup \sigma_-$,*
where σ_+, σ_0 and σ_- are respectively called unstable, center and stable spectrum such that $dim(\sigma_+) = n_+$, $dim(\sigma_0) = n_0$, and $dim(\sigma) = n_-$.

Remark 4. *It follows that at criticality, the space $\mathscr{H}$ may be decomposed as*

$$\mathscr{H} = E^c \oplus E^s \oplus E^u, \tag{2.25}$$

where E^c, E^s and E^u represents the vector spaces spanned by the eigenvectors of σ_0, σ_- and σ_+ respectively.

Theorem 2. *Assuming the above hypothesis hold, there exist a map $y = y(u_c, \alpha)$, $u_c \in E^c$ satisfying*

$$y(0,0) = 0, \;\; Dy(0,0) = 0, \tag{2.26}$$

and a neighborhood $\mathcal{N}_u \times \mathcal{N}_\alpha = (0,0)$ in $\mathfrak{D} \times \mathbb{R}^m$ such that for $\alpha \in \mathcal{N}_\alpha$, the n_0-dimensional local manifold:

$$W^c_{loc}(\alpha) = \{u_c, y(u_c, \alpha)\} \subset \mathfrak{D} \times \mathbb{R}^m, \tag{2.27}$$

has the following properties:

- *$W^c_{loc}(\alpha)$ is locally invariant. If $u(t)$ is a solution of Eq.(2.23) satisfying $u(0) \in \mathcal{N}_u \cap \mathcal{N}_\alpha$ and $u(t) \in \mathcal{N}_u$ for all $t \in [0,T]$ then $u(t) \in W^c_{loc}(\alpha)$ for all $t \in [0,T]$.*
- *$W^c_{loc}(\alpha)$ need not be unique.*
- *$W^c_{loc}(\alpha)$ is locally tangent to E_c.*
- *$W^c_{loc}(\alpha)$ contains the set of bounded solutions of Eq.(2.23) staying on $\mathcal{N}_u$ for all t.*
- *$W^c_{loc}(\alpha)$ has finite smoothness as the vector field of Eq.*(2.23) *in some neighborhood $\mathcal{N}_u \cap \mathcal{N}_\alpha$ of $(0,0)$.*

Remark 5. *The function $y(u_c, \alpha)$ is known as the reduction function. Its solutions are locally exponentially decaying (resp. growing) for $n_+ = 0$ (resp. $n_- = 0$). For the case $n_+ = 0$, the manifold is globally attracting and the evolution on the center manifold or restriction equation is given by*

$$\dot{z} = Az + f(u_c, y(u_c, \alpha)), \tag{2.28}$$

where A is a matrix whose eigenvectors span E^c. In this case, the stability of fixed points of Eq.(2.28) corresponds to the stability of the fixed point of Eq.(2.23) to the $\mathcal{O}(e^{-\gamma t})$, $\gamma > 0$:

$$u(t) = z(t) + \mathcal{O}(e^{-\gamma t}). \tag{2.29}$$

Normal form reduction without diffusion

Assume the diffusion $D = 0$ or that system (2.3) is made of identical, strongly coupled units. Further assume that the system is at a nonhyperbolic equilibrium (Hopf bifuration point) with the remaining eigenvalues in the left half of the complex plane. System Eq.(2.3) can be written in the form

$$\dot{U} = AU + F(U, \delta_c) + \mathcal{O}(|U|^4), \tag{2.30}$$

where δ_c represents the critical value of δ but could also represent any critical parameter value. To ease our notation, we represent δ_c at criticality simply as δ. For convenience, we

may sometimes represent $F(U,\delta)$ in the form:

$$F(U,\delta) = \frac{B(U,U)}{2} + \frac{C(U,U,U)}{6}, \tag{2.31}$$

where B and C are multi-linear functions of two (three) planar vectors on the critical eigenspace and defined by the following expressions:

$$\begin{aligned} B_i(x,y) &= \sum_{j,k=1}^{3} \left.\frac{\partial^2 F_i(\xi,\delta)}{\partial\xi_j\partial\xi_k}\right|_{\xi=0} x_j y_k, \\ C_i(x,y,v) &= \sum_{j,k,l=1}^{3} \left.\frac{\partial^3 F_i(\xi,\delta)}{\partial\xi_j\partial\xi_k\partial\xi_l}\right|_{\xi=0} x_j y_k v_l \quad i = 1\ldots 3. \end{aligned} \tag{2.32}$$

We now investigate the asymptotic dynamics on the center manifold of the system near a Hopf bifurcation. To this end, we project the system onto the center manifold using the generalized eigenvector, q and adjoint vector, p of A as outlined in the projection method [74]. The vectors p and q satisfy the equations

$$Aq = i\omega q, \tag{2.33}$$

$$A^T p = -i\omega p, \tag{2.34}$$

,and

$$\langle p,q\rangle = 1, \tag{2.35}$$

where ω is the frequency of the oscillations at the Hopf bifurcation. Note that the Jordan form of A at the Hopf bifurcation is

$$A = \begin{pmatrix} 0 & -\omega \\ \omega & 0 \end{pmatrix}. \tag{2.36}$$

Theorem 3 (Normal form theorem)**.** *By introducing a complex variable $U = zq + \bar{z}\bar{q} + y$, Eq.(2.30) can be written for sufficiently small $|\alpha|$ as a single equation*

$$\dot{z} = i\omega z + \frac{1}{2}g_{20}z^2 + g_{11}z\bar{z} + \frac{1}{2}g_{02}\bar{z}^2 + \frac{1}{2}g_{21}z^2\bar{z} + \ldots, \tag{2.37}$$

together with its conjugate counterpart. Here, $\alpha = \delta - \delta_c$, and $y = f(z,\bar{z})$ is a variable from the space complementary to the critical eigen space such that $\langle p,y\rangle = 0$. The coefficients

$g_{i,j}$ are given by:

$$g_{20} = \langle p, B(q,q)\rangle, \tag{2.38}$$

$$g_{11} = \langle p, B(q,\bar{q})\rangle, \tag{2.39}$$

$$g_{02} = \langle p, B(\bar{q},\bar{q})\rangle, \tag{2.40}$$

$$g_{21} = \langle p, C(q,q,\bar{q})\rangle - 2\langle p, B(q,s)\rangle + \langle p, B(\bar{q},r)\rangle + \frac{1}{i\omega}g_{20}g_{11} - \frac{2}{i\omega}|g_{11}|^2 - \frac{1}{3i\omega}|g_{02}|^2, \tag{2.41}$$

where r and s are generally complex matrices. Fulls details of the derivation of these formulas can be found in Ref.[74]. Eq.(2.37) is the restriction equation governing the dynamics on the center manifold. We may further reduce this equation to its pervasive form, the Poincaré form using the following lemma:

Lemma 2. *The equation*

$$\dot{z} = \lambda z + \sum_{2\le k+l\le 3} \frac{1}{k!l!} g_{kl} z^k \bar{z}^l + \mathscr{O}(|z|^4), \tag{2.42}$$

where $\lambda = \lambda(\alpha) = \mu(\alpha) + i\omega(\alpha)$, $\mu(0) = 0$, $\omega_0 > 0$ and $g_{ij} = g_{ij}(\alpha)$ can be transformed by an invertible parameter-dependent change of complex coordinate, smoothly depending on the parameter

$$z = w + \frac{h_{20}}{2}w^2 + h_{11}w\bar{w} + \frac{h_{02}}{2}\bar{w}^2 + \frac{h_{30}}{6}\bar{w}^3 + \frac{h_{12}}{2}w\bar{w}^2 + \frac{h_{03}}{6}\bar{w}^3, \tag{2.43}$$

for all sufficiently small α into the equation

$$\dot{w} = \lambda w + c_1|w|^2\bar{w}, \tag{2.44}$$

where

$$c_1 = \frac{i}{2\omega}\left(g_{20}g_{11} - 2|g_{11}|^2 - \frac{1}{3}|g_{02}|^2\right) + \frac{g_{21}}{2}. \tag{2.45}$$

Proof. :We attempt to eliminate the quadratic terms in Eq.(2.37) using the transformation

$$z = w + \frac{h_{20}}{2}w^2 + h_{11}w\bar{w} + \frac{h_{02}}{2}\bar{w}^2. \tag{2.46}$$

As suggested in Ref.[74], we consider the following inverse quadratic transformation including the resonant term

$$w = z - \frac{h_{20}}{2}z^2 - h_{11}z\bar{z} - \frac{h_{02}}{2}\bar{z}^2 + \frac{1}{2}(3h_{11}h_{20} + 2|h_{11}|^2 + |h_{02}|^2)z^2\bar{z}. \tag{2.47}$$

Taking the time derivative of Eq.(2.47), we get

$$\dot{w} = \dot{z} - h_{20}\dot{z}\dot{\bar{z}} - h_{11}(\dot{z}\bar{z} + z\dot{\bar{z}}) - h_{02}\dot{\bar{z}}\bar{z} + \frac{\Gamma}{2}(2z\dot{z} + z^2\dot{\bar{z}}), \tag{2.48}$$

where $\Gamma = 3h_{11}h_{20} + 2|h_{11}|^2 + |h_{02}|^2$. Next, we substitute the expressions of $\dot{z}$ and $\dot{\bar{z}}$ obtained from Eq.(2.37) into Eq.(2.48). After expanding the resulting equation and collecting terms in z and $\bar{z}$, we obtain

$$\begin{aligned}\dot{w} = \lambda z + (\frac{g_{20}}{2} - \lambda h_{20})z^2 + (\frac{g_{02}}{2} - \bar{\lambda}h_{02})\bar{z}^2 + (-h_{11}\lambda - h_{11}\bar{\lambda} + g_{11})z\bar{z} \\ + \Big(\frac{\Gamma}{2}(2\lambda + \bar{\lambda}) - g_{11}h_{20} - \frac{h_{11}}{2}g_{20} - h_{11}\bar{g_{11}} - \frac{\bar{g_{02}}}{2}h_{02} + \frac{g_{21}}{2}\Big)z^2\bar{z} + \ldots\end{aligned} \tag{2.49}$$

Here, the three dots stand for terms of order three and higher, excluding the resonant term ($z^2\bar{z}$). We now seek to approximate the terms z^2, $z\bar{z}$, $\bar{z}^2$ and $z^2\bar{z}$ with their expansions up to the third order, excluding non-resonant terms at order three. These results in the following order approximations:

$$z^2 = w^2 + 2h_{11}w^2\bar{w} + \ldots, \tag{2.50}$$

$$z\bar{z} = ww_{11} + (\bar{h_{11}} + \frac{h_{20}}{2})w^2\bar{w} + \ldots, \tag{2.51}$$

$$\bar{z}^2 = \bar{w}^2 + \bar{h_{02}}w^2\bar{w} + \ldots, \tag{2.52}$$

$$z^2\bar{z} = w^2\bar{w} + \ldots. \tag{2.53}$$

Substituting these relations into Eq.(2.49), collecting terms in w^2, $w\bar{w}$ and $\bar{w}^2$ and equating their coefficients to zero yield the expressions

$$h_{20} = \frac{g_{20}}{\lambda}, \quad h_{11} = \frac{g_{11}}{\bar{\lambda}}, \quad h_{02} = \frac{g_{02}}{2\bar{\lambda} - \lambda}. \tag{2.54}$$

These equations can be used to selectively eliminate quadratic terms of the desired order. Collecting terms in $w^2\bar{w}$ gives the coefficient

$$c_1 = \frac{3}{2}h_{11}h_{20}(2\lambda+\bar{\lambda}) + (2\lambda+\bar{\lambda})|h_{11}|^2 + \frac{|h_{02}|^2}{2}(2\lambda+\bar{\lambda}) - \frac{1}{2}g_{11}h_{20} + \frac{1}{2}h_{11}g_{20} - h_{11}\bar{g_{11}}$$
$$-\frac{\bar{g_{02}}}{2}h_{02} + \frac{g_{21}}{2} - 2\lambda h_{11}h_{20} + \frac{1}{2}\bar{h_{02}}g_{02} - \bar{\lambda}|h_{02}|^2 - |h_{11}|^2(\lambda+\bar{\lambda}) + g_{11}\bar{h_{11}} - \frac{1}{2}h_{11}h_{20}(\lambda+\bar{\lambda}). \tag{2.55}$$

The above expression reduces to a rather simple form, using the relations of Eq.(2.54), with $\lambda = i\omega$, giving us

$$c_1 = \frac{ig_{20}g_{11}}{2\omega} - \frac{i|g_{11}|^2}{\omega} - \frac{i|g_{02}|^2}{6\omega} + \frac{g_{21}}{2}. \tag{2.56}$$

At this point, any remaining third order terms in Eq.(2.49) can be eliminated similarly using lemma (3.5) of Ref.[74], which concludes the proof. □

Normal form reduction with diffusion, projection method

Assume the formal linear operator ($\mathscr{L}$) of system (2.3) has a pair of purely imaginary eigenvalues $\lambda = i\omega$ and all other eigenvalues lie on the left half of the complex plane. That is

$$\mathscr{L}q = i\omega q, \tag{2.57}$$

where q represents the critical eigenvector belonging to wave mode k. Note also that the linear operator is a function of k. Vector q has the form $q = V\cos kx$, $V \in \mathbb{C}^3$. We define an adjoint linear operator $\mathscr{L}^*$ defined such that

$$\mathscr{L}^* p = -i\omega p, \tag{2.58}$$

such that $p = W\cos kx$, defines the adjoint eigenvector with $W \in \mathbb{C}^3$. The normalization condition $\langle p, q\rangle = 1$ is carried out in an appropriate function space on which $\mathscr{L}$ is compact and bounded.

Assume system (2.3) at criticality can be decomposed as

$$U = zq + \bar{z}\bar{q} + y(z,\bar{z}), \tag{2.59}$$

where q and $\bar{q} \in E^c$, the center subspace and $y \in E^s$, the linear stable subspace. y is the reduction function satisfying $\langle p, y\rangle = 0$.

It follows that

$$z = \langle p, U \rangle, \tag{2.60}$$

$$\text{and } y = U - \langle p, U \rangle q - \langle \bar{p}, U \rangle \bar{q}. \tag{2.61}$$

Taking the time derivative of the previous two equations transforms Eq.(2.3) into

$$\dot{z} = i\omega z + \langle p, F(zq + \bar{z}\bar{q} + y, \delta) \rangle, \tag{2.62}$$

$$\dot{y} = \mathscr{L} y + F(zq + \bar{z}\bar{q} + y, \delta) - \langle p, F(zq + \bar{z}\bar{q} + y, \delta) \rangle q - \langle \bar{p}, F(zq + \bar{z}\bar{q} + y, \delta) \rangle \bar{q}, \tag{2.63}$$

from which the center manifold takes the form $y = f(z, \bar{z})$, satisfying $y(0,0) = 0$ and $D^j y(0,0) = 0$, $|j| \leq 1$. So we may choose y such that

$$y = \frac{r_{20}}{2} z^2 + r_{11} z\bar{z} + \frac{r_{02}}{2} \bar{z}^2 + \mathscr{O}(|z|^3). \tag{2.64}$$

Substituting Eq.(2.64) into Eq.(2.63) and equating terms of the same power we obtain the following boundary value problems:

$$(D\frac{d^2}{dx^2} + A - 2i\omega E) r_{20} = -H_{20}, \tag{2.65}$$

$$(D\frac{d^2}{dx^2} + A) r_{11} = -H_{11}, \tag{2.66}$$

$$(D\frac{d^2}{dx^2} + A + 2i\omega E) r_{02} = -H_{02}, \tag{2.67}$$

$$\frac{dr_{i,j}}{dx}\Big|_{x=0} = \frac{dr_{i,j}}{dx}\Big|_{x=\pi} = 0, \tag{2.68}$$

where,

$$H_{i,j} = \frac{\partial^{i+j}}{\partial z^i \partial \bar{z}^j} F(zq + \bar{z}\bar{q}, \delta)\Big|_{z=0} - G_{i,j} q - \bar{G}_{j,i} \bar{q} \ , i + j = 2 \tag{2.69}$$

$$G_{i,j} = \frac{\partial^{i+j}}{\partial z^i \partial \bar{z}^j} \langle p, F(zq + \bar{z}\bar{q}, \delta) \rangle\Big|_{z=0} \qquad , i + j \geq 2. \tag{2.70}$$

Using the Taylor series decomposition of $F(zq + \bar{z}\bar{q} + y, \delta)$ or its multilinear forms, Eq.(2.32), all vectors $H_{i,j}$ and $G_{i,j}$ can be computed. Eqs.(2.65-2.67) are systems of second order linear ordinary differential equations and as such, their solutions are linear combinations of a general and particular solution. When these functions are determined, so is the reduction

function Eq.(2.64). Substituting the reduction function into Eq.(2.62) yields the restricted equation on the center manifold from which the first Lyapunov coefficient can be computed.

Normal form reduction with diffusion: weakly coupled system

In this subsection, we consider a system of weakly coupled oscillators near a Hopf bifurcation and derive the restricted dynamics in this neighborhood. Consider small perturbations around the homogeneous state of the form $\delta = \delta_c + \alpha$, and $U = U_0 + V$ where $\delta_c = \delta_c(k=0)$. Under these transformations, Eq.(2.3) becomes

$$\begin{aligned} V_t &= (\mu^2 \tilde{D}\Delta + \tilde{A})V + F(U_0 + V, \delta_c + \alpha) \qquad \tilde{\Omega} = [0, \mu\pi], \\ \alpha_t &= 0, \\ \mu_t &= 0, \end{aligned} \tag{2.71}$$

where $\tilde{D} = D_{\delta_c+\alpha}$, $\tilde{A} = A_{\delta_c+\alpha}$ and $\mu > 0$ is a small parameter introduced to re-scale the spatial variable and diffusion coefficient using the transformation $x \to \mu x$. Because the diffusion is now scaled by a small parameter, we are now in the weakly coupled limit.
Close to the Hopf bifurcation of the homogeneous mode, the infinite dimensional center manifold takes the form $y(z, \bar{z}, \alpha, \mu^2)$. The corresponding spectral decomposition becomes

$$U = zq + \bar{z}\bar{q} + y(z, \bar{z}, \alpha, \mu^2) \qquad . \tag{2.72}$$

It follows that the reduced equation on the center manifold has normal form

$$\frac{\partial z}{\partial t} = i\omega_0 z + f_1 \alpha z - f_2 z|z|^2 + \mu^2 f_3 \Delta z + \ldots, \tag{2.73}$$

where

$$f_1 = \langle p, \frac{\partial \tilde{A}}{\partial \alpha}\Big|_{\alpha=0} q \rangle, \tag{2.74}$$

$$f_2 = -\langle p, B(q, y_{1100}) + B(\bar{q}, y_{2000}) + \frac{1}{2}C(q, q, \bar{q}) \rangle, \tag{2.75}$$

$$f_3 = \langle p, D_{\delta_c} q \rangle, \tag{2.76}$$

in which,

$$y_{1100} = -\mathscr{L}^{-1}B(q,\bar{q}), \tag{2.77}$$

$$y_{2000} = -\frac{1}{2}(\mathscr{L} - 2i\omega_0)^{-1}B(q,q), \tag{2.78}$$

$$B(\bar{q},y_{2000}) = \begin{pmatrix} 0 \\ -2\delta_c u^* \bar{q}_1 y^{(1)}_{2000} \\ 0 \end{pmatrix}, \tag{2.79}$$

$$B(\bar{q},y_{1100}) = \begin{pmatrix} 0 \\ -2\delta_c u^* q_1 y^{(1)}_{1100} \\ 0 \end{pmatrix}, \tag{2.80}$$

where $y^{(n)}_{ijkl}$ represents the n^{th}-component of y_{iklm}. Here, $B(U,V)$ and $C(U,V,W)$ are symmetric multilinear functions defined according to Eqs.(2.32). Note that in this case, $\mathscr{L}$ and the eigenfunctions q and p are evaluated at $k = 0$ and $\alpha = 0$. For more information on the derivation of these operators and other useful formulas consult Appendix A.1.

By introducing the following scaling transformations $t \to \mu^2 t$, $z \to ze^{i\omega_0 t}$ and setting $\alpha = -\mu^2$ we obtain the CGL as

$$\frac{\partial z}{\partial t} = -f_1 z - f_2 z|z|^2 + f_3 \Delta z, \tag{2.81}$$

ignoring higher order terms. The choice of $\alpha = -\mu^2$ is by assumption that the direction of instability is $\alpha < 0$. For a supercritical Hopf bifurcation of mode $k = 0$, the exact form of the CGL will be of cubic form without quintic or higher order terms which must be present if the bifurcation is subcritical. Further assume $f_{1r} < 0$ and $f_{3r} > 0$. With another set of set of transformations namely: $t \to -f_{1r}t$, $x \to \sqrt{\frac{-f_{1r}}{f_{3r}}}x$ and $z \to \frac{-f_{1r}}{f_{2r}}e^{i\frac{f_{1i}}{f_{1r}}t}z$, Eq.(2.81) can be rewritten in its pervasive form:

$$\frac{\partial z}{\partial t} = z - (1+ic_2)|z|^2 z + (1+ic_1)\Delta z, \tag{2.82}$$

with $c_2 = \frac{f_{2i}}{f_{2r}}$ and $c_1 = \frac{f_{3i}}{f_{3r}}$.

The G'/G expansion method

The G'/G expansion method is a popular method used to obtain exact traveling wave solutions to certain class of nonlinear partial differential equations (PDE's). It is relatively easy to implement on simple PDE's and was our method of choice to obtain front wave

solutions for the hyperbolic FHN model, without the recovery variable. The classical FHN model in addition to pulse or periodic wave solutions, possesses front wave solutions in the absence of the recovery variable [93]. By neglecting the recovery variable, boundary conditions and I in Eq.(2.1) ($v = 0$), we obtain a single partial differential equation of the form:

$$P(u, u_x, u_t, u_{xx}, u_{xt}, u_{tt}, \dots) = 0 \tag{2.83}$$

The G'/G expansion method can be used to find exact solitary solutions of Eq.(2.83) in the form of trigonometric or hyperbolic trigonometric functions as follows:

— **Step 1**: Introduce a change of variables by letting $u(x,t) = u(\xi)$, where $\xi = x - ct$. This transforms Eq.(2.83) into an ordinary differential equation:

$$Q(c, u', u'', u''', \dots) = 0. \tag{2.84}$$

— **Step 2**: We seek solutions of Eq.(2.84) as a power series of the function G'/G as follows:

$$u(\xi) = \sum_{m=0} \alpha_m (\frac{G'}{G})^m + \dots, \tag{2.85}$$

where $\alpha_m \neq 0$ and the $\dots$ represent terms of order $m-1$ and lower. $G(\xi)$ is assumed to be the solution of the second order ordinary differential equation:

$$G'' + \lambda G' + \mu G = 0, \tag{2.86}$$

where λ and μ are constant to be determined. The integer m is determined by balancing terms in the highest order derivative and highest order nonlinear terms in $Q(u(\xi))$.

— **Step 3**: Substituting Eq.(2.85) into Eq.(2.84), making use of Eq.(2.86) and collecting like terms of order $(\frac{G'}{G})$ (setting each of these terms to zero), we obtain a system of equations with unknowns, α_m, c, λ, and μ.

— **Step 4**: Next we use a computer algebraic software such as MAPLE to solve the system of equations obtained in step 3 and substitute the solutions into Eq.(2.86). We then find the general solutions of this equation which we replace into Eq.(2.85), to obtain traveling waves solutions.

The direct integration method

The direct integration approach is a simple method used to find exact solutions to equations similar to Eq.(2.84) by simply integrating this equation a number of timse and

setting the integration constants to zero. We used this method to find exact solutions to oscillons of the CGL similar to that obtained in Eq.(2.73). To demonstrate this method, let us assume we are precisely at the critical Hopf bifurcation point ($\alpha = 0$) and that Eq.(2.73) has been rescaled to remove the frequency(ω). That is, We consider the CGL of the form

$$iA_t + PA_{\xi\xi} + Q|A|^2 A = 0, \tag{2.87}$$

where P and Q are generally complex coefficients. We assume solutions of this equation of the form

$$A(\xi,t) = f(z)e^{i(m\xi - nt)}, \qquad z = \xi + Vt \tag{2.88}$$

where m and n are parameters and V is the speed of the wave. Substituting this into Eq.(2.87), we obtain

$$i(Vf' - inf) + (P_r + iP_i)\left[f'' + 2imf' - m^2 f\right] + (Q_r + iQ_i)f^3 = 0, \tag{2.89}$$

where, $f' = \frac{\partial f}{\partial z}$. This equation further be separated into real and imaginary parts as

$$nf + P_r(f'' - m^2 f) - 2mP_i f' + Q_r f^3 = 0, \tag{2.90}$$

$$Vf' + 2mf'P_r + P_i(f'' - m^2 f) + Q_i f^3 = 0. \tag{2.91}$$

Eliminating f' from this two equations, we obtain

$$(n - P_r m^2 - \gamma P_i m^2)f + (P_r + \gamma P_i)f'' + (\gamma Q_i + Q_r)f^3 = 0, \tag{2.92}$$

with $\gamma = \frac{2mP_i}{2mP_r + V}$. Multiplying by f' and integrating once, we obtain

$$-Ff^2 + Gf'^2 + \frac{H}{2}f^4 = c_1, \tag{2.93}$$

where, c_1, is a constant of integration which we set to zero, in requirement with properties of a solitary solution. The constants F, G, and H are given by

$$F = m^2(P_r + \gamma P_i) - n^2, \tag{2.94}$$

$$G = P_r + \gamma P_i, \tag{2.95}$$

$$H = \gamma Q_i + Q_r. \tag{2.96}$$

Making f' the subject in Eq.(2.93), we have

$$\frac{\sqrt{2G}f'}{f(\sqrt{2F-Hf^2})}=1, \tag{2.97}$$

where, $\frac{2F-Hf^2}{2G}>0$. Letting $2F-Hf^2=g^2$, this equation can be transformed into the following (relatively easier to integrate) equation

$$\frac{\sqrt{2G}g'}{2F-g^2}=-1. \tag{2.98}$$

The latter can be integrated by partial fraction technique by separating in the form

$$\sqrt{\frac{G}{F}}\left(\frac{1}{(\sqrt{2F}+g)}+\frac{1}{(\sqrt{2F}-g)}\right)g'=-2. \tag{2.99}$$

After integration and simplification, we obtain

$$g=-\sqrt{2F}tanh\left(\sqrt{2F}c_2+\sqrt{\frac{F}{G}}z\right), \tag{2.100}$$

where, c_2 is a constant of integration. Expressing f in terms of g, we have

$$f=\sqrt{\frac{2F}{H}}sech\left(\sqrt{2F}c_2+\sqrt{\frac{F}{G}}z\right), \tag{2.101}$$

and the solitary solution

$$A=\sqrt{\frac{2F}{H}}sech\left(\sqrt{2F}c_2+\sqrt{\frac{F}{G}}z\right)e^{i(m\xi-nt)}. \tag{2.102}$$

The multiple scale expansion method

The multiple scale expansion method is a reductive method similar to the center manifold reduction method. This method exploits the fact that the dynamics on the center manifold is generally slower than the dynamics on the complementary space. As a result, a time separation can be imposed on the system in the neighborhood of a nonhyperbolic equilibrium. Spatial variations are also assumed to be slow on this manifold.

We introduce slow time and space variables as follows

$$\xi=\delta x, \qquad T=\delta t, \qquad \tilde{\tau}=\delta^2 t, \tag{2.103}$$

where $\delta << 1$ is a small parameter which represents a small deviation from the steady state of Eq.(2.1). Next, we expand the membrane potential and recover variables , in a Fourier and power series of unstable modes in δ of the form:

$$\mathbf{U} = \sum_{n=1}^{3} \delta^n \mathbf{U}_n^{\tilde{p}} e^{i\tilde{p}\varphi}, \tag{2.104}$$

where $\mathbf{U} = (u,v)^T$, $-2 \leq \tilde{p} \leq 2$, $\tilde{p} \in \mathbb{Z}$, and $\varphi = kx - \omega t$. Here, φ represents the phase of the propagating wave, $\tilde{p}$ its harmonic, k its wavenumber, and ω its frequency.
We consider the most unstable mode at threshold to be a slowly moving wave, having the following ansatz

$$\mathbf{U} = \mathbf{U}_1(\xi, T, \tilde{\tau}) e^{i\varphi} + c.c, \tag{2.105}$$

where $\mathbf{U}_1$ as well as $\mathbf{U}_n^{\tilde{p}}$ are functions of the slow time and space variables. In terms of the slow variables, the time and space derivatives of Eq.(2.1) take the form:

$$\begin{aligned} U_{xx} &= -k^2\tilde{p}U + 2\delta U_{x\xi} + \delta^2 U_{\xi\xi}, \\ U_t &= -i\omega\tilde{p}U + \delta U_T + \delta^2 U_{\tilde{\tau}}, \\ U_{tt} &= -\omega^2\tilde{p}^2 U + 2\delta U_{Tt} + U_{\tilde{\tau}t} + 2\delta^3 U_{T\tilde{\tau}} + \delta^2 U_{TT} + \delta^4 U_{\tilde{\tau}\tilde{\tau}}. \end{aligned} \tag{2.106}$$

Substituting Eqs.(2.106) into system (2.1) and collecting terms of different orders of δ, we can obtain information about the linear stability of the wave state and obtain other useful information. At higher orders of this procedure, we obtain the complex Ginzburg-Landau (CGL) equation from which we can easily build exact solitary solutions. Full details about the approach used here can be found in Ref.[97]. The advantage of the multiple scale expansion is that it yields the CGL naturally without reference to bifurcation points, boundary conditions and other critical parameters. We have therefore used this technique to find analytical solutions to oscillons.

2.3.2 Numerical methods

Finite difference approximation of the hyperbolic FHN

One of the desirable attributes of a discrete model, obtained from a continuous one, is its ability to conserve the quality and quantity of solutions, and bifurcations of the continuous mode. This is because discretization often induces new bifurcations and solutions that differ from those of the original system. As such we considered two discretization schemes for the hyperbolic FHN model, given in Eq.(2.2). First, a discretization in space to reproduce the its

main bifurcations, followed by a discretization in time to mimic the temporal behavior of the model without diffusion ($D = 0$).

Discretization in space

Here, we discretize the diffusion term u_{xx} in Eq.(2.2) using a centered finite difference scheme as

$$u_{xx} = \frac{u_{i+1} - 2u_i + u_{i-1}}{h^2}. \tag{2.107}$$

We consider a neuron of length $\ell = 1$, discretized using $N \geq 3$, nodal points with space step $h = 1/N - 1$. Next we discretize the boundary conditions on $\Omega = [0, \ell]$ with a second order scheme as

$$\begin{aligned} u_x|_{x=0} &= \frac{4u_1 - u_2 - 3u_0}{2h}, \\ u_x|_{x=1} &= \frac{4u_{N-2} - u_{N-3} - 3u_{N-1}}{2h}, \end{aligned} \tag{2.108}$$

where u_0 and u_{N-1} represent the potential at the leftmost and right nodes respectively. Details for the formulas in Eq.(2.108) can be found in Ref.[110]. Setting the right hand sides of Eq.(2.108) to zero, we obtained the expressions of the boundary nodal voltages u_0 and u_{30}. Putting everything together, Eq.(2.2) becomes

$$\begin{aligned} u_i' &= w_i \qquad\qquad \text{in } \Omega = [0,1], \\ w_i' &= \frac{1}{\tau}\left(\frac{d(u_{i+1} - 2u_i + u_{i-1})}{h^2} + u_i - \frac{u_i^3}{3} - v_i - w_i\right), \\ v_i' &= \varepsilon(u_i + a - bv_i) \qquad \text{for } i = 1 \ldots N-2, \\ u_0 &= \frac{4u_1 - u_2}{3}, \\ u_{N-1} &= \frac{4u_{N-2} - u_{N-3}}{3}, \end{aligned} \tag{2.109}$$

where as before, we set $u_i' = w_i$, where the primes denote differentiation with respect to time. Additionally, the boundary conditions imposed on u also apply to v.

Discretization in time

We now consider Eq.(2.2), ignoring the effect of diffusion and boundary conditions. We discretize the time variable as follows:

$$\begin{aligned} u_{j+1} &= u_j + wdt, \\ w_{j+1} &= w_j + \frac{dt}{\tau}(u_j - \frac{u_j^3}{3} - v_j - w_j + I), \\ v_{j+1} &= v_j + \varepsilon dt(u_j + a - bv_j), \end{aligned} \tag{2.110}$$

where dt is the time step for the forward Euler method.

Numerical bifurcation and continuation software

In this thesis we used MATCONT, version 7.1, as the only too for numerical bifurcation and continuation analysis of the various models encountered throughout this thesis. MATCONT is a MATLAB based toolbox for the numerical bifurcation bifurcation analysis of ODE's featuring standard protocols for numerical bifurcation analysis. Examples of these protocols, those used in this thesis include:

— Fixed point location via methods such Newton's method and variants.

— Fixed point stability analysis.

— Codimension one bifurcation analysis.

— Codimension two bifurcation analysis.

Full details about the implementation of these protocols in the software , MATCONT can be found in Chapter 10, Ref.[74] for ODE's and in Ref.[78] for maps or discrete differential equations.

2.4 Conclusion

In this chapter we have reviewed both the hyperbolic FHN model and a photosensitive variant of this model. We provided detailed descriptions of their structure, boundary conditions and derived where applicable the governing equations from first principles. We also reviewed the main methods (analytical and numerical) applied to both models in this thesis. The center manifold theorem, underpinning most of this thesis was reviewed in this chapter as well as corresponding methods allowing for the reduction of the dynamics to such invariant manifolds. A brief review of a few relevant analytical methods in constructing exact solitary

solutions was also conducted. These methods were selected on the basis of their suitability to the problem at hand and their ease of implementation.

Chapter 3

Results and discussions

In this chapter, we present the following results: bifurcation analysis of the continuous and discrete hyperbolic FHN models with and without diffusion, analysis of the front and oscillon solutions of the hyperbolic FHN model, and lastly, burst synchronization in two coupled photosensitive hyperbolic FHN models; under different coupling schemes.

The first part of these results concerns the bifurcation analysis of the local kinetic system of the hyperbolic FHN model with the relaxation time as the principal bifurcation parameter. This analysis reveals a threshold of the relaxation constant beyond which a supercritical Hopf bifurcation occurs. Analytical estimates of the first Lyapunov coefficient are confirmed via numerical simulations. A codimension-two bifurcation diagram of the relaxation time and the excitable current reveals: regions of bistability (with the possibility of two types of bursting), quiescence, periodic firing with periods one, two, three, and four. Chaotic regions are also present at higher values of the relaxation time. Despite the addition of the hyperbolic time derivative, the hyperbolic model is shown to preserve the typical bifurcation diagrams of the classical FHN model, at subthreshold values of the relaxation time.

The second part of our results is on the bifurcation analysis of the hyperbolic FHN model with the diffusion parameter. We obtain general results for the Pitchfork and Hopf bifurcation in terms of the diffusion parameter, length of the neuron, wavenumber, and relaxation time. The first Lyapunov coefficient is computed analytically for the mode $k = 1$, assuming a strong diffusion coefficient. For the weakly coupled case, numerical simulation of the nonlinear wave states of the system shows that the uniform oscillatory state is stable against long-wave perturbations, indicating full synchronization. Pitchfork bifurcations are independent of the relaxation time and induced by negative diffusion. For all wave modes, it is shown that the square of the wave speed varies inversely with the relaxation time, in contrast to the classical FHN model.

Part three of the results concerns the bifurcation analysis of the discrete FHN model with space and time discretizations. We show that most of the bifurcations induced in the continuous model persist in the discrete model. For the discretiztion in space, a centered finite difference was used while the simple Euler method was used for discretizations in time. In both cases, the discrete system obtained is an ODE whose bifurcations are faithful to the continuous model.

Part four of this chapter presents results on the analysis of front and pulse solutions of the hyperbolic FHN model. The effect of the time of relaxation on the profiles of these solutions is analyzed via analytical and numerical methods. We construct exact front solitary solutions using the $G'/G-$ method and the direct integration for the oscillon. For both solitary waves, analytical estimates suggest that a maximum speed of propagation exists, and corresponds to the speed at vanishing relaxation time. As with periodic waves the square of the speeds of solitary waves vary inversely with the increasing magnitude of the relaxation time.

The last part of our results concerns the analysis of the origin of bursting in the photosensitive hyperbolic FHN model, and burst synchronization between two coupled photosensitive neurons through different coupling schemes. We establish in two-dimensional parameter space, regions of quiescence, periodic spiking, and bursting. We show that two types of bursting are possible for such a system as per the unfolding in the neighborhood of a Bautin bifurcation. By focusing on elliptic bursting, we establish via numerical simulations, regions of coupling strengths favorable to burst synchronization using electrical, excitatory, or inhibitory synaptic coupling. This synchronization may involve either in-phase or anti-phase spike synchronization, depending on the type of coupling used. Furthermore, we observe that certain intervals of coupling strength induce amplitude death, and burst destruction.

This rest of this chapter is organized as follows: Section 3.1 reviews some key terms and previous results or studies relevant to the results obtained in this thesis. Section 3.2 presents results on the bifurcation analysis of the hyperbolic FHN model, in the absence of diffusion. In section 3.3 we include the diffusion term and present results on the Hopf and Pitchfork bifurcations of the hyperbolic model. Section 3.4 discusses the results of the bifurcation analysis of the hperbolic FHN model with discrete time and space dynamics. The effect of the time of relaxation on the properties of fronts and oscillons is presented in section 3.5. Results on bursting and burst synchronization in two coupled light sensitive hyperbolic neurons is presented in section 3.6. A conclusion to the chapter is presented in section 3.7.

3.1 Introduction and background

Stability analysis in dynamical systems plays a key role in predicting under what parameter ranges qualitatively distinct behaviors emerge and the system's asymptotic behavior. The emergence of periodic or oscillatory behaviors seems to be of particular interest due to their wide range of applications. The pervasiveness of oscillations in brain circuitry and its importance cannot be overstated. Oscillations in neurons play diverse roles in the nervous system, from trivial cell-to-cell communications via action potentials to more complex spatial organization tasks such as the formation of Hebbian cell assemblies, believed to be the basic unit of information storage in the brain as pointed out in Ref.[37]. The most common route leading to periodic behavior, and often encountered in excitable systems, is the Hopf bifurcation (section 1.4.1), extensive treatise of which can be found in Refs.[111, 112]. Seminal works on the Hopf bifurcation can be traced back to the works of Poincaré , Andronov , Hopf and others [111]. The limit cycle born (destroyed) from the Hopf bifurcation may be stable or unstable. If the cycles emerge before the critical parameter value, the Hopf bifurcation is termed subcritical. If on the contrary, the cycles emerge post-critical value, we say a supercritical Hopf bifurcation has taken place. Subcritical Hopf bifurcations may be undesirable in some systems as they tend to be irreversible and lead to large excursions from steady states. Hence assessing the direction of the Hopf bifurcation is of prime importance, from a structural stability standpoint.

Based on the nature of the bifurcation at a critical parameter value, models of single neurons can be compartmentalized into two main types (see Ref.[113]), the so-called bifurcation types -1 and -2 neurons [29]. A bifurcation of type-1 generally occurs when the equilibrium loses stability via a saddle-node bifurcation on an invariant circle. Bifurcation type-2 neurons, also called resonators, lose stability via Hopf bifurcations. They fire in response to stimulating frequencies equal to their resonant frequency [114, 27]. In addition to their sensitivity to the frequency of an external stimulation , one feature, common to bifurcation type-2 neurons , in contrast to type-1 neurons, and which we shall observe subsequently, is their ability to fire post-inhibitory pulses [27]. This is the result of the unstable manifold being warped around the stable equilibrium making it more likely for small perturbations to drive the system into instability.

As discussed in Chapter 1.4.1, a limit cycle can undergo bifurcations of its own such as fold or limit point of cycle bifurcation, flip or period-doubling bifurcation, Neimark-Sacker bifurcation of cycles (bifurcations on an invariant torus), and canard explosions [115]. The latter corresponds to a rapid transition in the period of a limit cycle, from a small value to a large value over a very small range of the bifurcation parameter. The period-doubling

bifurcation (See section 1.4.1) is one of the most studied routes to chaos; via period-doubling cascades. This bifurcation has been observed in other variants of the FHN model[116, 117].

Much of what we know about the brain comes from experimental measurement, achieved via electroencephalogram (EEG) and related techniques. This technique consists of mapping a given spatially coherent brain activity to a specific brain function or pathology [118, 119]. As such, if one desires to study more intricate brain functions, and the collective behavior of neurons, one must take into account the spatial coupling of neurons via diffusive effects. The interaction of diffusing species in extended systems often leads to complex and interesting spatial patterns with specific implications. The study of such patterns forms the core of the subject— pattern formation. Pattern formation in spatially extended systems has been the source of intense research over the last century [35, 120, 121], and the mathematical methods which emerged from its study have been successfully applied to explain the dynamics of oscillatory and stationary patterns in chemical and biological systems. Pattern formation in biological systems continues to be an active area of research as evidenced by recent studies: The effect of magnetic flow [122, 123], temperature fluctuations [124], diffusion [125, 126] , on a network of spatially coupled FHN units have been addressed. Hopf and Pitchfork bifurcations in two-dimensional coupled bulk surfaces of general reaction diffusion systems were recently addressed in Ref.[127]; just to name a few.

Models of discrete time or space dynamics commonly called maps, have been the subject of multiple studies in dynamical systems theory. Maps are sometimes derived in situations where a continuous approximations seems inadequate. For example, changes in population sizes are best described by discrete time dynamics. Although maps share similar bifurcations with continuous models, they typically have very complex bifurcation scenarios, even for the simplest one dimensional maps[78]. Numerical bifurcation analysis of the time discrete FHN model was conducted by Jing et al.[128]. In that study, the authors used a forward Euler discretization on the time variable. The nearly exact discretization (NEDS) in time, recently proposed by Kwessi et al.[129], was used to study the continuous FHN model [130]. They showed that NEDS preserved the quantitative and qualitative dynamics of the continuous FHN.

The clasical FHN possesses solitary waves or different types: fronts, pulse, pulse with oscillatory tails, and much more[74]. In Refs.[22, 23, 23], the authors studied pulse solitary waves of the hyperbolic FHN model and showed that this model does not allow for solitons of infinite speeds to propagate. That is, for any given value of the relaxation time, there is an upper limit of possible wave speeds for soliton propagation. Using the G'/G-method, Muhammad et al.[131] built exact front solutions for a hyperbolic diffusion model known as the generalized telegraph equation. Ebadi et al.[132] and Elagan et al. [133] built exact

solution for the FHN model with nonlinear source terms. However, analytical solutions for fronts and pulse solutions of the telegraph FHN model are currently not available, to the best of our knowledge. Solitary waves may also become unstable via a Hopf bifurcation to form a jumping soliton (oscillon) with oscillating amplitude [134, 135]. The exact solutions and the effect of the time of relation on the profiles of the fronts and the oscillons of the hyperbolic FHN model have not been researched at this time.

The classical photosensitive FHN neuron proposed by Liu and colleagues [81] allows for the fine tuning of the complex firing pattern of the model by light-dependent signals. The authors were able to show that the photocurrents induced in the phototube could induce various spiking dynamics in the neuron such as chaotic, periodic spiking, and bursting. In a follow-up study [136], they showed that networks of spiking photosensitive neurons could synchronize within certain values of the coupling strength, light intensity, and frequency. However, the full range of parameter values within which the aforementioned dynamical behaviors may be observable was not specified. Furthermore, the authors did not address the issue of burst synchronization in coupled photosensitive neurons.

Synchronization of coupled systems and neurons has been studied extensively over the years [137]. The goal has been to understand how such systems collectively process and transmit information. A key factor in this understanding is the knowledge of how the properties of a given neuron are affected by the external signal. Such a signal may be from background noise, other neurons' activities, electromagnetic radiation [138, 139], injected current, or some other current source. Furthermore, this signal may be constant, periodic, or aperiodic. Also of great importance is the notion of burst synchronization[29]. Although much more difficult to analyze analytically, burst synchronization in elliptic bursters happens to be amenable to analytical analysis. Izhikevich [76] studied burst synchronization in weakly coupled elliptic bursters, using the normal form of the Bautin bifurcation. Azad et al. [77] extended this analysis to higher-order normal form terms. From the previous two references, it was found that burst synchronization was easier to achieve for electrical and other synaptic coupling schemes (excitatory or inhibitory). Spike synchronization on the other hand was possible only under certain coupling schemes. Synchronization in elliptic bursters has also been studied under nonlinear coupling [140] and a host of other schemes [141]. However the synchronization of light dependent elliptic bursters has not been addressed in previous research studies, to the best of our knowledge.

3.2 Linear stability and Hopf bifurcation in the absence of diffusion

3.2.1 Linear stability analysis and Hopf bifurcation for $k = 0$

We consider the modified FHN model given by Eq.(2.2), in the absence of the diffusion term (and boundary conditions). In the absence of stimulation I, this model is equivalent to the system of three autonomous ODE's:

$$\begin{aligned} u_t &= w, \\ \tau w_t &= u - \frac{u^3}{3} - v - w, \\ v_t &= \varepsilon(u + a - bv). \end{aligned} \tag{3.1}$$

The equilibria of this system correspond to the spatially homogeneous equilibria, Eq.(2.15). Applying lemma 1 to Eq.(2.16), we obtain the discriminant

$$D = \frac{-108(1-b)^3 - 243a^2b}{b^3}. \tag{3.2}$$

For the sake of simplicity, we shall consider the unique stable equilibrium for the study of Hopf bifurcations. Eq.(3.2) under lemma 1, implies that system (3.1) possesses a unique equilibrium, satisfying $108(1-b)^3 + 234a^2b > 0$. Choosing $0 < b < 1$, $\forall a \geq 0$ is enough to guarantee this condition.

Notice that the location of the steady state is independent of τ , our chosen bifurcation parameter which makes it ideal for the reduction to the center manifold as demonstrated subsequently.

Eq.(3.1) can be put in the form

$$\begin{aligned} X_t &= Y, \\ Y_t &= \delta\left[(1-u^{*2})X - u^*X^2 - \frac{X^3}{3} - Y - Z\right], \\ Z_t &= \varepsilon(X - bZ), \end{aligned} \tag{3.3}$$

where $X = u - u^*$, $Y = w - w^*$, $Z = v - v^*$, and $\delta = \frac{1}{\tau}$. Here, (u^*,w^*,v^*) represent the unique uniform steady state. We are interested in the onset of nonlinear oscillations in system (3.1), under the influence of the relaxation constant. Since we are in $\mathbb{R}^3$ and generic Hopf bifurcations are analytically defined for two-dimensional systems, we make use of the

reduction techniques from the center manifold theory to prove that Hopf bifurcations do exist for our system at large values of the relaxation constant. We follow the guidelines of the projection method in the absence of the diffusion (see section 2.3.1).

Consider the Jacobian (A) of system (3.1):

$$A = \begin{pmatrix} 0 & 1 & 0 \\ \delta(1-u^{*2}) & -\delta & -\delta \\ \varepsilon & 0 & -\varepsilon b \end{pmatrix}. \tag{3.4}$$

Its characteristic polynomial is obtained as

$$\lambda^3 + (b\varepsilon + \delta)\lambda^2 + (b\varepsilon + u^{*2} - 1)\delta\lambda + (bu^{*2} - b + 1)\varepsilon\delta = 0. \tag{3.5}$$

Applying Theorem 1 to Eq.(3.5), we obtain $a_3 > 0$, $\Delta_2 = 0$ and $\Delta_1 > 0$ as three conditions necessary for a Hopf bifurcation to occur in the system under study. Its easy to verify the first and third relations by inspection. Applying the second condition ($\Delta_{n-1} = 0$) to the third 2^{nd}-order Hurwitz determinant of Eq.(3.5), we obtain

$$b\varepsilon(\varepsilon b + u^{*2} - 1) - \varepsilon(bu^{*2} - b + 1) = 0, \tag{3.6}$$

and after a short algebraic manipulation, we arrive at the critical value

$$\delta_c = \frac{\varepsilon - b^2\varepsilon^2}{\Lambda}, \tag{3.7}$$

where $\Lambda = \varepsilon b + u^{*2} - 1$. Let $\alpha = \delta - \delta_c$ be the distance away from the bifurcation point, then we can say, at $\alpha = 0$, a Hopf bifurcation takes place. We will show that a stable limit cycle indeed bifurcates from the unique stable fixed point for values of $\alpha < 0$ while the origin maintains its equilibrium for $\alpha > 0$.

To establish the frequency of these limit cycle oscillations, we proceed as follows. We substitute $\lambda = i\omega$ into Eq.(3.5) and separate the resulting equation into real and imaginary parts, to obtain

$$b\varepsilon\delta(u^{*2} - 1) - (b\varepsilon + \delta)\omega^2 + \delta\varepsilon = 0, \tag{3.8}$$

$$\omega^3 - \Lambda\delta\omega = 0, \tag{3.9}$$

with $\Lambda = \varepsilon b + u^{*2} - 1 > 0$. From these two equations, we obtain

$$\delta_c = \frac{\omega^2}{\Lambda}, \text{ and } \omega^2 = \varepsilon - b^2\varepsilon^2. \tag{3.10}$$

The first equation on the left corresponds to the value of δ_c predicted by Theorem 1 while the second equation is the frequency of the resulting oscillations ($\omega > 0$). Under these conditions, Eq.(3.5) can be written as

$$(\lambda + b\varepsilon + \delta_c)(\lambda^2 + \omega^2) = 0, \tag{3.11}$$

which is then solved for the third eigenvalue of A, at the critical point, having solution

$$\lambda_3 = -\frac{(bu^{*2} - b + 1)\varepsilon}{\Lambda} < 0, \tag{3.12}$$

which predicts that all asymptotic solutions converge on the center manifold.

3.2.2 Direction of Hopf bifurcation for $k = 0$

To begin investigations of orbital stability on the center manifolds, we express the Jacobian of the system at the critical point, in terms of δ_c. Let us call this matrix $A(\omega)$

$$A(\omega) = \begin{pmatrix} 0 & 1 & 0 \\ \frac{\omega^2(1-u^{*2})}{\Lambda} & -\frac{\omega^2}{\Lambda} & -\frac{\omega^2}{\Lambda} \\ \varepsilon & 0 & -\varepsilon b \end{pmatrix}. \tag{3.13}$$

Using the notation of section 2.3 on the center manifold theory, we associate to matrix $A(\omega)$, the integers : $n_0 = 2$, $n_+ = 0$, $n_- = 1$, such that for sufficiently small α, Theorem 2, predicts the existence of a two dimensional local attracting center manifold $W^c_{loc}(0)$. The resulting manifold is obviously dependent on δ.

Given the slightly complex nature of matrix $A(\omega)$, we use MAPLE software to find its eigenvectors. It follows that

$$q = \begin{pmatrix} \frac{\varepsilon b^2 - 1}{i\omega(1 - \varepsilon b^2 + i\omega b)} \\ \frac{\varepsilon b^2 - 1}{1 - \varepsilon b^2 + i\omega b} \\ 1 \end{pmatrix} \text{ and } \tilde{p} = \begin{pmatrix} \frac{\Lambda + i\omega}{1 - \varepsilon b^2 - i\omega b} \\ \frac{-\Lambda}{i\omega(1 - \varepsilon b^2 - i\omega b)} \\ 1 \end{pmatrix}. \tag{3.14}$$

In order to satisfy the normalization condition, we choose a constant $\nu = \langle \tilde{p}, q \rangle$ such that $\langle p, q \rangle = 1$. Where $\langle , \rangle$ is the standard scalar product in $\mathbb{C}^3$. Hence we can take $p = \frac{1}{\nu}\tilde{p}$.

At δ_c, we can express system (3.1) in the form given by Eq.(2.30). Using the multilinear functions, Eq.(2.32), we evaluate:

$$B(q,q) = \begin{pmatrix} 0 \\ -2\delta u^* q_1^2 \\ 0 \end{pmatrix}, \; B(q,\bar{q}) = \begin{pmatrix} 0 \\ -2\delta u^* q_1 \bar{q}_1 \\ 0 \end{pmatrix}, \tag{3.15}$$

$$B(\bar{q},\bar{q}) = \begin{pmatrix} 0 \\ -2\delta u^* \bar{q}_1{}^2 \\ 0 \end{pmatrix}, \text{ and } C(q,q,\bar{q}) = \begin{pmatrix} 0 \\ -2\delta q_1^2 \bar{q}_1 \\ 0 \end{pmatrix}.$$

The normal form coefficients of Eq.(2.37) then become

$$g_{20} = -2\delta u^* \bar{p}_2 q_1^2, \tag{3.16}$$

$$g_{11} = -2\delta u^* \bar{p}_2 q_1 \bar{q}_1, \tag{3.17}$$

$$g_{02} = -2\delta u^* \bar{p}_2 \bar{q}_1{}^2, \tag{3.18}$$

$$g_{21} = -2\delta \bar{p}_2 q_1^2 \bar{q}_1 + 4\delta u^* \bar{p}_2 q_1 s_1 - 2\delta u^* \bar{p}_2 \bar{q}_1 r_1 + \frac{1}{i\omega} g_{20} g_{11} - \frac{2}{i\omega}|g_{11}|^2 - \frac{1}{3i\omega}|g_{02}|^2. \tag{3.19}$$

Matrices r and s are 3×1 matrices given by

$$s = A(\omega)^{-1} B(q,\bar{q}), \quad \text{and} \quad r = (2i\omega E - A(\omega))^{-1} B(q,q), \tag{3.20}$$

with matrix E being the identity matrix in $\mathbb{R}^3$. The inverse matrix $A(\omega)^{-1}$ has the form

$$A(\omega)^{-1} = \begin{pmatrix} \frac{-b}{b(u^{*2}-1)+1} & \frac{-b\Lambda}{\omega^2(b(u^{*2}-1)+1)} & \frac{1}{\varepsilon(b(u^{*2}-1)+1)} \\ 1 & 0 & 0 \\ \frac{-1}{b(u^{*2}-1)+1} & \frac{-\Lambda}{\omega^2(b(u^{*2}-1)+1)} & -\frac{u^{*2}-1}{\varepsilon(b(u^{*2}-1)+1)} \end{pmatrix}. \tag{3.21}$$

Since matrices B and C happen to be in a simplified form, r and s will also simplify to

$$s = \begin{pmatrix} \frac{2bu^* q_1 \bar{q}_1}{b(u^{*2}-1)+1} \\ 0 \\ \frac{2u^* q_1 \bar{q}_1}{b(u^{*2}-1)+1} \end{pmatrix}, \quad \text{and } r = \frac{-2u^* q_1^2 \bar{\zeta}}{|\zeta|^2} \begin{pmatrix} (2i\omega + \varepsilon b) \\ 2i\omega(2i\omega + \varepsilon b) \\ \varepsilon \end{pmatrix}, \tag{3.22}$$

where ζ is a complex number expressed as

$$\zeta = 2i(2i\omega + \varepsilon b)(2i\Lambda + \omega) + (2i\omega + \varepsilon b)(u^{*2} - 1) + \varepsilon. \tag{3.23}$$

To determine whether the ensuing oscillations are supercritical (subscritical), we compute the first Lyapunov coefficient from the reduced normal form coefficient c_1 from Eq. (2.56). This coefficient is related to the first Lyapunov coefficient $l_1(\delta_c)$ as

$$\begin{aligned} l_1(\delta_c) &= \frac{\mathrm{Re}(c_1)}{\omega}, \\ &= \frac{1}{2\omega}\mathrm{Re}\left[\langle p, C(q,q,\bar{q})\rangle - 2\langle p, B(q,s)\rangle + \langle p, B(\bar{q},r)\rangle\right] \\ &= \frac{1}{2\omega}\mathrm{Re}\left(-2\delta\bar{p}_2 q_1^2\bar{q}_1 + 4\delta u^*\bar{p}_2 q_1 s_1 - 2\delta u^*\bar{p}_2\bar{q}_1 r_1\right). \end{aligned} \tag{3.24}$$

In order to keep τ within a range consistent with the Taylor series approximation from, section 1.3.4, we need to keep its value very small compared to t. We may take $t = 0$ as the origin of time and choose $0 < \tau < 1$. That is, in Eq.(3.7), we can choose ε, u^* and b such that

$$\varepsilon b + \varepsilon^2 b^2 < 1 - u^{*2} + \varepsilon. \tag{3.25}$$

For $a = 0.7$, $\varepsilon = 0.8$ and $b = 0.4$ the unique equilibrium of system 3.1 is located at $u^* \approx -0.966, w^* = 0, v^* \approx -0.665$, see Fig.3.1. The critical value of relaxation constant for this case is

$$\tau_c \approx 0.363. \tag{3.26}$$

The corresponding estimate of the first Lyapunov coefficient at τ_c is

$$l_1(\delta_c) \approx -0.5023 < 0, \tag{3.27}$$

which predicts that the resulting oscillations ensuing from this Hopf bifurcation are stable (supercritical Hopf).

3.2.3 Numerical analysis

Hopf bifurcation and canard phenomenon

System (3.1) has equilibria which are independent of τ. This implies that the projection of the equilibrium curve onto the (u,τ)-plane is a straight line $u = u^*$ when we consider system (3.1), otherwise, the curve $X = 0$, if we consider system (3.3). However, the equilibrium may loose stability as τ is varied. Numerical simulation and continuation of system (3.1) and its subsequent bifurcations were performed on MATCONT [106]. Bifurcations of the mono-stable equilibrium was performed in two stages. First, we varied τ by keeping I at its rest value $I = 0$ and then we varied I, while keeping τ very close to zero. In the first study, a

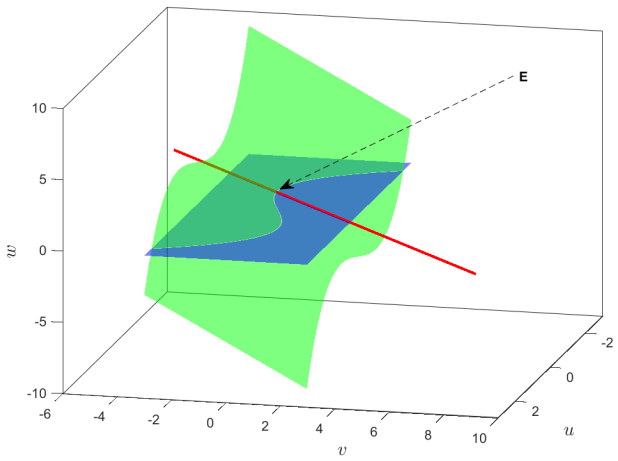

Figure 3.1 Intersecting nullclines of the system 3.1. The unique equilibrium (**E**) is located at the point of intersection of the green, blue planes, and the red line; representing the three nullclines of the system. Note that blue and red nullclines actually lie on the (u,v)-plane. System parameters were set as $a = 0.7$, $\varepsilon = 0.8$, $b = 0.4$ and $I = 0$.

supercritical Hopf (sH) bifurcation occurred at $\tau \approx 0.363$, which confirms results obtained from our previous analysis. Continuation of limit cycles born from this point is shown in Fig.3.2a. Here, sH represents a supercritical Hopf point beyond which, stable limit cycles emerge. System parameters used for this figure were $a = 0.7$, $b = 0.4$, $\varepsilon = 0.8$ and $I = 0$. Figure 3.2b shows the equilibrium curve in the presence of an external stimulating current I. Here, uH_1 and uH_2 are subcritical Hopf points with blue(stable) and red(unstable). These correspond to values $I_{c1} \approx 0.327$, and $I_{c2} \approx 1.423$ respectively. Unlike in the previous case, where τ was varied, these Hopf points are subcritical in nature. As I approaches uH_1 from the left, several stable and unstable cycles are born through a limit point of cycles bifurcation (LPC). The unstable cycles are generally contained within the stable cycle. As I is increased further, the unstable cycle coalesces with the fixed point in a subcritical Hopf bifurcation. This leaves an unstable fixed point and single stable limit cycle within the range $I_{c1} < I < I_{c2}$. This is confirmed by continuation of the cycles born from uH_1. The results are plotted in Fig.3.2c. Here, we observe a family of periodic orbits of slightly different geometry (rectangular) than those of sH. These cycles correspond to large amplitude limit cycles in contrast to those obtained from a supercritical Hopf bifurcation. In neurons, action potentials are primarily birthed via subcritical Hopf bifurcations. Even though the limit cycles born from a supercritical Hopf bifurcation do not lead to full-blown action potentials, they nonetheless play a crucial role in cell-cell communications especially when coupled via electrical synapses[142]. The location of the various LPC points, being very

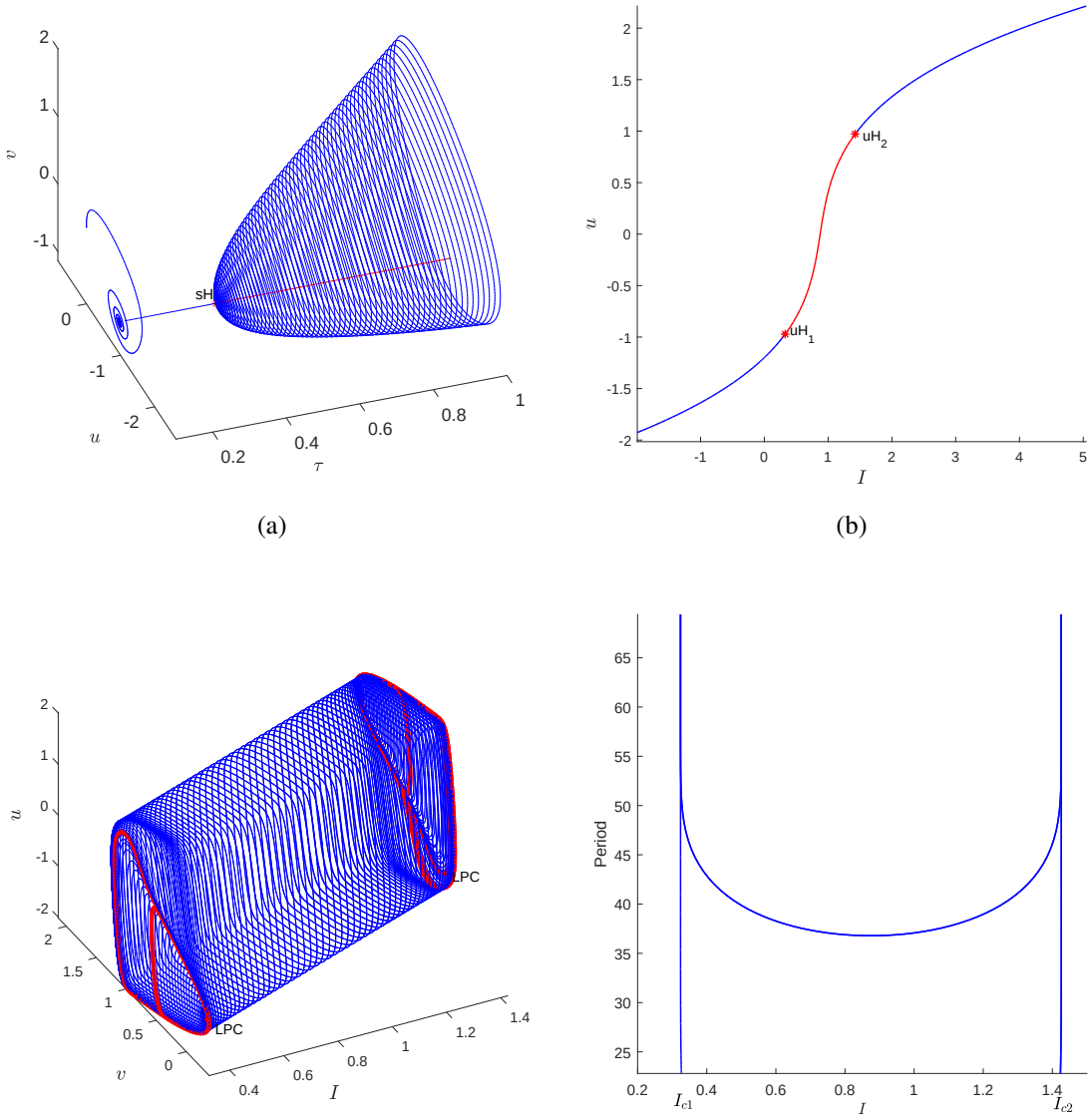

Figure 3.2 (a) Bifurcation of the equilibrium of system 3.1, in the absence of stimulating current. The straight line represents the equilibrium curve: stable(blue) and unstable(red).(b) Shows the equilibrium curve and its bifurcations in the presence of I. Limit cycles bifurcating from these points are shown in panel (c) as well as limit point of cycle points LPC. Panel (d) shows the variation of the period of these cycles with stimulating current I.

close to I_{c1} and I_{c2}, and their multiplicity suggests that a small region of bistability exists and canard explosion occurs at these locations, see cycles colored in red in Fig.3.2c. For Figs.3.2a,3.2b, and 3.2c, system parameters were $a = 0.7$, $b = 0.8$, $\varepsilon = 0.08$ and $\tau = 0.1$. The canard phenomenon is a distinct feature of the Van-der-Pol oscillator. For the analysis of canards in the FHN, see Ref. [47]. This suggests that the new model presented here, bears features reminiscent of other FHN models, as observed in Ref.[143], wherein a formula for calculating the location of these canards is given for a model in canonical form. The period of the ensuing limit cycles has been plotted against I and the results are displayed in Fig.3.2d. From the pattern depicted, we observe the occurrence of Homoclinic bifurcations near both critical values of current.

Codimension-two bifurcations

We have shown in the previous subsections that both τ and I can give rise to oscillations beyond certain critical values. We have not however, explored the combined effect of these two parameters, the analysis of which we have reserved for this subsection. The classical FHN model is known to exhibit two main codimension-two bifurcations, the Bogdanov-Takens (BT) and generalized Hopf (GH) bifurcations. For a full picture of the phase portraits around GH points, refer to Fig.1.8 from section 1.4.2. Figure 3.3 captures all relevant codimension two bifurcations of the system without diffusion, observed on the (I, τ)-parameter plane. Only the regions for which $\tau > 0$ are biologically meaningful. Completion of the green curve was limited by the continuation software. System parameters for continuation were $a = 0.7$, $b = 0.8$ and $\varepsilon = 0.08$. Four principal curves partition the parameter space into four distinct regions corresponding to topologically different features of the phase plane:

Regions A and B : The system is in a quiescent state with the origin as a stable focus. Figures. 3.4a and 3.4c show the corresponding phase portrait and time series obtained by numerical integration. In this region, it is possible however for very strong perturbations to excite the hyperbolic neuron.

Region C : In this region, the Jacobian of the system has a pair of purely complex conjugate eigenvalues, the stable origin loses its stability and a stable limit cycle is born in the process. Figures. 3.4b and 3.4d, show the corresponding numerical plots for the phase plane and time series. It is worth noting that the system can fire even when the excitation $I < 0$, provided τ is sufficiently large; a salient quality of resonators. Thus we can think of an increment in τ as resulting in the shrinking of the stable basin of attraction to a point and a corresponding increase in the unstable basin of attraction.

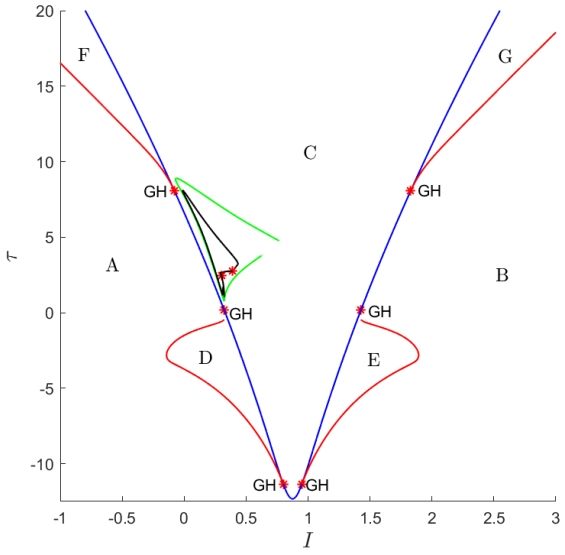

(a)

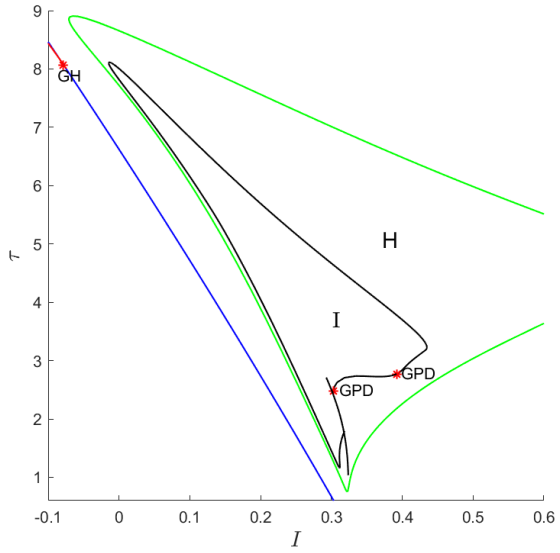

(b)

Figure 3.3 Codimension-two bifurcations of system 3.1, as seen on (I,τ)-parameter plane and phase space. (a) The blue curve represents the projection of the Hopf curve on the (I,τ)-plane, the red curve is a limit point of cycle curve (LPC), green and black curves are period doubling curves. (b) Magnification of a portion of the codimension-two plane. GH are Bautin bifurcation points while GPD are generalized period doubling points.

Regions D, E, F and G (Bistability) : In these regions, which are typically bounded by Hopf and LPC curves, the system is active (excitable) in a bi-stable sense. That is, a smaller unstable limit cycle is born inside the larger and stable cycle from region C. Points outside of the unstable cycle are attracted to the stable cycle but points within it are attracted to the origin, the origin regains its stability. Essentially this means the cell can either be in quiescent or firing mode depending on the degree of stimulation. As current is varied in the system, the unstable cycle grows and collides with the stable cycle, giving rise to LPC bifurcations. Further increases in current leads to the annihilation of both cycles and the system returns to a quiescent state . Fig.3.5 captures the bistable dynamics obtained numerically, for different initial conditions. The bistability observed in the neighborhood of this region can lead to two main types of bursting dynamics: Hopf-Hopf and SubHopf-fold bursting(see section 3.26 and Ref.[29]) as illustrated in Fig.3.6.

Regions H and I (Period-doubling): Within these regions, delimited by the period doubling curves, it is possible to find cycles of period-2 and -4 respectively. Since H, I $\subset$ C, the origin is unstable in this region and the emergent cycles are stable in nature. Period-2 cycles are born when a period-1 cycle undergoes a period doubling bifurcation. When the latter undergoes an additional period-doubling bifurcation, a period-4 cycle is born. Numerical simulations of the current model show that region I actually consists of period-3 and -4 cycles coexisting with chaotic attractors. Examples of period-2 and -3 and -4 orbits and their respective time series are shown in Figs.3.7. Fig.3.8 depicts the bifurcation diagrams across portions of these regions as τ is varied, supplemented with their respective maximum Lyapunov exponents. For the computation of the latter, a total of 13501 data points from the time series were used, under a time step of 0.0667. It can be seen that the aforementioned regions consist of marginally stable attracting sets interrupted by chaotic windows. An example of a chaotic set and its respective time series is shown in Figs.3.8e and 3.8f. While period-4 cycles can be explained in terms of successive period doubling bifurcations, period-3 cycles are often born out of tangent bifurcations similar to that of the logistic map demonstrated in [144, 145]. Indeed several tangent bifurcations (fold-flip) bifurcations were detected (Not shown) during the continuation of the period-doubling curve (green) and could explain the origin of the period-3 cycles.

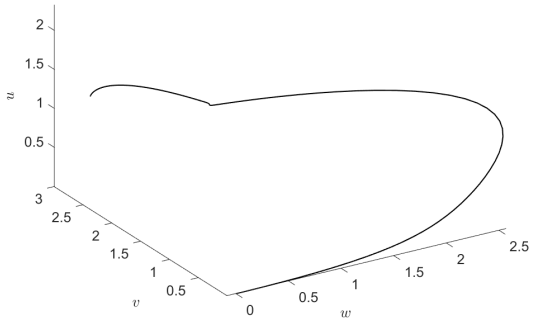

(a) $\tau = 0.1$ and $I = 2$

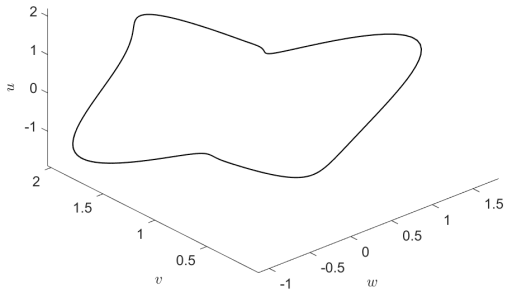

(b) $\tau = 0.2$ and $I = 1.3$

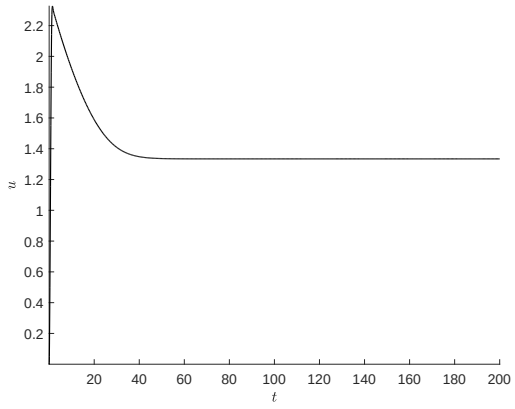

(c)

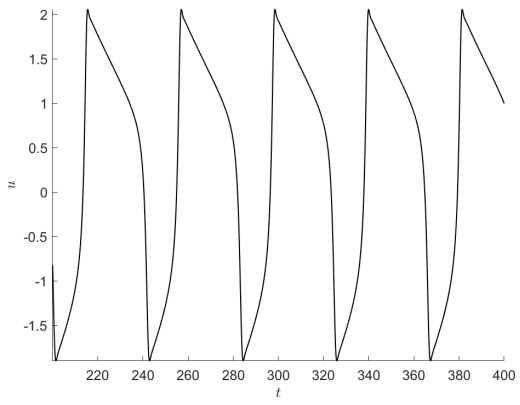

(d)

Figure 3.4 Phase plane portrait (top row) and corresponding time series (bottom row) in regions A, B(column 1) and C(column 2), of the (τ, I) parameter plane. System parameters were $a = 0.7$, $b = 0.8$ and $\varepsilon = 0.08$.

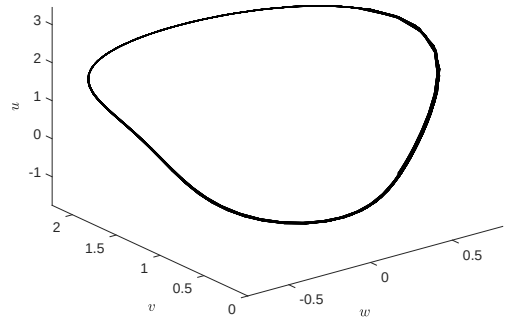

(a) $\tau = 16$, $I = 2.5$, and $(u, v, w) = (0, 0, 0)$

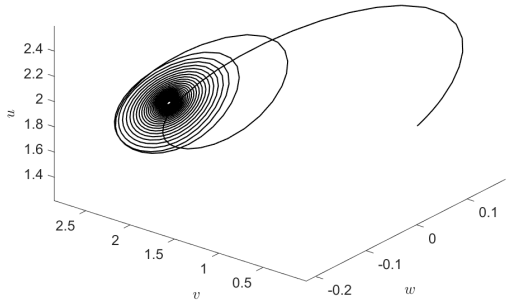

(b) $\tau = 16$, $I = 2.5$, and $(u, v, w) = (2, 0, 0)$

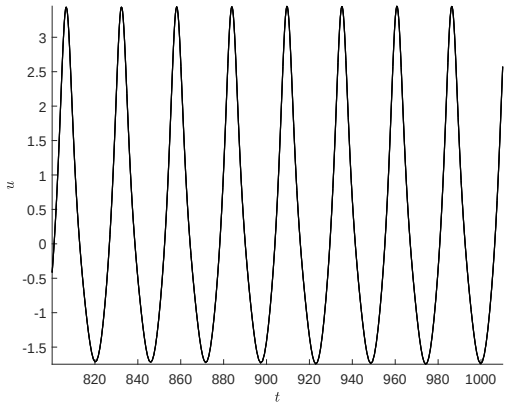

(c)

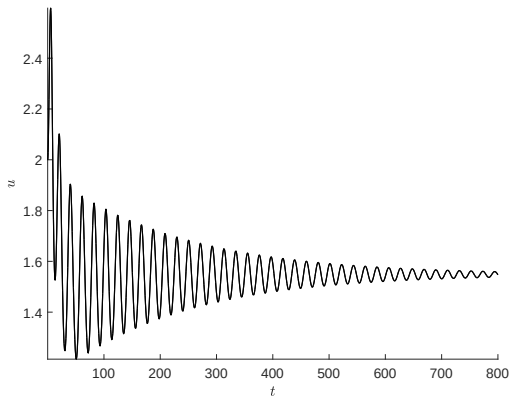

(d)

Figure 3.5 Phase plane portrait (top row) and corresponding time series (bottom row) in the bistable regions D, E, F and G, using different initial conditions. System parameters were $a = 0.7$, $b = 0.8$ and $\varepsilon = 0.08$.

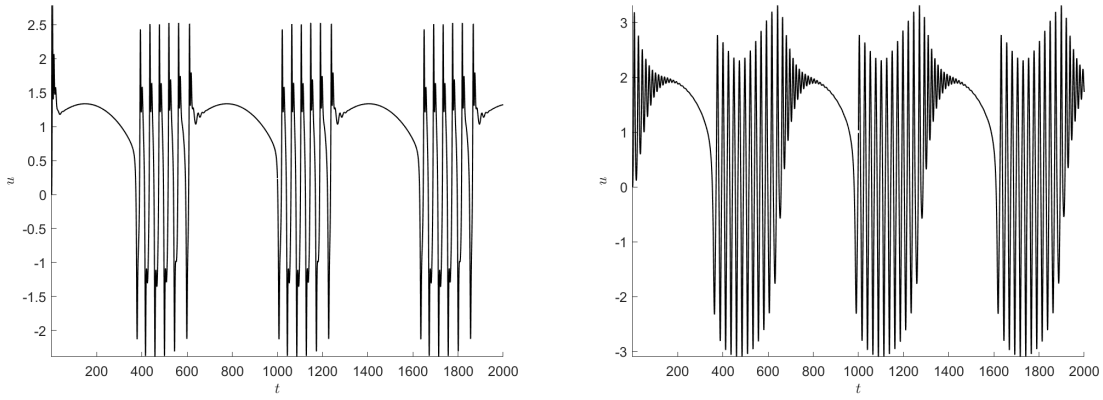

(a) $\tau = 2.5$, $I = 0.5 + \sin 0.01t$ (b) $\tau = 12$, $I = 2 + 1.8\sin 0.01t$

Figure 3.6 Bursting dynamics of neuron showing: (a) Hopf-Hopf bursting, and (b) SubHopf-fold bursting, observed in the neighborhood of the bistable regions for periodic external stimuli. System parameters were $a = 0.7$, $b = 0.8$ and $\varepsilon = 0.08$.

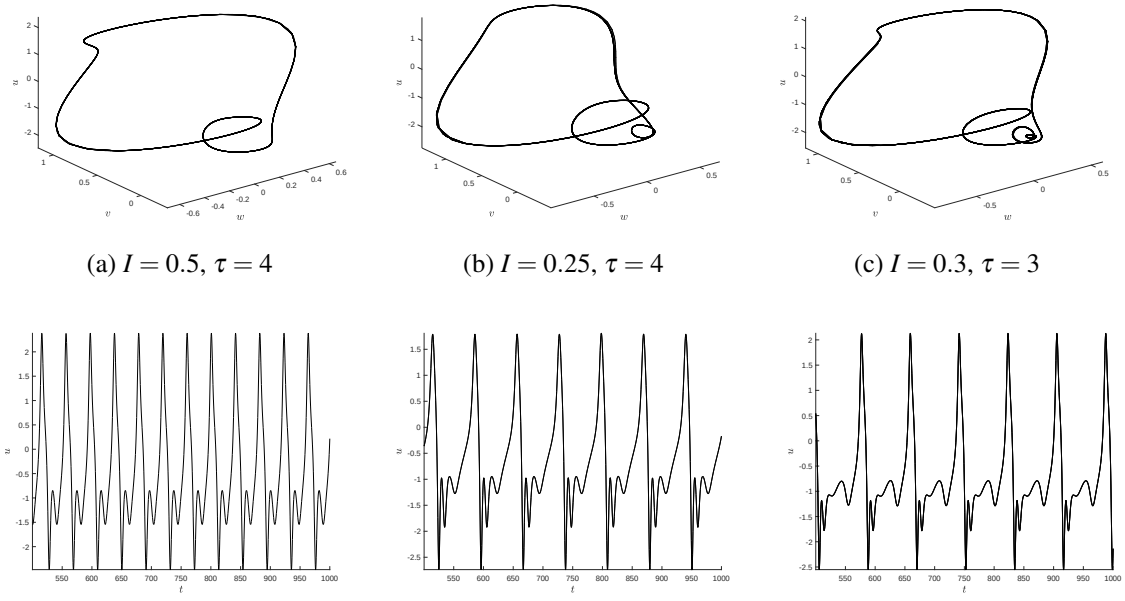

(a) $I = 0.5$, $\tau = 4$ (b) $I = 0.25$, $\tau = 4$ (c) $I = 0.3$, $\tau = 3$

(d) $I = 0.5$, $\tau = 4$ (e) $I = 0.25$, $\tau = 4$ (f) $I = 0.3$, $\tau = 3$

Figure 3.7 Phase plane (row 1) and corresponding time series (row 2) in period doubling regions I and H showing: (a) a period-two orbit in H, (b) period-three, and (c) period-four orbit in I with their respective time series in panels (d), (e) and (f). System parameters were $a = 0.7$, $b = 0.8$ and $\varepsilon = 0.08$.

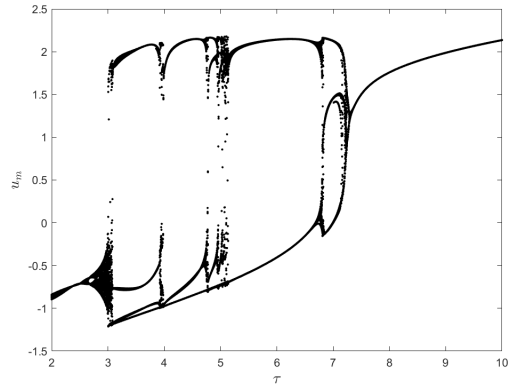

(a) $I = 0.25$

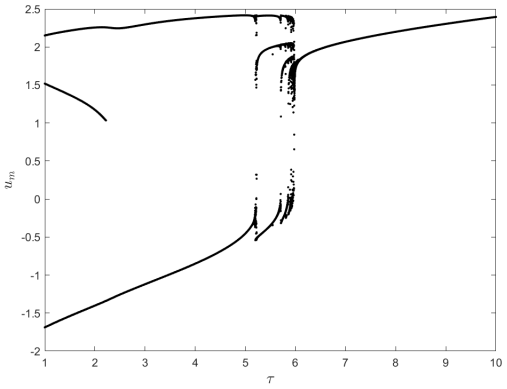

(b) $I = 0.5$

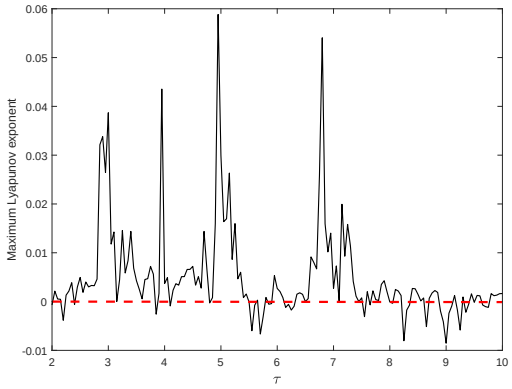

(c) $I = 0.25$

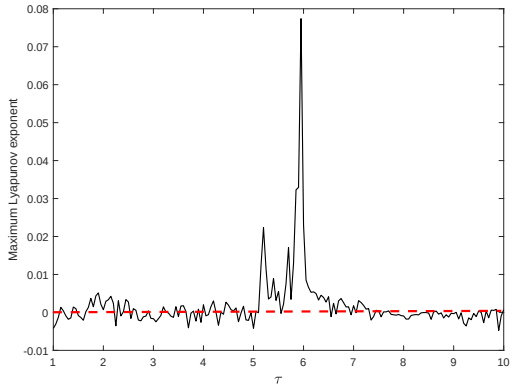

(d) $I = 0.5$

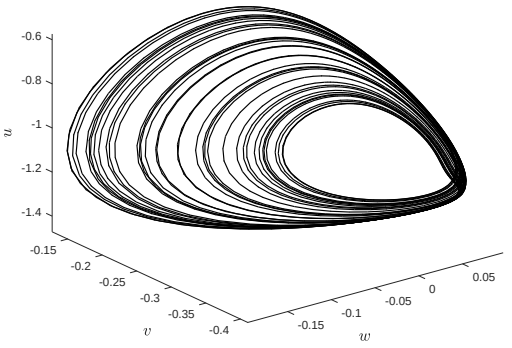

(e) $I = 0.3$, $\tau = 1.5$

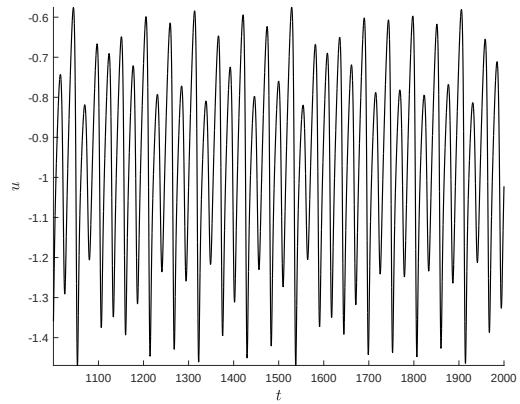

(f) $I = 0.3$, $\tau = 1.5$

Figure 3.8 Bifurcation of local extrema of membrane potential u_m (row 1) with τ and corresponding variation of maximum Lyapunov exponent (row 2). Red dashed line marks the transition from stable to chaotic behavior. (e) Example of chaotic attractor in region I and (f) its corresponding time series. System parameters were $a = 0.7$, $b = 0.8$ and $\varepsilon = 0.08$.

3.2.4 Discussions

It should be noted that, while delays in reality can be very large such as observed in Fig.3.3, the Taylor series approximation used section 1.3.4 to obtain the hyperbolic diffusion allows us to study make accurate predictions on the actual neuronal dynamics only within small values of τ, typically less than 1. That is, as τ gets larger, the dynamic behavior observed in Fig.3.3, might not accurately describe that of the parabolic model with delay which it tries to model. This is because, larger values of τ will impose higher order derivatives in Eq.(1.24), and Eq.(1.26), which might lead to qualitatively different dynamics from that of the original system with delay. However if these higher order derivatives or their coefficients are very small or zero then higher values of τ might be justified. A full discussion of approximations of delay systems with Taylor series is given in Ref.[146]. Nonetheless, the dynamics captured by Fig.3.3 especially in the higher τ regions is interesting.

Since the Hopf bifurcation induced by τ on system (2.2) is supercritical, it seems reasonable to think that the oscillations it induces would be relevant under subthreshold operating conditions of the neuron. Subthreshold oscillations play a role brain processes such as action potential timing control[147]— by increasing the firing probability of neurons[19], synaptic plasticity [148] and much more. Furthermore, If one is interested in studying the temporal resolution of neurons, one should consider delays in the analysis since certain neurons can discriminate between signals based on the delay of the system. For example, dendritic and axonal delays lead to spike-timing dependent plasticity (STDP)[149].

3.3 Linear stability analysis and Hopf bifurcation with diffusion

3.3.1 Linear stability analysis, Hopf and pitchfork bifurcations for $k \neq 0$

We now consider the following Sturm-Liouville problem (Eq.(2.20)) for system (2.3):

$$\begin{aligned} \mathscr{L}U &= \lambda U, \\ U_x\big|_{x=0} &= U_x\big|_{x=\pi} = 0. \end{aligned} \tag{3.28}$$

Solutions to this equation have the form $U = \sum_k W_k \phi_k e^{\lambda t}$, $k \in \mathbb{N}$, where $\phi_k = \cos kx$ and $W_k \in \mathbb{C}^3$, is an eigenvector of $\mathscr{L}_k = A - k^2 D$ corresponding to the eigenvalue λ. For the Hopf and Pitchfork (stationary) bifurcations: $\lambda = \pm i\omega$, and $\lambda = 0$ respectively. The dot product

of two eigenfunctions is defined as:

$$\langle \psi, \phi \rangle = \langle \psi, \phi \rangle_{L^2}. \tag{3.29}$$

The corresponding eigenvalue problem is then as follows:

$$\chi(\lambda) = \lambda^3 + T\lambda^2 + M\lambda + R = 0, \tag{3.30}$$

with,

$$T = (\varepsilon b + \delta), \tag{3.31}$$

$$M = (\frac{\ell^2 \Lambda + d\pi^2 k^2}{\ell^2})\delta, \tag{3.32}$$

$$R = (\frac{\ell^2(bu^{*2} - b + 1) + d\pi^2 k^2 b}{\ell^2})\varepsilon\delta, \tag{3.33}$$

with $\Lambda = \varepsilon b + u^{*2} + 1$.

Theorem 4 (Hopf bifurcation)**.** *The polynomial $\chi(\lambda)$ in Eq.*(3.30) *has a pair of purely imaginary eigenvalues, and system (2.2) undergoes a Hopf bifurcation if*

$$TM - R = 0. \tag{3.34}$$

Moreover, the third eigenvalue lies in the left half of the complex plane(LHCP) if $R > 0$ and $T > 0$.

Proof. According to Vieta's formulas, the roots of polynomial $\chi(\lambda)$, β_1, β_2 and β_3, are related to its coefficients T, M and R by

$$\begin{aligned} \beta_1 + \beta_2 + \beta_3 &= -T, \\ \beta_1\beta_2 + \beta_1\beta_3 + \beta_2\beta_3 &= M, \\ \beta_1\beta_2\beta_3 &= -R. \end{aligned} \tag{3.35}$$

it follows that,

$$TM - R = \beta_1^2(\beta_2 + \beta_3) + \beta_2^2(\beta_1 + \beta_3) + \beta_3^2(\beta_1 + \beta_2) + 2\beta_1\beta_2\beta_3 \tag{3.36}$$

$$= (\beta_1 + \beta_2)(\beta_1 + \beta_3)(\beta_2 + \beta_3). \tag{3.37}$$

Assume the system is at a Hopf bifurcation, then $\exists\ \beta_i, \beta_j,\ i \neq j,\ \ni \mathrm{Re}(\beta_i) = \mathrm{Re}(\beta_j) = 0$ and $\mathrm{Im}(\beta_i) = -\mathrm{Im}(\beta_j)$ which implies that

$$\beta_i + \beta_j = 0. \tag{3.38}$$

That is, one of the factors in the product $(\beta_1+\beta_2)(\beta_1+\beta_3)(\beta_2+\beta_3)$ is zero, whence $TM - R = 0$, which concludes the first part of the proof.
To prove that the third eigenvalue is negative at the Hopf bifurcation, we assume the statements $R > 0$ and $T > 0$ are true, then we can write $R = |R|$ and $T = |T|$. This implies $\exists\ \beta_l$, $l \neq i, j$ such that the first and third equations of system (3.35) become

$$\beta_l = -|T|, \tag{3.39}$$

$$\text{and } \beta_l|\beta_j|^2 = -|R|. \tag{3.40}$$

From these two equations, we conclude that $\beta_l < 0$, such that the third eigenvalue lies in the LHCP, and concludes the proof. □

Remark 6. *It can be shown that the roots of $\chi(\lambda)$ given by Eq.*(3.30) *all lie in the left half of the complex plane, that is, the steady state is asymptotically stable if $T > 0$, $R > 0$ and $TM > R$ and unstable if $T < 0$, $R < 0$ and $TM < R$. Elements required to construct this proof can be found in Ref.[150]. The condition for stationary bifurcations is given by the condition $R = 0$. This condition is independent of τ and is a function of length and diffusion.*

Theorem 5 (Pitchfork bifurcation)**.** *System (2.2) has a Pitchfork (stationary) bifurcation, independent of τ, when $R = 0$. This implies the diffusion and length of the system satisfy:*

$$\ell = \sqrt{\frac{-d\pi^2 k^2 b}{bu^{*2} - b + 1}},\ \textit{and} \quad d < 0. \tag{3.41}$$

A negative diffusion coefficient is admissible if a biological process, an external force, or a diffusing species causes another species (in this case the membrane potential) to diffuse against its concentration gradient. This can happen under two scenarios: In the first, and very rare case, the uphill flux is induced by a species's gradient. In the second and more common case, negative diffusion is driven by the gradient of another species. The former case is referred to as incongruent diffusion [151] and the latter case as uphill diffusion[152]. Diffusion of substances against their concentration gradients has been extensively studied in multicomponent chemical systems [153], where they seem to be more prevalent. Although we did not find strong evidence of such a phenomenon in the neuroscience literature, we do

not rule out the possibility of such an observation being made in future experimental studies. Thus at the moment, Theorem 5, can be regarded as pure mathematical speculation.
For the Hopf and Pitchfork bifurcations, the respective solutions to the linear system, Eq.(3.28), also referred to as the order-one or most unstable mode at instability, take the form:

$$U_{Hopf} = W_0 e^{i\omega t} + W_0 e^{-i\omega t}, \tag{3.42}$$

$$U_{Pitchfork} = W_k \phi_k + W_{-k}\bar{\phi}_k,\ k \neq 0. \tag{3.43}$$

In what follows, we shall focus on the Hopf bifurcation, derive the respective amplitude equations and study the dynamics of the restricted system. The Pitchfork bifurcation is to be addressed numerically.
From Theorem 4, we conclude that at $TM = R$, system (2.2) exhibits a Hopf bifurcation and $\chi(\lambda)$ has a pair of purely imaginary roots $\lambda_c = \pm i\omega_k$ where

$$\omega_k^2 = (\frac{\ell^2\Lambda + d\pi^2k^2}{\ell^2})\delta, \tag{3.44}$$

and the critical value of τ for which this occurs is given by the reciprocal of

$$\delta_c(k) = \frac{\ell^2(\varepsilon - \varepsilon^2 b^2)}{\ell^2\Lambda + d\pi^2k^2}, \tag{3.45}$$

which, gives us

$$\tau_c(k) = \tau_0 + \frac{d\pi^2k^2}{(\varepsilon - \varepsilon^2 b^2)\ell^2}, \tag{3.46}$$

where $\tau_0 = \frac{\Lambda}{\varepsilon - \varepsilon^2 b^2}$ is the critical parameter value for the homogeneous case ($k = 0$). Fig.3.9 shows the variation of τ against the wavenumber (k).

Eq.(3.44) gives us the dispersion relation of the system from which we can obtain the critical phase velocity

$$v_{ph} = \sqrt{\frac{1}{\tau k_c^2} + \frac{d\pi^2}{\ell^2\tau}}. \tag{3.47}$$

This velocity represents the phase velocity of the traveling waves at the onset of the Hopf instability. Fig.3.10 and Fig.3.11 show the stability boundary for propagating traveling waves in the (τ, v_{ph}) and (k, v_{ph}) planes respectively. Two main observations can be made from these figures: as $\tau \to 0$, the critical propagation velocity tends to infinity, and for any given τ there exist a critical velocity beyond which, an oscillatory instability sets-in. The first observation can be understood in the sense that for $\tau \approx 0$, the current model behaves like the

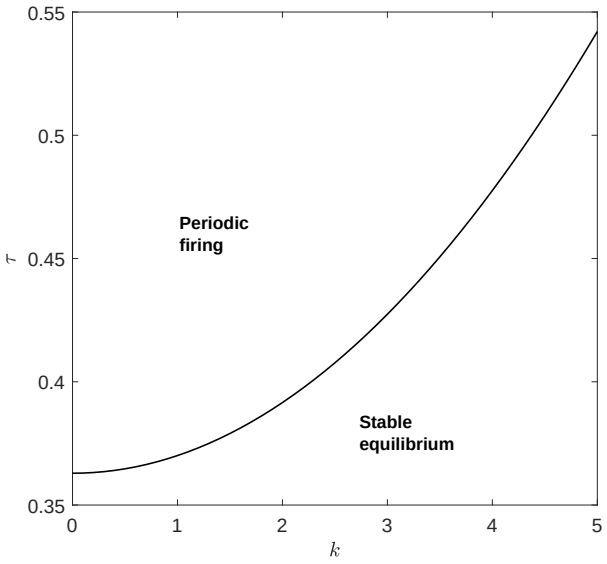

Figure 3.9 Critical curve for a continuous k, showing the Hopf bifurcation curve for system 2.3, in the (k,τ)-plane. System parameters were $a = 0.7$, $b = 0.4$, $e = 0.8$, $d = 0.005$, $u^* = -0.966$.

classical FHN which assumes an infinite velocity of propagation. However, for relatively large delays, the critical velocity is finite and diminishes with increasing τ. Similar results were obtained with models of intracortical neural fields of integrodifferential-type [57]. Also note that, in the limit $k \to \infty$, the wave system behaves like a non-dispersive system since v_{ph} is independent of k.

Let $\alpha = \delta_c(k) - \delta_c(0)$ represent the distance to the Hopf bifurcation point. In the limit $\alpha \to 0$, $d \to 0$ (or $\ell \to \infty$), all modes with $k > 0$ become simultaneously excited with approximately the same frequency

$$\omega_0^2 = \varepsilon - \varepsilon^2 b^2, \tag{3.48}$$

corresponding to the spatially homogeneous oscillation frequency. These modes ($k > 0$, but not too large), constitute the side-band and can be viewed as perturbations of the homogeneous mode. Each mode's frequency in the band is shifted from the homogeneous frequency as

$$\omega_k^2 - \omega_0^2 = \frac{d\pi^2 k^2}{\ell^2}\delta_c(k). \tag{3.49}$$

Thus, in the limit under consideration, other spatially periodic wave states (traveling waves) in the neighborhood of the spatially homogeneous one, propagate. These wave states are discrete and countable in k, for a finite size domain and form a continuous band for an infinite domain. Furthermore, they may induce long-wave instabilities, see Ref.[85]. The dynamics

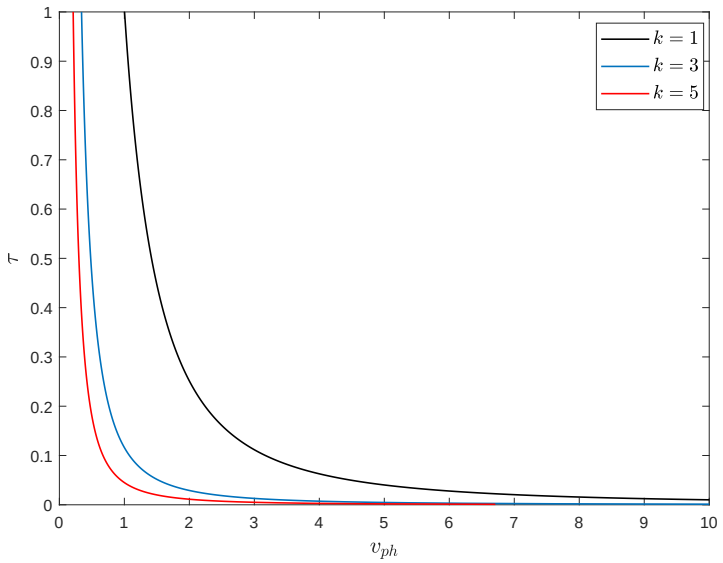

Figure 3.10 Stability boundaries of traveling waves of system 2.3 as seen on the (τ, v_{ph})-plane, v_{ph} being the phase velocity. The curve is plotted for different values of k shown in the legend. Other parameters were $\ell = \pi$ and $d = 0.01$.

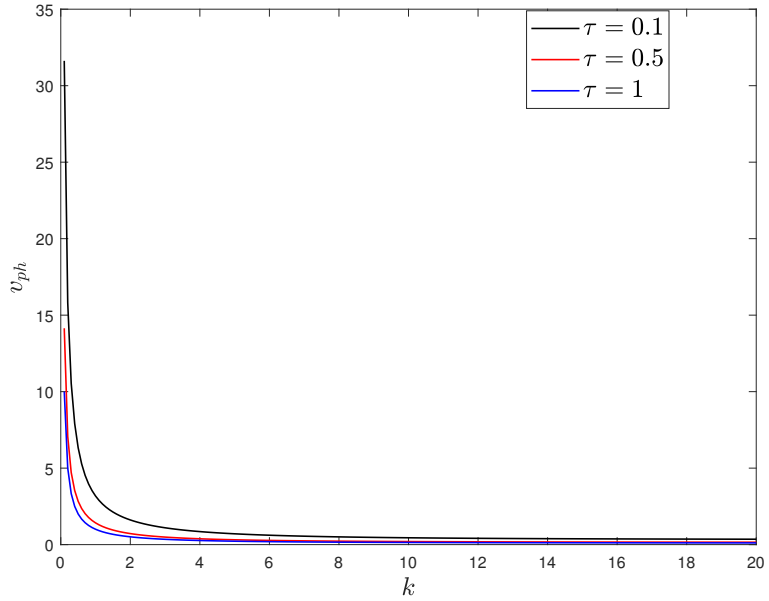

Figure 3.11 Stability boundaries of traveling waves of system 2.3 as seen on the (k, v_{ph})-plane. The curve is plotted for different values of τ shown in the legend. Other parameters were $\ell = \pi$ and $d = 0.01$.

of the slowly varying amplitudes of these wave states, in the neighborhood of the Hopf bifurcation, in the long-time, weakly-coupled limit or large spatial domain, can be modeled by the corresponding CGL ((2.82)), from which the stability of the different Fourier modes can be studied.

3.3.2 Direction of Hopf bifurcation for $k = 1$

In this section we compute the direction of the Hopf bifurcation for a specific wave mode ($k \in \mathbb{N}$) by evaluating the corresponding Lyapunov coefficient. We use the projection method with diffusion (see section 2.3.1). For a similar application of the projection method to the FHN in infinite-dimensional setting consult Ref.[154], and Ref.[155] for its application to different reaction diffusion models. Since Ω is finite, Eq.(3.46) implies there is an increasing sequence of values δ_k, for Eq.(2.2) has a pair of purely imaginary eigenvalues.

Theorem 6. *At $\delta = \delta_c$ and for mode $k = 1$, Eq.(2.2) has a two-dimensional parameter dependent center manifold $W^c_\delta \in \mathscr{X}$ of the form,*

$$y = \frac{r_{20}}{2}z^2 + r_{11}z\bar{z} + \frac{r_{02}}{2}\bar{z}^2 + \mathscr{O}(|z|^3). \tag{3.50}$$

Where $r_{ij} = \sum_{m=1}^{2} \gamma_m e^{\beta_m x}\nu + \sum_{l=0}^{2} B_l \cos lx$, with, $m \in \mathbb{N}$, γ_m, $\beta_m \in \mathbb{C}^1$, and $\nu, B_l \in \mathbb{C}^3$. Moreover, the respective first Lyapunov coefficient at the point of bifurcation is given by

$$l_1(\delta) = \frac{1}{\omega}\mathrm{Re}\Big[-\frac{3\delta}{8}\bar{W}_2 V_1^2 \bar{V}_1 - 2u^*\delta\bar{W}_2\int_{\hat{\Omega}} f(x)\cos^2 x dx\Big], \tag{3.51}$$

where $f(x) = (V_1 r_{11,1} + \bar{V}_1 r_{20,1})$.

Proof. The existence of a center manifold in an infinite-dimensional reaction diffusion system can be established following principles established in Refs.[156, 14] and examples of applications in Ref.[15].

Suppose a hopf bifurcation occurs for some k, say k_0, with all other wave modes being stable. Then we can define an eigenfunction $q = V\cos k_0 x$ of $\mathscr{L}(\delta_c)$, $V \in \mathbb{C}^3$, and an adjoint eigenfunction $p = W\cos k_0 x$, $W \in \mathbb{C}^3$, of $\mathscr{L}^*(\delta_c) = -k_0^2 D^T(\delta_c) + A^T(\delta_c)$. That is,

$$\mathscr{L}(\delta_c) = \begin{pmatrix} 0 & 1 & 0 \\ \Theta & -\delta & -\delta_c \\ \varepsilon & 0 & -\varepsilon b \end{pmatrix}, \text{and} \quad \mathscr{L}^*(\delta_c) = \begin{pmatrix} 0 & \Theta & \varepsilon \\ 1 & -\delta_c & 0 \\ 0 & -\delta_c & -\varepsilon b \end{pmatrix}, \tag{3.52}$$

where $\Theta = \delta_c(1 - u^{*2} - dk_0^2)$, such that

$$\mathscr{L}(\delta_c)q = i\omega q, \qquad \mathscr{L}^*(\delta_c)p = -i\omega p, \quad \text{and} \quad \langle p, q\rangle = 1. \tag{3.53}$$

The normalization condition implies $\langle W, V\rangle \int_{\hat{\Omega}} \cos^2 k_0 x \, dx = 1$, from which it follows that

$$\langle W, V\rangle = \frac{2}{\pi}. \tag{3.54}$$

For the remaining part of the proof, we consider the mode $k_0 = 1$. Also, we shall represent δ_c simply as δ, $\mathscr{L}(\delta_c)$ as $\mathscr{L}$, $D(\delta_c)$ as D, and $A(\delta_c)$ as A.

We wish to find the equation of the nonlinear center manifold for $k = 1$ as well as the restricted dynamics to it. The spectral decomposition of the linear space at the critical point becomes

$$U = zq + \bar{z}\bar{q} + y, \tag{3.55}$$

and the reduction function as

$$y = \frac{r_{20}}{2}z^2 + r_{11}z\bar{z} + \frac{r_{02}}{2}\bar{z}^2 + \mathscr{O}(|z|^3). \tag{3.56}$$

Using the Taylor series decomposition of $F(zq + \bar{z}\bar{q} + y, \delta)$, we determine the expressions Eq.(2.69) and Eq.(2.70) as

$$H_{i,j} = \Psi_{ij}\cos x - S_{ij}\cos^2 x, \tag{3.57}$$

$$\Psi_{ij} = 2(\alpha_{ij}\bar{W}_2 V + \alpha_{ji}W_2\bar{V})\int_{\hat{\Omega}} \cos^3 x dx, \quad \alpha_{ij} = V_1^i \bar{V}_1^j u^* \delta, \tag{3.58}$$

$$S_{i,j} = \begin{pmatrix} 0 \\ 2\alpha_{ij} \\ 0 \end{pmatrix}, \quad G_{i+j=2} = -2\alpha_{ij}\bar{W}_2 \int_{\hat{\Omega}} \cos^3 x dx, \tag{3.59}$$

and

$$G_{21} = -2\delta\bar{W}_2 V_1^2 \bar{V}_1 \int_{\hat{\Omega}} \cos^4 x dx. \tag{3.60}$$

Using these expressions, we solve the system of equations : Eqs.(2.65-2.67). We describe the procedure for Eq.(2.65); solutions to Eq.(2.66) and Eq.(2.67) are derived in a similar manner. Consider the homogeneous problem:

$$(D\frac{d^2}{dx^2} + A - 2i\omega E)r_{20} = 0, \tag{3.61}$$

with the corresponding boundary conditions given by Eq.(2.68). We assume solutions of the form:

$$r_{20}^{h} = \boldsymbol{a}e^{\eta x}, \tag{3.62}$$

where $\boldsymbol{a} \in \mathbb{C}^3$. Substituting Eq.(3.62) into Eq.(3.61), we obtain

$$(\eta^2 D - K)\boldsymbol{a} = 0, \tag{3.63}$$

where $K = 2i\omega E - A$. For a nontrivial solution, Eq.(3.63) represents a generalized eigenvalue problem, with eigenvalue η_i corresponding to an eigenvector $\boldsymbol{a}$. The two eigenvalues are solutions to the quadratic matrix equation

$$det(\eta^2 D - K) = 0. \tag{3.64}$$

It follows that,

$$\delta d(2i\omega + \varepsilon b)\eta^2 + \delta(2i\omega + \varepsilon b)(1 - u^{*2}) - 2i\omega(2i\omega + \varepsilon b)(2i\omega + \delta) - \delta\varepsilon = 0. \tag{3.65}$$

Once the two eigenvalues η_1 and η_2 have been obtained from Eq.(3.65), the homogeneous solution can be written as

$$r_{20}^{(h)} = (C_1 e^{\eta_1 x} + C_2 e^{\eta_2 x})\boldsymbol{a}. \tag{3.66}$$

Using similar arguments, it is possible to construct the homogeneous solutions $r_{11}^{(h)}$ and $r_{02}^{(h)}$. Next, we obtain the particular solution to Eq.(2.65). In this case, the functions $H_{i,j}$ can be regarded as periodic forcing agents on the unperturbed system as such they can be decomposed into a Fourier (trigonometric) series. That is,

$$H_{i,j} = \Psi_{ij}\cos x - \frac{1}{2}S_{ij}(1 + cos2x). \tag{3.67}$$

For Eq.(2.65), we can thus choose a particular solution of the form

$$r_{20}^{(p)} = B_n \cos nx, \tag{3.68}$$

with $n \in \mathbb{N}$. Substituting this trial solution into Eq.(3.61) and comparing like terms, we obtain

$$B_0 = \frac{1}{2}(A - 2i\omega E)^{-1} S_{20}, \tag{3.69}$$

$$B_1 = -(-D + A - 2i\omega E)^{-1}\Psi_{20}, \tag{3.70}$$

$$\text{and } B_2 = \frac{1}{2}(-4D + A - 2i\omega E)^{-1} S_{20}, \tag{3.71}$$

such that,

$$r_{20}^{(p)} = B_0 + B_1 \cos x + B_2 \cos 2x. \tag{3.72}$$

Performing similar operations on the Eqs.(2.66) and (2.67), we obtain

$$r_{11}^{(p)} = \frac{1}{2}A^{-1}S_{11} - (-D+A)^{-1}\Psi_{11}\cos x + \frac{1}{2}(-4D+A)^{-1}S_{11}\cos 2x, \tag{3.73}$$

$$r_{02}^{(p)} = \frac{1}{2}(A+2i\omega E)^{-1}S_{02} - (-D+A+2i\omega E)^{-1}\Psi_{02}\cos x + \frac{1}{2}(-4D+A+2i\omega E)^{-1}S_{02}\cos 2x. \tag{3.74}$$

The general solution to Eqs.(2.65-2.67) then becomes

$$r_{ij} = r_{ij}^{(h)} + r_{ij}^{(p)}, \tag{3.75}$$

which is of the form $r_{ij} = \sum_{m=1}^{2} \gamma_m e^{\beta_m x}\nu + \sum_{l=0}^{2} B_l \cos lx$.
Subsequent application of the boundary conditions imposed on the vectors r_{ij}, determines the constants C_1 and C_2 of Eq.(3.66). We have

$$C_2 = e^{(\eta_1-\eta_2)\pi}, \text{ and} \qquad C_1 = -\frac{\eta_2}{\eta_1}C_2. \tag{3.76}$$

Hence, the center manifold is uniquely determined. Substituting Eq.(3.75) into Eq.(3.56), gives the dynamics on the nonlinear center manifold:

$$\dot{z} = i\omega_0 z + \frac{1}{2}G_{20}z^2 + G_{11}z\bar{z} + \frac{1}{2}G_{02}\bar{z}^2 + \frac{1}{2}G_{21}z^2\bar{z} + \langle G_{10}, y\rangle z + \langle G_{01}, y\rangle \bar{z} + \ldots, \tag{3.77}$$

with

$$\bar{G}_{10,i} = \frac{\partial^2}{\partial y_i \partial z}\langle p, F(zq+\bar{z}\bar{q}+y)\rangle\big|_{z=0,y=0}, \qquad i = 1,2,3. \tag{3.78}$$

$$\bar{G}_{10} = (-2u^*\delta\bar{W}_2 V_1 \int_{\hat{\Omega}} \cos^2 x dx, 0, 0), \tag{3.79}$$

$$\bar{G}_{01,i} = \frac{\partial^2}{\partial y_i \partial \bar{z}}\langle p, F(zq+\bar{z}\bar{q}+y)\rangle\big|_{z=0,y=0}, \tag{3.80}$$

$$\text{and } \bar{G}_{01} = (-2u^*\delta\bar{W}_2\bar{V}_1 \int_{\hat{\Omega}} \cos^2 x dx, 0, 0). \tag{3.81}$$

It follows that,

$$\dot{z} = i\omega z + \frac{1}{2}G_{20}z^2 + G_{11}z\bar{z} + \frac{1}{2}G_{02}\bar{z}^2 + \left(\frac{1}{2}G_{21} - 2u^*\delta\bar{W}_2(V_1 r_{11,1} + \bar{V}_1 r_{20,1})\int_{\hat{\Omega}}\cos^2 x dx\right)z^2\bar{z}\ldots, \tag{3.82}$$

where, $r_{ij,m}$ represents the m^{th} component of r_{ij}. Since $G_{20} = G_{11} = G_{02} = 0$ by integration, the first Lyapunov coefficient is expressed as

$$\begin{aligned} l_1(\delta) &= \frac{1}{\omega}\mathrm{Re}\Big[\frac{1}{2}G_{21} - 2u^*\delta\bar{W}_2\int_{\hat{\Omega}} f(x)\cos^2 x dx\Big] \\ &= \frac{1}{\omega}\mathrm{Re}\Big[-\frac{3\delta}{8}\bar{W}_2 V_1^2\bar{V}_1 - 2u^*\delta\bar{W}_2\int_{\hat{\Omega}} f(x)\cos^2 x dx\Big], \end{aligned} \tag{3.83}$$

where $f(x) = (V_1 r_{11,1} + \bar{V}_1 r_{20,1})$. □

Theorem 7. *The Hopf bifurcation of any mode k_0 from rest is supercritical if $l_1(\delta) < 0$ and subcritical if $l_1(\delta) > 0$.*

3.3.3 Numerical analysis

Spatio-temporal dissipative structures

In this subsection we simulate Eq.(2.2) together with the no-flux boundary conditions using the method of lines. We consider a neuron of length $\ell = \pi$, discretized over 100 points. Setting $\varepsilon = 0.8$, $b = 0.4$, $a = 0.7$, $\ell = \pi$ and $d = 0.005$, we can estimate the sequence of values τ_k for which system (2.2) exhibits a Hopf bifurcation. This is obtained from Eq.(3.46), evaluated at different k values. For $0 \leq k \leq 3$, the corresponding sequence τ_k is

$$\tau_0 = 0.3629, \tau_1 = 0.3701, \tau_2 = 0.3916, \tau_3 = 0.4274. \tag{3.84}$$

The first unstable mode leading to spatial-temporal dissipative structures occurs at $k = 0$. This mode, corresponds to the spatially homogeneous case or bulk oscillations for which, all spatial points fire synchronously. Note that for this set of parameters, we do not expect a Pitchfork instability. In each case, if $\tau < \tau_0$ all modes converge to a uniform stationary solution while some get excited if $\tau \geq \tau_0$. Fig.3.12 depicts the temporal evolution of u at $x = 0$, for different initial conditions, below and above criticality. Noise for the simulations was added using the MATLAB function : $rand(size(n))$. Here, initial values were $w = w^* = 0$, $v = v^* = -0.665$ while other system parameters were $\ell = \pi$, $a = 0.7$, $d = 0.5$, $b = 0.4$, and $\varepsilon = 0.8$. Damped wave profiles propagate below criticality as shown in Fig.3.13. Here, system initial values were $w = w^* = 0$ and $v = v^* = -0.665$ while other parameters were

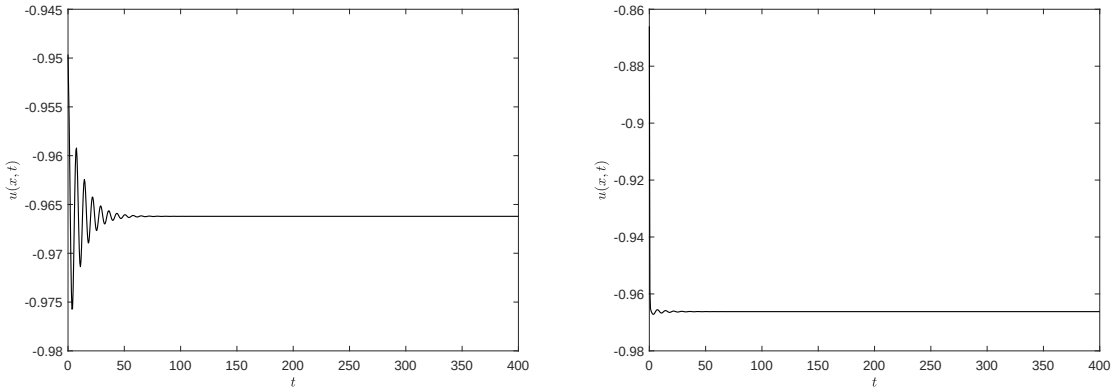

(a)

(b)

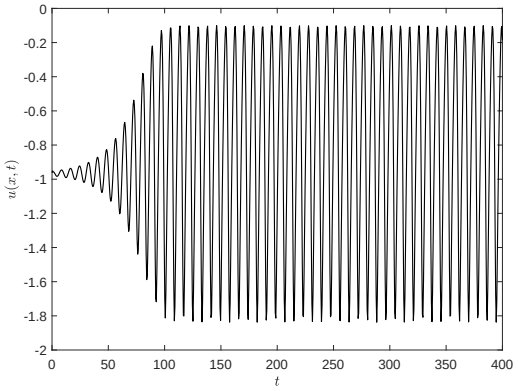

(c)

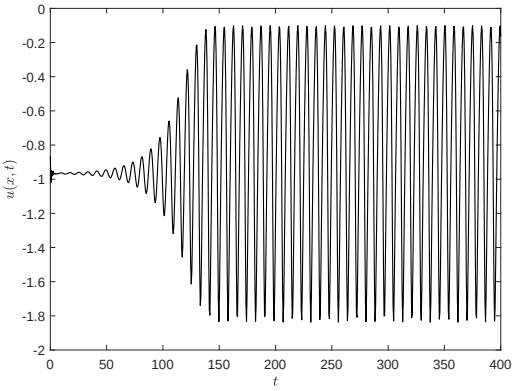

(d)

Figure 3.12 Temporal evolution of solution of membrane potential of system (2.2) at $x = 0$. $\tau < \tau_0$ in panels (a) and (b) while $\tau > \tau_0$ as in panels (c) and (d). Initial conditions were taken as $u(x,0) = u^* + 0.03 \times \textit{noise}$ for (a) and (c), and as $u(x,0) = u^* + 0.1\cos 1x$ for (b) and (d).

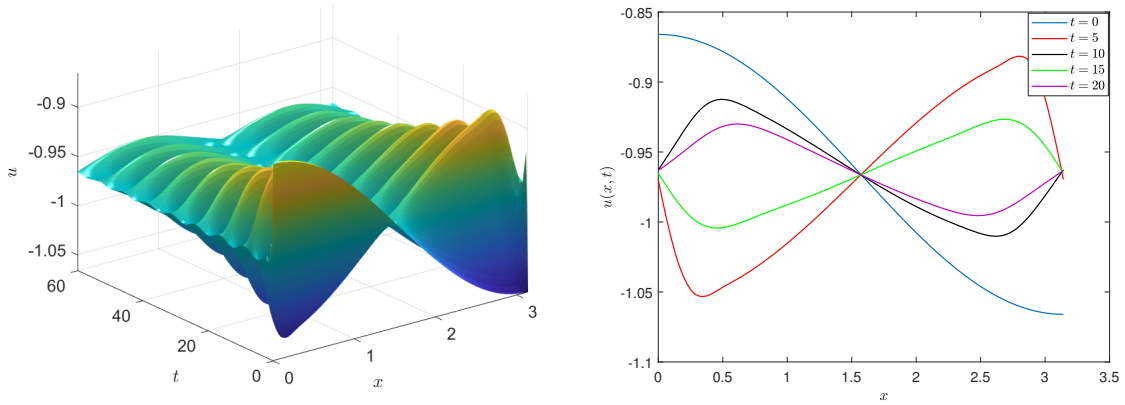

(a) (b)

Figure 3.13 (a) Space-time evolution of the wave mode $\cos x$ of system (2.2) for $\tau = 0.3$ ($< \tau_c$) and (b) Its temporal evolution at times indicated in the legend. Initial conditions were taken as $u(x,0) = u^* + 0.1\cos 1x$.

$\ell = \pi$, $a = 0.7$, $d = 0.005$, $b = 0.4$, and $\varepsilon = 0.8$. Damping in the system is due to the dissipation term u_t in Eq.(2.2).

Fig.3.14 shows the space-time plot of the membrane potential at the Pitchfork instability for two different values of the diffusion coefficient within the unstable range. Here, noise was added using the MATLAB function: $rand(size(n))$ and other system parameters were $a = 0.7$, $b = 0.4$, $\varepsilon = 0.8$, $\ell = \pi$, and $\tau = 0.6$. The stationary state displayed in the plot consist of regular stripes interrupted by localized spatial defects that run vertically through the figure. Spatially inhomogeneous stationary states represent regions of localized excitations and have been liked to memory formation.

Stability of plane wave solutions of the CGL equation

In this subsection, we determine the stability of various wave modes of Eq.(2.1), using the CGL(Eq.(2.82)) and we determine the stability of the homogeneous oscillations against side-band instability. Using the parameter values: $\varepsilon = 0.8$, $b = 0.4$, and $a = 0.7$ (see section 3.2), we obtain the steady state $u^* = -0.966$, and the corresponding critical value and frequency $\tau_0 \approx 0.363$ and $\omega_0 = 0.835$ respectively. Additionally, when $d = 0.5$ and $\ell = 200$, we find

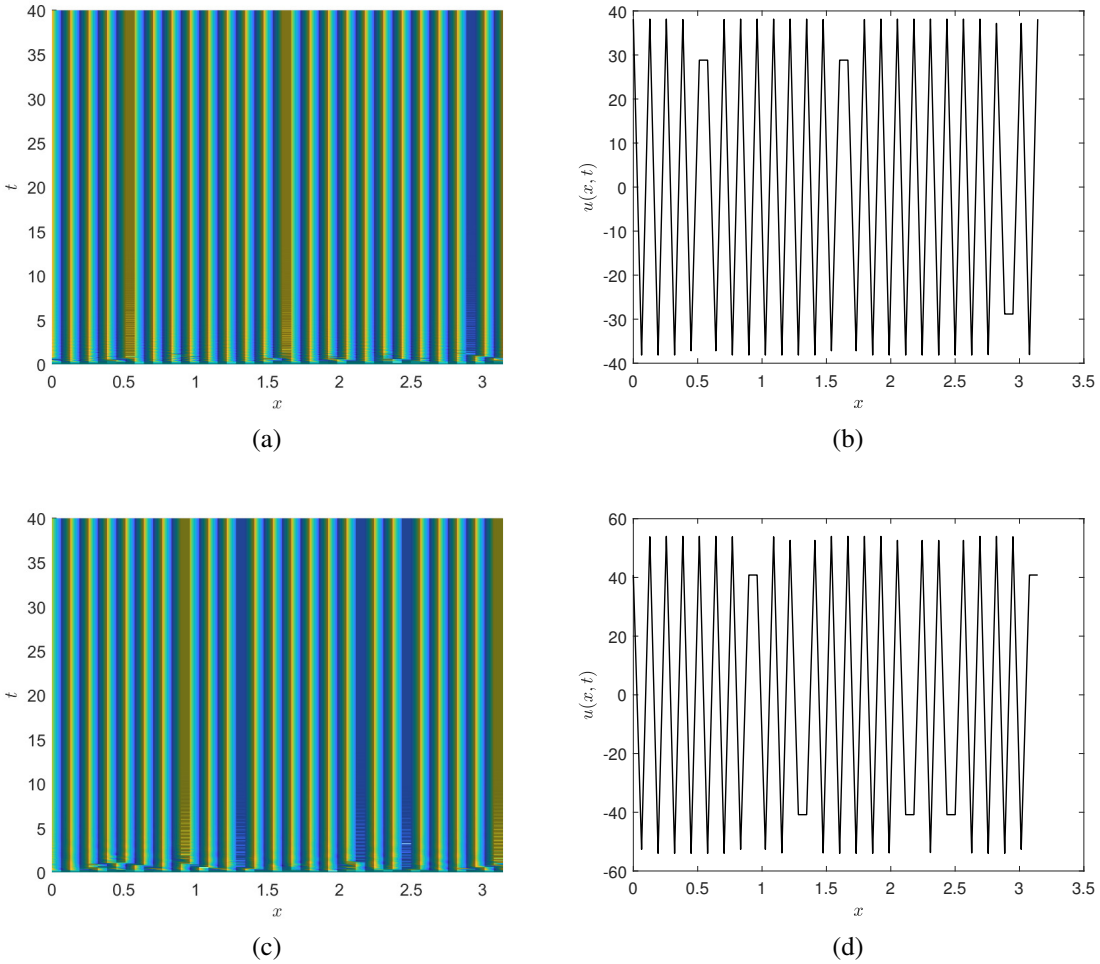

Figure 3.14 Space-time plot of membrane potential (left column) and a stationary wave at $t = 20$ (right column). Panels show a stationary state of system (2.2) emerging from random initial conditions $u^* = -0.966 + 0.03 \times noise$, $w^* = 0$ and $v^* = -0.665$. The diffusion coefficient was $d = -0.5$ for panels (a) and (b), and $d = -1$ for panels (c) and (d).

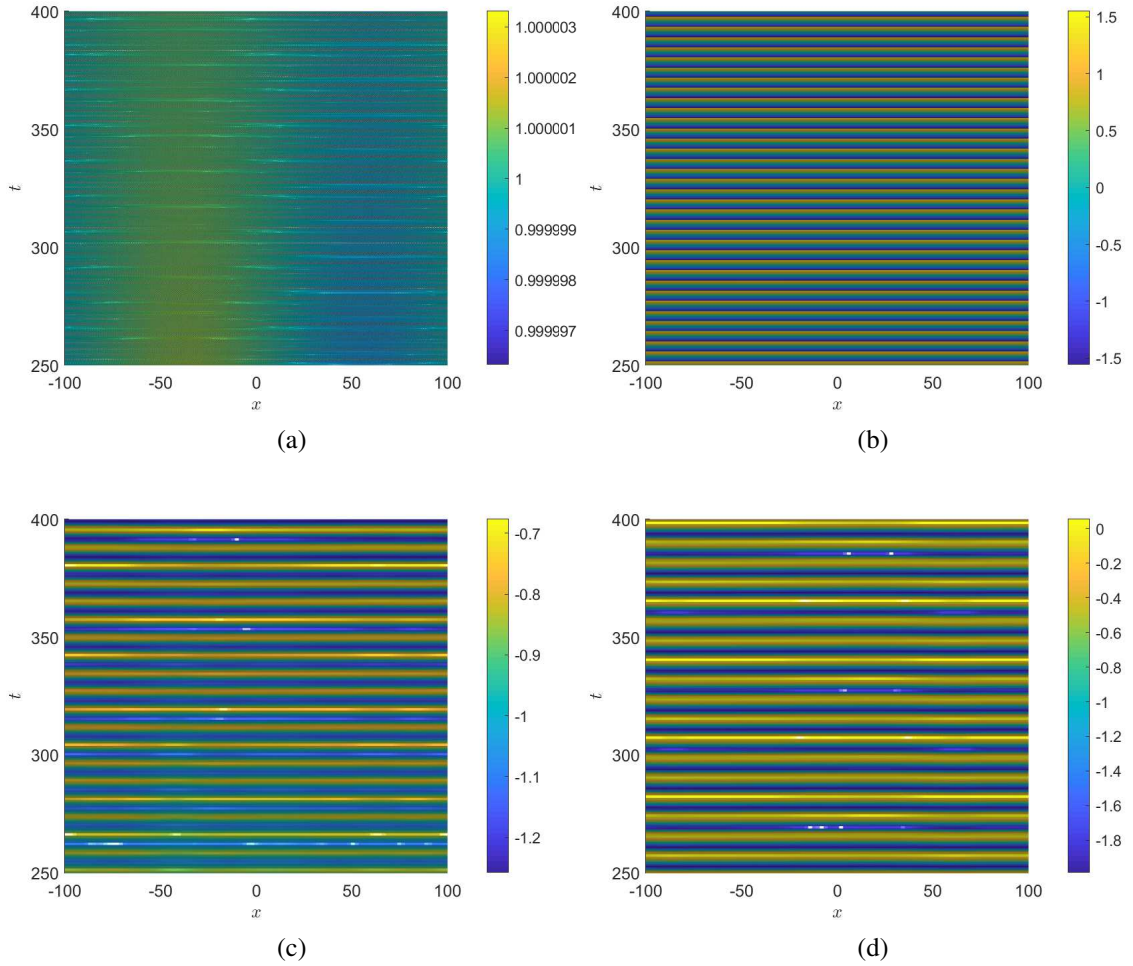

Figure 3.15 Space-time plot of evolution of the (a) intensity $|z|^2$ and (b) phase of the CGL (Eq.(2.82)), and membrane potential of system (2.2) for (c) $\tau = 1.1\tau_0$, and (d) $\tau = 1.7\tau_0$. For the CGL, initial conditions were $z_0 + noise$ while those for system (2.2) were $U = U_0 + noise$.

the coefficients of the CGl, Eq.(2.82), as

$$\begin{aligned} f_{1r} &= -3.434\times10^{-2}, \qquad f_{1i} = 2.5094\times10^{-2}, \\ f_{2r} &= 6.629\times10^{-2}, \qquad f_{2i} = -0.3783, \\ f_{3r} &= 1.869\times10^{-3}, \qquad f_{3i} = -1.366\times10^{-3}. \end{aligned} \tag{3.85}$$

It follows that, $c_1 \approx -5.7068, \qquad c_2 \approx -0.7307,$

Plane wave solutions of Eq.(2.82) are of the form:

$$z_k = \rho_k e^{i(kx+\hat{\omega}t)}, \tag{3.86}$$

with

$$|\rho_k|^2 = 1-k^2, \qquad \hat{\omega}_k = -c_2 + (c_2-c_1)k^2. \tag{3.87}$$

Under these condition, the spatially homogeneous oscillatory state takes the form:

$$z_0 = n_0 e^{i\hat{\omega}_0 t}, \quad |\rho_0|^2 = 1, \quad \hat{\omega}_0 = -c_2. \tag{3.88}$$

Notice that its frequency ($\hat{\omega}_0$) is strikingly similar to, that obtained from Eq.(3.48), using the same parameters. That is, $\hat{\omega}_0 \approx \omega_0 = 0.835$. This is an illustration of the impressive predictive power of the CGL. Furthermore, the homogeneous mode z_0, will be stable since the Benjamin-Feir condition i.e

$$1 + c_1 c_2 > 0, \tag{3.89}$$

is satisfied. This implies that a stable sideband $0 < k \leq k_E$, surrounds the homogeneous state [72, 157, 158], where

$$\begin{aligned} k_E &= \sqrt{\frac{1+c_1c_2}{3+2c_2^2+c_1c_2}} \\ &= 0.2674, \end{aligned} \tag{3.90}$$

is the location of the Eckhaus instability [159, 160], beyond which plane waves become unstable to phase perturbations. It follows that all simulations of wavenumber k, within the existence band, will converge towards a wavestate $|k| \leq k_E$, in the neighbourhood of the homogeneous mode $k = 0$. To simulate the stability of plane wave solutions ($k \neq 0$), we use initial conditions of the form

$$z_k(x,0) = noise + \sqrt{1-k^2}e^{ikx}, \tag{3.91}$$

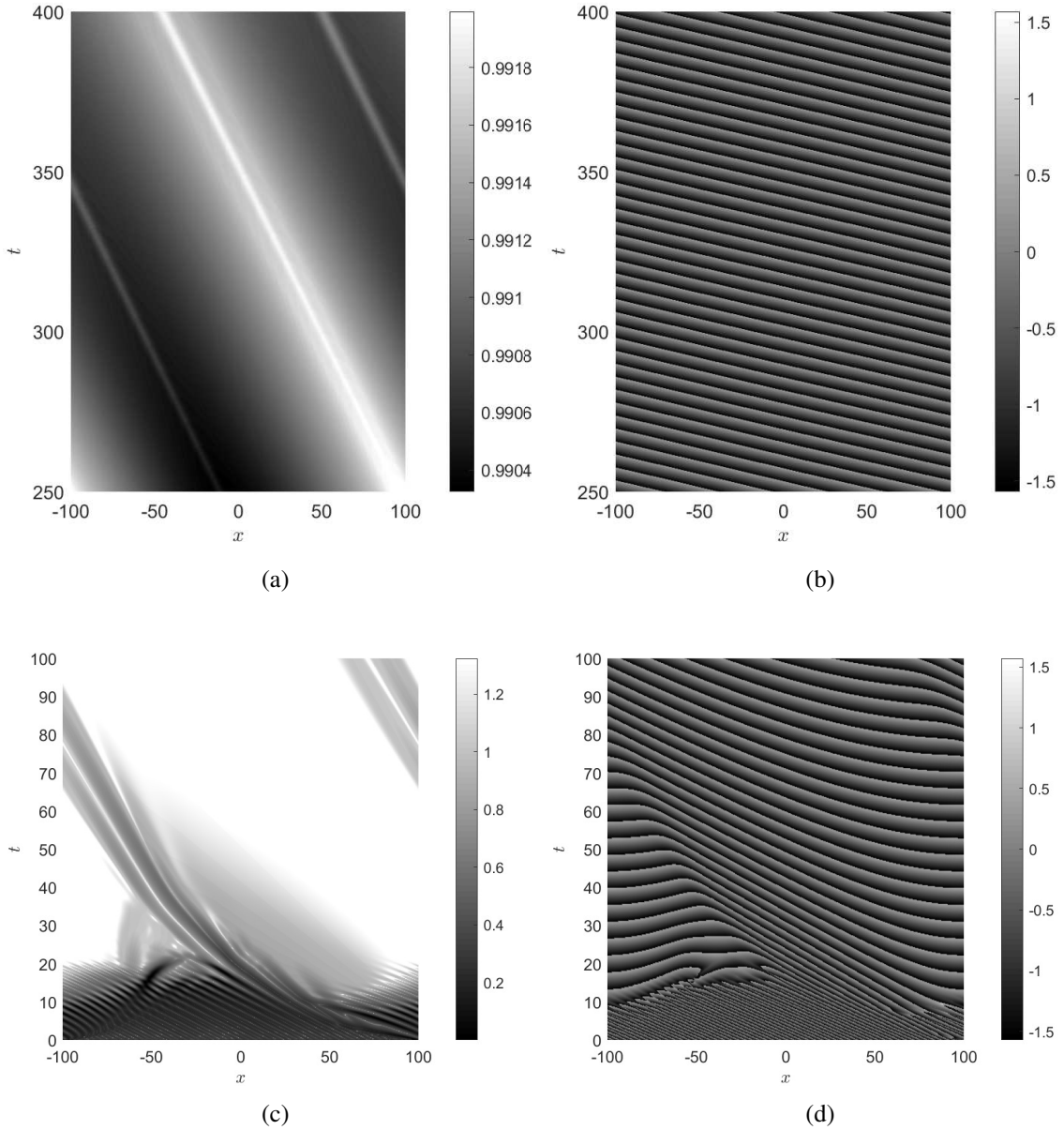

Figure 3.16 Space-time plot of the intensity $|z|^2$ (first column) and phase (second column) of the CGL for two different initial traveling waves $z_{0.1}$(Panels (a) and (b)), within and $z_{0.8}$(Panels (c) and (d)), outside the stable band, both subject to a small initial random perturbation implemented using the MATLAB function $rand(size(n))$, of amplitude 0.1.

and select wavenumbers within the stable and unstable ranges of the CGL as initial solutions and simulate their space time evolution. Fig.3.15 shows the spatiotemporal evolution of the homogeneous solutions of Eq.(2.2) and Eq.(2.82). Here, noise was added using the MATLAB function $rand(size(n))$ while other system parameters were set as $a = 0.7$, $b = 0.4$, $\varepsilon = 0.8$, $d = 0.5$ and $\ell = 200$. It can be seen that both solutions converge to a spatially homogeneous, temporally oscillating solution which remains stable in the long time limit and well above threshold. The results for $k > 0$ are displayed in Fig.3.16. In the stable range with mode $z_{0.1}$, the amplitude converges to a value $\approx \sqrt{1-0.1^2}$, while the phase settles to a spatially inhomogeneous state. Hence this mode is indeed stable against small perturbations and corresponds to neurons that fire out of phase with a frequency close to $\hat{\omega}_{0.1}$. For $k \gg k_E$, the amplitude and phase undergo perturbations. The foregoing numerical results and discussion suggests the homogeneous mode is stable to perturbations of wavenumber $0 < k \leq k_E$. Beyond the stable range ($k > k_E$), plane waves become unstable. In all simulations, the asymptotic solution has wave number in the range $0 < k \leq k_E$.

3.3.4 Discussions

In this section, we provided a framework to study delay and diffusion-induced instability in a spatially extended neuron with homogeneous Neumann boundary conditions. Unlike infinite-dimensional classical delayed reaction-diffusion systems, the current model is advantageous in the sense that only the diffusion and not the delay generates infinite dimensional character of the dynamical system. The latter approach is analytically and computationally easier to study. The results presented here suggest that the Hopf bifurcation results in oscillatory and traveling waves whose squared speeds are inversely proportional to the delay, are finite for large τ and infinite for negligible τ. This is a confirmation of experimental studies which suggests that axons without myelin sheath tend to propagate signals at relatively lower speeds resulting in more delayed pulses. Due to the dissipative character of the system, only damped traveling waves propagate in the system for small values of the relaxation time. However, in the large τ limit, oscillatory waves corresponding to the homogeneous mode dominate and are stable to side band instability. Our calculations also predicted a Pitchfork instability induced by negative diffusion (and independent of delay), although there is currently no experimental evidence of negative diffusion in biological neurons, to the best of our knowledge. Further research on the existence of this phenomenon is needed in order to confirm this aspect of our results.

3.4 Numerical bifurcation analysis of the discrete hyperbolic FHN model

Here, we present results on the bifurcation analysis of the discrete hyperbolic FHN model. Numerical bifurcation analysis of systems (2.109) and (2.110) was performed in MATCONT. For a review of essential bifurcations of maps see section 1.4.

For system (2.109) we used the following parameter set: $N = 31$, $\tau = 0.1$, $\varepsilon = 0.8$, $b = 0.4$, $a = 0.7$, $h = 1/30$ and $d = 0.001$. After locating a stable fixed point by numerical integration we study its codimension-one bifurcation, taking τ as the bifurcation parameter. The bifurcation diagram is displayed in Fig.3.17a with parameters set: $d = 0.001$, $\varepsilon = 0.8$, $b = 0.4$, and $a = 0.7$. We observe that as τ is increased, the first supercritical Hopf bifurcation occurs corresponding to mode $k = 0$, followed by a sequence of supercritical Hopf bifurcations presumably due to higher order modes ($k > 0$). Switching d from 0.001 to 0.1 and repeating the procedure above, we obtain the diagram for the pitchfork bifurcation displayed in Fig.3.17b. Here, we set $\tau = 0.1$ while other parameters were maintained at $\varepsilon = 0.8$, $b = 0.4$, and $a = 0.7$. In this plot, we observe the occurrence of a stationary bifurcation as d crosses zero from right to left. The first branch point corresponds to mode $k = 1$ and is followed presumably by a sequence of branch point bifurcations. In both codimension-one studies, the bifurcations obtained with system (2.2) are captured with good precision by the corresponding discrete system, system (2.109).

Next, we study the bifurcations of system (2.110) in a manner similar to the previous paragraph, by detecting the the codimension-one (codim 1) bifurcations. Fig.3.18a and 3.18b shows respectively, the codim-1 bifurcations with τ and I as bifurcation parameters. Note that these figures mirror those of system (2.2)(with $d = 0$), Figs.3.2a and 3.2b. Additionally, we continue these bifurcations on the codimension-two plane and obtain Fig.3.19. Once again, the essence of the codim-2 bifurcation diagram of system (2.2) ($d = 0$), Fig.3.3a has been captured by Fig.3.19. Due to limitations in software, we were unable to continue the detected Chenciner points.

3.4.1 Discussions

The motivation for studying the discrete FHN model stems from the fact that certain nerve transmission phenomena may best be discrete by discrete dynamics. A good discrete model which serves as an approximation to the corresponding continuous model should maintain to a high degree the properties and solutions of the continuous model. Such is the case with the discrete models we have proposed here. On the one hand, the model with

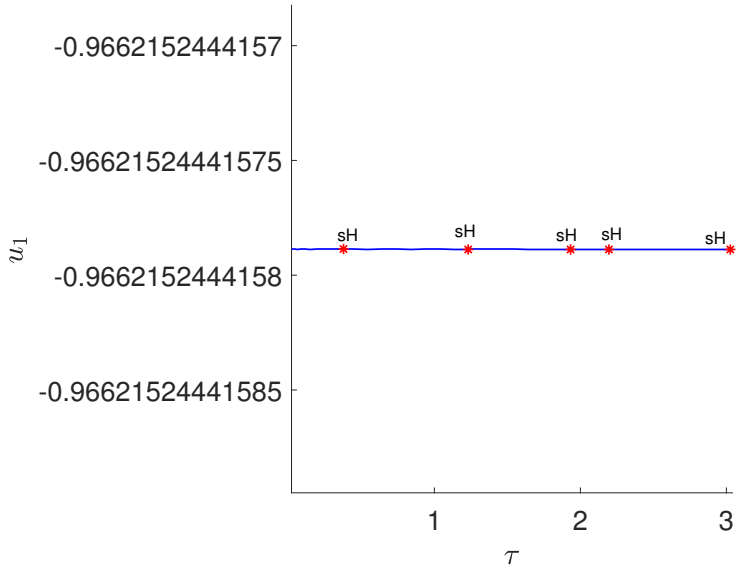

(a)

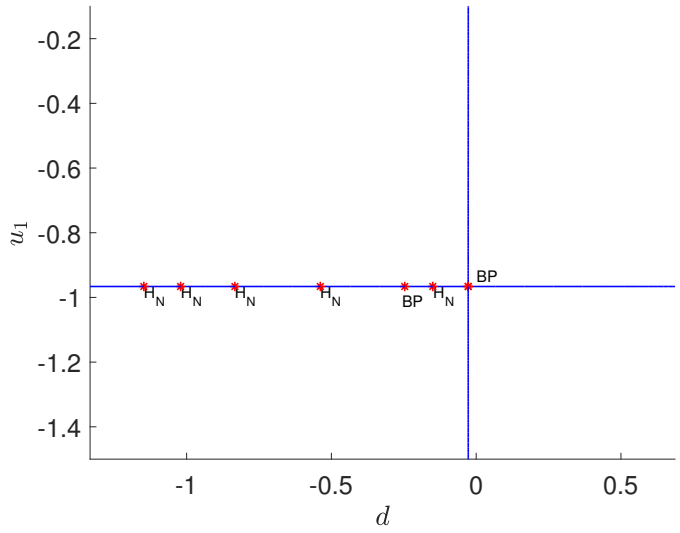

(b)

Figure 3.17 Codimension-one bifurcation diagrams of system (2.109) with bifurcation parameter (a) τ and (b) d. sH denotes superciritcal Hopf bifurcations, BP denotes a branch point or pitchfork bifurcation, and H_N denotes a neutral saddle. The horizontal (vertical) branch of equilibria bifurcating from BP represents spatially homogeneous (inhomogeneous) stationary states.

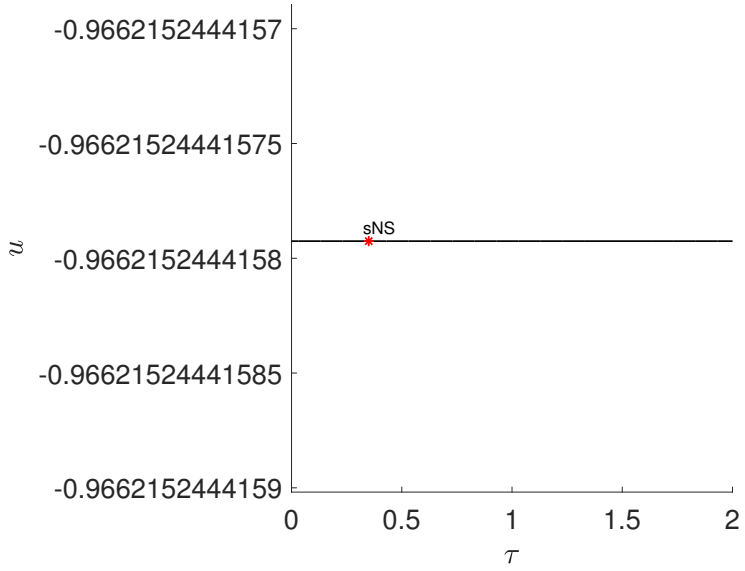

(a)

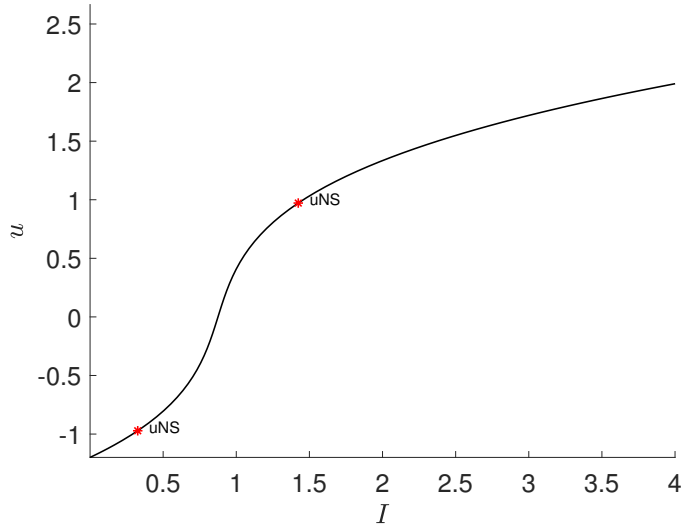

(b)

Figure 3.18 Codimension-one bifurcation diagrams of system(2.110) with bifurcation parameter (a) τ, and (b) I. sNs (uNs) denotes superciritcal (subcritical) Neimark-Sacker bifurcations. Parameters sets used for these simulations were: (a) $\varepsilon = 0.8$, $b = 0.4$, $a = 0.7$, and $dt = 0.01$ (b) $\varepsilon = 0.08$, $b = 0.8$, $a = 0.7$, and $dt = 0.01$.

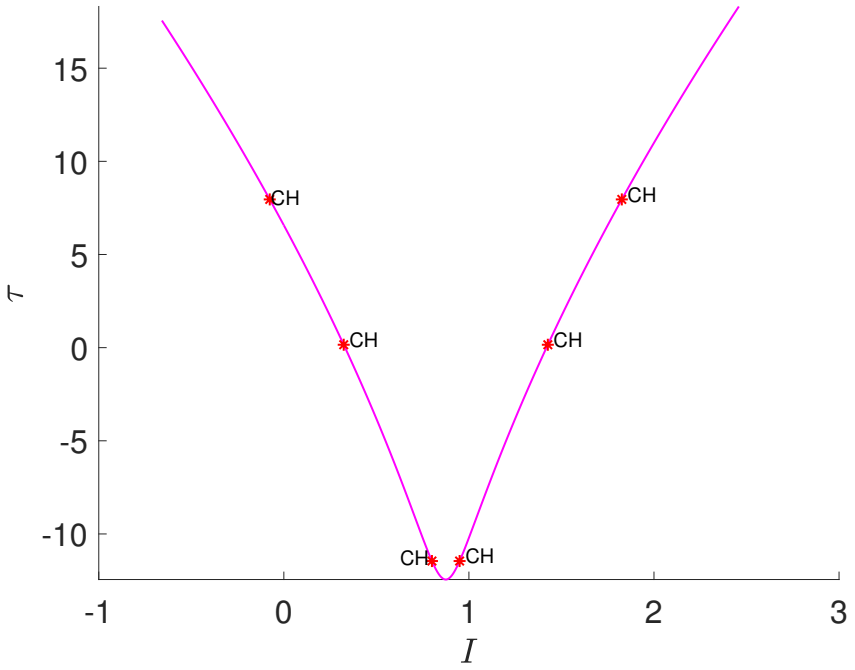

Figure 3.19 Codimension-two bifurcations of system (2.110) as seen on the $(\tau, I)-$ plane. Red curve is the NS curve while CH are nondegenerate Chenciner bifurcation. Parameter set used for the simulation is : $\varepsilon = 0.08$, $a = 0.7$, $b = 0.8$, and $dt = 0.01$.

discretizations in space replicated successfully, the primary bifurcations of the reaction-diffusion equation studied in section 3.3. Although the exact locations of these bifurcations in the discrete model were slightly off, relative to the continuous model, better accuracy may be achieved by increasing the number of mesh points used to discretize the Laplacian. Spurious bifurcations such as the neutral saddle (NS) were detected in the discrete model. These are usually induced by discretizations in space but their multiplicity usually drops as the discretization method is improved. On the other hand, discretizations in the time variable (without diffusion) successfully replicated the dynamics observed in section 3.2. Here, no spurious bifurcations were detected and high order accuracy was achieved even at moderately high time steps ($dt = 0.1$).

3.5 Dynamics of fronts and oscillons of the hyperbolic model

3.5.1 Analytical front solution by G'/G method

Assume the recovery variable of the neuron in system (2.1) is constant ($v_t = 0$), which without loss of generality, may be taken as zero. The corresponding system dynamics of the membrane potential is then given by:

$$\tau u_{tt} + u_t = u - \frac{u^3}{3} + u_{xx}. \tag{3.92}$$

In what follows we look for the analytical solution to this equation using the G'/G - expansion method, described in section 2.3.1.

Letting $u(x,t) = u(\xi)$ with $\xi = x - ct$, It follows that

$$(1 - \tau c^2)u'' + cu' + u - \frac{u^3}{3} = 0. \tag{3.93}$$

Assume $u(\xi)$ can be expanded as

$$u(\xi) = \sum_{m=0} \alpha_m (\frac{G'}{G})^m, \tag{3.94}$$

where $G(\xi)$ is the solution of Eq.(2.86).
We find a homogeneous balance between the terms u^3 and u'' in Eq.(3.93), where

$$u^3(\xi) = \alpha_m^3 (\frac{G'}{G})^m + \dots \tag{3.95}$$

$$u''(\xi) = m(m+1)\alpha_m (\frac{G'}{G}) + \dots. \tag{3.96}$$

It follows from the homogeneous balance that: $m + 2 = 3m$ and thus $m = 1$. Hence the desired solution is of the form:

$$u(\xi) = \alpha_0 + \alpha_1 (\frac{G'}{G}). \tag{3.97}$$

Substituting the expansions of Eq.(3.97), its derivatives u', u'' as well as that of the term u^3 into Eq.(3.93), we group terms of like-powers of $(\frac{G'}{G})$ together. Setting the coefficients of

each power of $(\frac{G'}{G})$ to zero, we obtain the following system of equations:

$$2\alpha_1(1-\tau c^2) - \frac{\alpha_1^3}{3} = 0 \tag{3.98}$$

$$3\alpha_1\lambda(1-\tau c^2) - \alpha_1 c - \alpha_1^2\alpha_0 = 0 \tag{3.99}$$

$$(1-\tau c^2)(2\alpha_1\mu + \alpha_1\lambda^2) - \alpha_1\lambda c + \alpha_1 - \alpha_1\alpha_0^2 = 0 \tag{3.100}$$

$$(1-\tau c^2)\alpha_1\lambda\mu - \alpha_1\mu c + \alpha_0 - \frac{\alpha_0^3}{3} = 0. \tag{3.101}$$

Solving this system on Maple, we obtain fifteen different solutions: seven of which have a constant velocity (independent of τ) and the rest with a velocity inversely proportional to the relaxation time, τ. One of the eight solutions with dependence on the delay has the following coefficients:

$$\alpha_0 = \sqrt{\frac{3}{2}}\left[1 + \frac{8\mu}{9\tau+2} + \sqrt{1+\frac{16\mu}{9\tau+2}}\right]^{\frac{1}{2}}. \tag{3.102}$$

$$\alpha_1 = \frac{\sqrt{6}}{4\mu}\frac{\left(\frac{8\mu}{9\tau+2} - 1 - \sqrt{1+\frac{16\mu}{9\tau+2}}\right)\sqrt{8\mu+9\tau+2-\sqrt{(9\tau+2)(16\mu+9\tau+2)}}}{27\tau+6-\sqrt{(9\tau+2)(16\mu+9\tau+2)}}, \tag{3.103}$$

with

$$c = \frac{3}{\sqrt{9\tau+2}} \tag{3.104}$$

$$\lambda = \frac{\sqrt{16\mu+9\tau+2}}{2}, \tag{3.105}$$

where μ is a real constant and $\lambda^2 - 4\mu > 0$. Substituting the general solution of Eq.(2.86) for the case where $\lambda^2 - 4\mu > 0$, into Eq.(3.97) we obtain as solution:

$$u(\xi) = \alpha_0 + \frac{\sqrt{9\tau+2}}{4}\alpha_1\left(\frac{C_1\sinh\frac{\sqrt{9\tau+2}}{4}\xi + C_2\cosh\frac{\sqrt{9\tau+2}}{4}\xi}{C_1\cosh\frac{\sqrt{9\tau+2}}{4}\xi + C_2\sinh\frac{\sqrt{9\tau+2}}{4}\xi}\right). \tag{3.106}$$

Letting $C_2 = 0$ we obtain the familiar shock type solution:

$$u(\xi) = \alpha_0 + \frac{\sqrt{9\tau+2}}{4}\alpha_1\tanh\frac{\sqrt{9\tau+2}}{4}\xi, \tag{3.107}$$

or more explicitly written:

$$u(x,t) = \alpha_0 + \frac{\sqrt{9\tau+2}}{4}\alpha_1\tanh\left(\frac{\sqrt{9\tau+2}x - 3t}{4}\right). \tag{3.108}$$

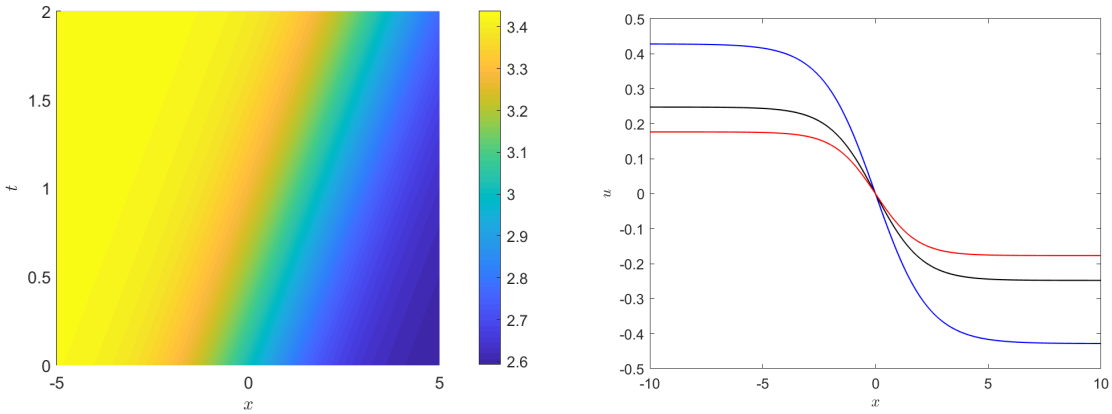

(a) (b)

Figure 3.20 Analytical front solution, Eq.(3.108) in space-time (left panel) at $\tau = 0.1$, and across the neuron (right panel) for $\tau = 0.1$, $\tau = 0.2$ and $\tau = 0.3$ (resp. blue, black and red lines). For all simulations $\mu = 0.9$ and $\alpha_0 = 0$.

The constant α_0 controls the vertical shift of the solution at $t = 0$ and may be taken as 0, without loss of generality. The profile of the front solution is displayed in Fig. 3.20 while its speed as a function of τ is plotted in Fig.3.22 .
To verify the analytical results obtained above, we simulate Eq. (3.92) using the method of lines by first transforming it into the system:

$$u_t = w \tag{3.109}$$

$$\tau w_t = u - \frac{u^3}{3} + u_{xx} - w. \tag{3.110}$$

The operator u_{xx} was discretized using a mesh of 200 points and the initial profile was taken from Eq.(3.108) as :

$$u(x,0) = \frac{\sqrt{9\tau+2}}{4}\alpha_1 \tanh\left(\frac{\sqrt{9\tau+2}x}{4}\right). \tag{3.111}$$

The results of the numerical simulation are shown in Fig. 3.21 which shows a localized front solution. This solution can be made to agree with the analytical solution, Eq.(3.108), viewed on the comoving frame.

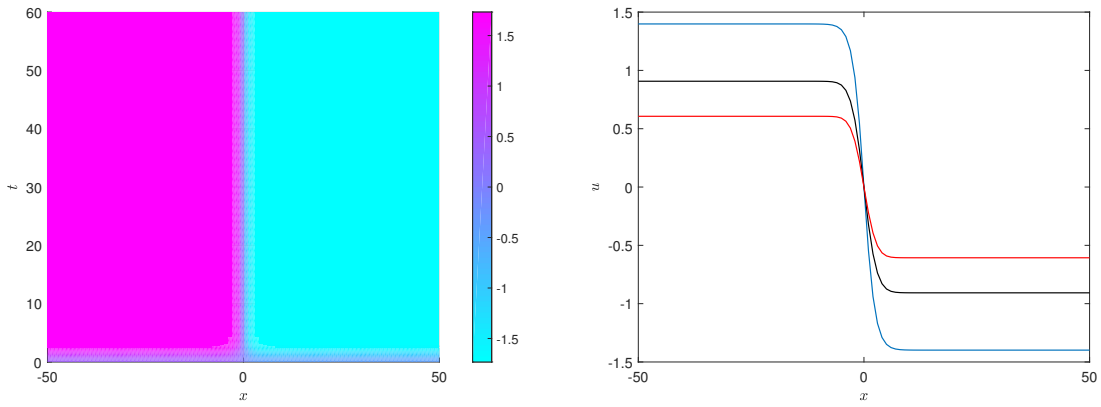

(a) (b)

Figure 3.21 Numerical front solution of system (3.92), showing (a) space-time plot at $\tau = 0.1$, and (b) solution across the neuron for different values of τ: 0.1, 0.2 and 0.3 corresponding to blue, black and red lines respectively.

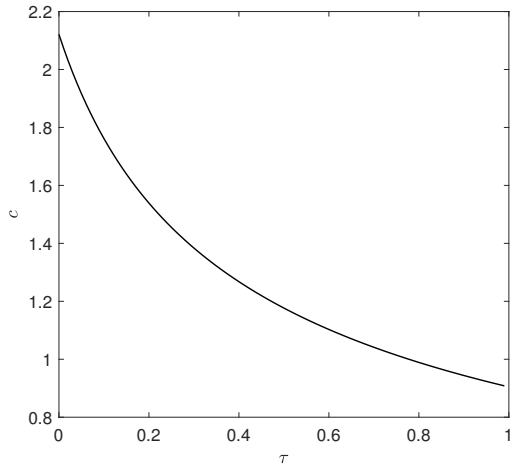

(a)

Figure 3.22 Variation of wave speed of front solution, Eq.(3.108), with relaxation time.

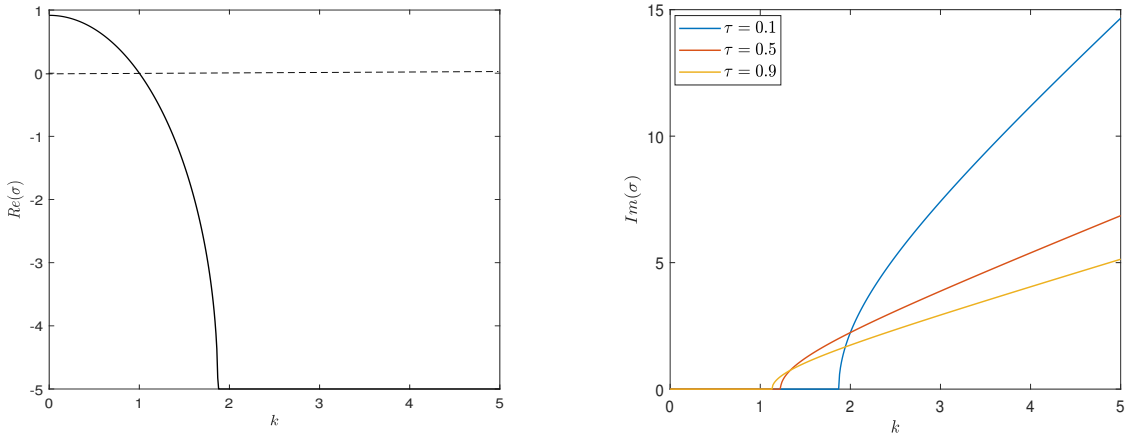

(a) (b)

Figure 3.23 (a) Shows the instability gain for system (2.1), Re(σ) against k for the mode ω_1 for $\tau = 0.1$; the dashed line is a visual aid. (b) The dispersion relation for the modes ω_1 at various values of τ and wavenumbers $0 < k < 5$. Other system parameters were $a = 0.7$, $b = 0.8$, $\varepsilon = 0$.

3.5.2 Wave properties of a propagating oscillon

Dispersion relations

Here, we use the method of multiple scales described in section 2.3.1 to reduce system (2.1) to the Hopf normal form from which we build an oscillon solution.

Taking into account Eqs.(2.103) and (2.104), and expanding system (2.1) up to order δ^3 we obtain the following relations:

At order δ^1, terms in $e^{i\tilde{p}\varphi}$ gives the following system

$$\mathbf{D}\mathbf{U_1} = 0, \tag{3.112}$$

with

$$\mathbf{D} = \begin{pmatrix} -\tau\omega^2\tilde{p}^2 - i\omega\tilde{p} + k^2\tilde{p}^2 - 1 & 1 \\ -\varepsilon & \varepsilon b - i\omega\tilde{p} \end{pmatrix}. \tag{3.113}$$

For $\mathbf{U_1} \neq 0$, equating the determinant of the matrix $\mathbf{D}$ to zero, gives the following third order characteristic equation

$$-\tau\omega^2\tilde{p}^2 - i\omega\tilde{p} + k^2\tilde{p}^2 + \eta - 1 = 0, \tag{3.114}$$

with $\eta = \frac{\varepsilon}{\varepsilon b - i\omega\tilde{p}}$, $\varepsilon b \neq i\omega\tilde{p}$.
The roots of Eq.3.114, represent different modes of wave propagation. An analytical search for these roots is quite challenging. As such, only a qualitative description of the instabilities will be done for the case $\varepsilon = 0$ while those for the third order polynomial is to be evaluated numerically. In what follows, we shall also ignore multiple wave interactions by focusing on the first harmonic ($u_1^{\tilde{p}} = 0$ if $\tilde{p} \neq 1, -1$).

Case: $\varepsilon = 0$

When the recovery variable is ignored, the dispersion relation, Eq.(3.114) becomes

$$-\tau\omega^2 - i\omega + k^2 - 1 = 0. \tag{3.115}$$

Assuming $k \in \mathbb{R}$ and a temporal representation of the dispersion relation with $\omega = \omega(k)$—a complex function, solutions to Eq.(3.115) can be obtained easily as:

$$\omega_{1,2} = \frac{-i \pm \sqrt{4\tau(k^2-1)-1}}{2\tau}. \tag{3.116}$$

The eigenvalues $\omega_{1,2}$ are the modes of propagation of the signal. To understand their physical significance, let us consider plane wave solutions of the form $\mathbf{U}e^{i(kx-\omega t)}$. This can conveniently be represented as $\mathbf{U}e^{ikx-i\omega_r t+\omega_i t}$ or simply as $\mathbf{U}e^{ikx+\sigma t}$ where, $\sigma = -i\omega$. Here $\mathrm{Re}(\sigma)$ represents the gain or growth rate of the perturbation while $\mathrm{Im}(\sigma)$ is responsible for the periodic behavior (Phase velocity) of the of the signal. For any wavenumber k, the plane wave is temporally unstable (stable) if $\mathrm{Re}(\sigma) > 0$ ($\mathrm{Re}(\sigma) \leq 0$). The critical modes are those for which $\mathrm{Re}(\sigma) = 0$ or $\omega_i = 0$ and correspond to oscillating solutions. Defining the phase velocity

$$v_p = \frac{\mathrm{Re}(\omega_{1,2})}{k},$$

we have that

$$v_p = \begin{cases} 0, & k^2 < \frac{1}{4\tau} + 1 \\ \pm\frac{\sqrt{4\tau(k^2-1)-1}}{2\tau}, & k^2 \geq \frac{1}{4\tau} + 1. \end{cases} \tag{3.117}$$

We conclude there exist a critical wavenumber $k_{c1} = \frac{1}{4\tau} + 1$ and that no plane waves exist for $k < k_{c1}$. Fig.3.23 shows the plot of $\mathrm{Re}(\sigma)$ and $\mathrm{Im}(\sigma)$ against k for mode ω_1 for different values of τ. For each case, we observe that when $k < k_{c1}$ ($k \geq k_{c1}$), plane waves are temporally unstable (stable). No periodic pattern is observed in the former case while damped waves, propagating towards the left or right, may be observed in the latter case.

Case: $\varepsilon \neq 0$

In this case, Eq.(3.114) can be put in the form of a polynomial with real coefficients as follows

$$\tau\sigma^3 + (b\tau\varepsilon + 1)\sigma^2 + (b\varepsilon + k^2 - 1)\sigma + \varepsilon(b(k^2-1)+1) = 0. \tag{3.118}$$

wherein we have made use of the substitution $\sigma = -i\omega$, with σ bearing the same definition as before. Using a suitable Newton solver (the function $roots(a_n, a_{n-1}, \dots)$, in MATLAB), the roots of the polynomial dispersion relation given by Eq.(3.118) can computed. The results for $0 \leq k \leq 2$ are shown in Table 3.1. Mode σ_1 has no wave solutions since $\mathrm{Im}(\sigma_1) = 0$ and $\mathrm{Re}(\sigma_1) < 0 \; \forall k > 0$. Modes $\sigma_{2,3}$, has wave solutions for some values of k with $\mathrm{Im}(\sigma_{2,3}) \neq 0$. The conjugate nature of $\sigma_{2,3}$ at periodic states reflects propagation towards the left and right directions.

An oscillatory periodic state is achieved when a pair of roots lie on the imaginary axis, this corresponds to a Hopf bifurcation. Suppose Eq.(3.118) has a pair of roots on the imaginary axis so that one root r_1 is real and the others r_2 and $r_3 = \bar{r}_2$, are complex. Using Vieta's formulas, we obtain the following equations (relating the roots to the coefficients of the polynomial equation):

$$r_1 = -\frac{(1+\tau b\varepsilon)}{\tau}, \tag{3.119}$$

$$|r_2|^2 = \frac{\varepsilon b + k^2 - 1}{\tau}, \tag{3.120}$$

$$r_1|r_2|^2 = -\frac{\varepsilon(b(k^2-1)+1)}{\tau}. \tag{3.121}$$

It follows that

$$(1+\tau\varepsilon b)(\varepsilon b + k^2 - 1) = \tau\varepsilon(b(k^2-1)+1). \tag{3.122}$$

from which we obtain the critical value

$$k_{c2} = \sqrt{1 + \varepsilon(\tau - b) - \tau b^2\varepsilon^2)}. \tag{3.123}$$

Eq.(3.120) gives us the frequency of oscillation (ω) at the critical value. That is,

$$\omega_c = \sqrt{\frac{b\varepsilon + k_{c2}^2 - 1}{\tau}}. \tag{3.124}$$

	σ_1	σ_2	σ_3
k=0	-10.9223	0.0174	0.8409
k=0.2	-10.8885	0.8032	0.0212
k=0.4	-10.7857	0.0355	0.6863
k=0.6	-10.6103	0.0787	0.4677
k=0.8	-10.3552	0.1456 + 0.1839i	0.1456 - 0.1839i
k=1.0	-10.0080	-0.0280 + 0.2813i	-0.0280 - 0.2813i
k=1.2	-9.54801	-0.2580 + 0.2161i	-0.2580 - 0.2161i
k=1.4	-8.93576	-0.1642	-0.9641
k=1.6	-8.08217	-0.1195	-1.8623
k=1.8	-0.10139	-6.6497	-3.3129
k=2.0	-0.09150	-4.9863 + 2.2057i	-4.9863 - 2.2057i

Table 3.1 Roots of the polynomial, Eq.(3.118), obtained by numerical iteration of k within the range $0 < k < 2$ with a step size of 0.2. Three roots exist for each k, and represent the three modes of propagation σ_1,σ_2 and σ_3. Other parameters were $\tau = 0.1$, $\varepsilon = 0.08$, $b = 0.8$ and $a = 0.7$

At order (δ^2) of the expansion, we have the following system of equations:

$$(-\tau\omega^2\tilde{p}^2 - i\omega\tilde{p} + k^2\tilde{p}^2)u_2^{\tilde{p}} + (1 - 2i\tau\omega\tilde{p})u_{1T} - 2i\tilde{p}ku_{1\xi}^{\tilde{p}} = u_2^{\tilde{p}} - v_2^{\tilde{p}}, \tag{3.125}$$

$$-i\omega\tilde{p}v_2^{\tilde{p}} + v_{1T}^{\tilde{p}} = \varepsilon u_2^{\tilde{p}} - \varepsilon b v_2^{\tilde{p}}. \tag{3.126}$$

Making use of the relation $v_{1T}^{\tilde{p}} = \eta u_{1T}^{\tilde{p}}$, obtained from System.(3.112) and the dispersion relation Eq.(3.114), terms in $u_2^{\tilde{p}}$ vanish and system (3.125) reduces to

$$\left(1 - 2i\tau\omega\tilde{p} - \frac{\eta^2}{\varepsilon}\right)u_{1T}^{\tilde{p}} - 2i\tilde{p}ku_{1\xi}^{\tilde{p}} = 0. \tag{3.127}$$

We let the coefficient of u_{1T} in Eq.(3.127) be a complex frequency:

$$\Omega = \frac{1}{2i}\left(1 - 2i\tau\omega\tilde{p} - \frac{\eta^2}{\varepsilon}\right), \tag{3.128}$$

whose full expression can be found in Appendix A.2. Eq.(3.127), at $\tilde{p} = 1$, becomes

$$2i\Omega u_{1T}^1 - 2iku_{1\xi}^1 = 0. \tag{3.129}$$

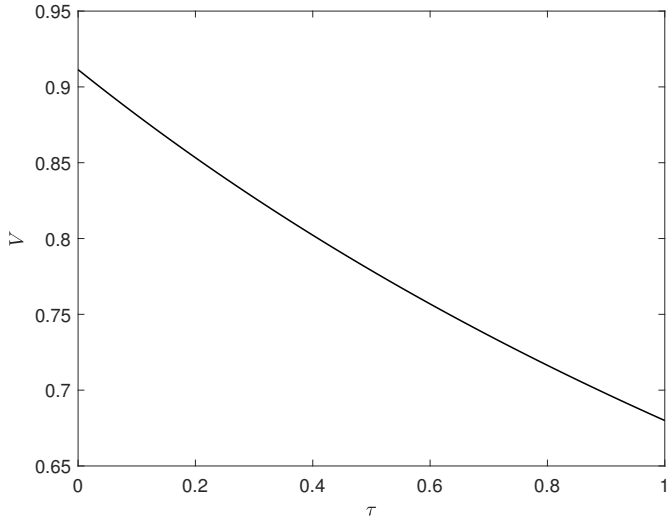

Figure 3.24 Plot of the group velocity of traveling pulses given by relation (3.131) for $k = 0.8$ and $\omega = -0.1839 + 0.1456i$. This frequency was obtained from table 3.1. Other parameters were $a = 0.7$, $\varepsilon = 0.08$ and $b = 0.8$

which is the well known transport equation with solutions of the form

$$u_1^1 = A(\xi + Vt), \tag{3.130}$$

corresponding to the propagation of a left-moving traveling pulse (wave-packet) with group velocity

$$V = \mathrm{Re}(\frac{k}{\Omega}). \tag{3.131}$$

Figure (3.24) shows the plot of V as a function of τ. Notice that V stays finite even when $\tau \to 0$ in contrast wave propagation of periodic waves for which the phase velocity $v_p = \frac{\omega_c}{k} \to \infty$ as $\tau \to 0$.

Amplitude equations

We now derive the canonical model governing the system dynamics at the Hopf bifurcation point. At order δ^3 of the perturbative expansion we get:

$$(-\tau\omega^2\tilde{p}^2 - i\omega\tilde{p} + k^2\tilde{p}^2 - 1)u_3^{\tilde{p}} + (1 - 2i\tau\omega\tilde{p})u_{2T}^{\tilde{p}} + (1 - 2i\tau\omega\tilde{p})u_{1\tilde{\tau}}^{\tilde{p}} + \tau u_{1TT}^{\tilde{p}} - 2i\tilde{p}ku_{2\xi}^{\tilde{p}} - u_{1\xi\xi}^{\tilde{p}} = -\frac{R_3^{\tilde{p}}}{3} - v_3^{\tilde{p}}. \tag{3.132}$$

where $R_3^{\tilde{p}}$ and $v_3^{\tilde{p}}$ are given by

$$v_3^{\tilde{p}} = \eta u_3^{\tilde{p}} - \eta^2 \frac{u_{2T}^{\tilde{p}}}{\varepsilon} - \eta^2 \frac{u_{1\tilde{\tau}}^{\tilde{p}}}{\varepsilon} + \eta^3 \frac{u_{1TT}^{\tilde{p}}}{\varepsilon^2}, \tag{3.133}$$

$$\text{and } R_3^{\tilde{p}} = \sum_{h+l+m=\tilde{p}} u_1^3. \tag{3.134}$$

where, h, l , m take integer values in the set $\{-2,-1,0,1,2\}$. Making use of the dispersion relation, Eq.(3.114) and relations, (3.133) and (3.134), Eqs.(3.132) for $\tilde{p}=1$ simplifies to

$$2i\Omega u_{2T}^1 - 2iku_{2\xi}^1 + 2i\Omega A_{1\tilde{\tau}} - A_{1\xi\xi} + \left(\tau + \frac{\eta^3}{\varepsilon^2}\right) A_{1TT} + |A|^2 A = 0. \tag{3.135}$$

where we have made use of Eq.(3.128), Eq.(3.130) and the fact that $R_3^1 = 3|u_1^1|^2 u_1^1$, while the terms in u_3^1 cancel each other. Placing ourselves on the frame of motion of the wave-packet, by using the transformations

$$\tilde{\xi} = \xi + VT, \text{ and } \tilde{T} = T, \tag{3.136}$$

Eq.(3.135) can be written as

$$\partial_{\tilde{T}} u_2^1 = \Phi(\tilde{\xi}). \tag{3.137}$$

Integrating this equation with respect to $\tilde{T}$, we have

$$u_2^1 = \tilde{T}\Phi(\tilde{\xi}) + u_2^1(0). \tag{3.138}$$

At large values of $\tilde{T}$, u_2^1 becomes a secular term in the perturbation expansion Eq.(2.104) and the latter breaks down. This can be removed by taking

$$\lim_{\tilde{T}\to+\infty} \left(\frac{u_2^1}{\tilde{T}}\right) = 0. \tag{3.139}$$

That is, we set $\Phi(\tilde{\xi}) = 0$, from which we get the following complex Ginzburg-Landau equation (CGL)

$$2i\Omega A_{\tilde{\tau}} + \left[\frac{k^2}{\Omega^2}(\tau + \frac{\eta^3}{\varepsilon^2}) - 1\right] A_{\tilde{\xi}\tilde{\xi}} + |A|^2 A = 0, \tag{3.140}$$

without the small parameter (δ) and critical frequency ω_c. This equation may be written in the generalized form

$$iA_\tau + PA_{\xi\xi} + Q|A|^2 A = 0, \tag{3.141}$$

dropping the hats on τ and ξ. Here, P and Q are complex coefficients given by

$$P = \frac{1}{2\Omega}\left[\frac{k^2}{\Omega^2}(\tau + \frac{\eta^3}{\varepsilon^2}) - 1\right], \tag{3.142}$$

$$\text{and } Q = \frac{1}{2\Omega}. \tag{3.143}$$

Full expressions for these coefficients (P_r, P_i, Q_r and Q_i) can be found in Appendix A.2. Equation (3.141) represents the slow evolution of the most unstable modes (A) on the center manifold at the Hopf bifurcation point. The linear dispersive coefficient (P), leads the spreading of the wave amplitude A, in space, while Q represents its nonlinear saturation. Eq.(3.141) has traveling wave solutions [35], as well as solitary solutions[161, 162] of the form:

$$A = \sqrt{\frac{2F}{H}} sech\left(\sqrt{2F}c_2 + \sqrt{\frac{F}{G}}z\right) e^{i(m\xi - nt)}, \tag{3.144}$$

where

$$z = \xi + Vt \tag{3.145}$$

$$F = m^2(P_r + \gamma P_i) - n^2, \tag{3.146}$$

$$G = P_r + \gamma P_i, \tag{3.147}$$

$$H = \gamma Q_i + Q_r, \tag{3.148}$$

$$\text{and } \gamma = \frac{2mP_i}{2mP_r + V}, \tag{3.149}$$

valid in the limit $\frac{2F - HA^2}{2G} > 0$, $\sqrt{\frac{F}{G}} > 0$ and $\sqrt{\frac{F}{H}} > 0$. This solution consist of a carrier wave ($e^{i(m\xi - nt)}$) modulated by an envelop ($sech$). Details of the derivation of this solution by direct integration of Eq.(3.141), is found in section 2.3.1. The coefficient c_2 controls the position of the solitary wave in 1D-space and can be conveniently set to zero.
The general solution of our system is obtained by substituting Eq.(3.144) into Eq.(2.105) to obtain

$$u = 2\sqrt{\frac{2F}{H}} e^{\omega_i t} sech\left(\sqrt{2F}c_2 + \sqrt{\frac{F}{G}}x\right) \times cos\left[(m+k)x - (n+\omega_r)t\right], \tag{3.150}$$

which is the exact solution for the oscillon of Eq.(2.1) (see Fig.3.25a). The profile has the shape of a “Mexican-hat"[163], indicating local excitation and lateral inhibition. This profile is similar to that reported in Ref.[164], in which a neuron model with hyperbolic based dynamics was studied. The amplitude of the envelope solution, Eq.(3.150), grows

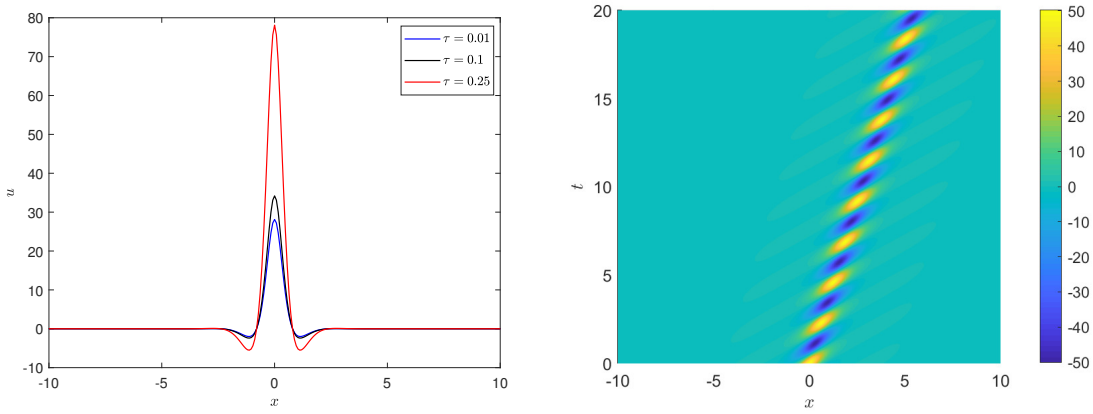

(a) (b)

Figure 3.25 (a) Profile of oscillon given by relation (3.150) at $t = 0$ and (b) its evolution in space-time (top-view). Simulation parameters were $k = k_c = 0.9714$, $\omega_r = 0.2755$, $\omega_i = 0$, $m = 1$, $n = 3$, $a = 0.7$, $b = 0.8$, $\varepsilon = 0.08$, and $c_2 = 0$.

exponentially for $\omega_i > 0$, decays if $\omega_i < 0$, and oscillates if $\omega_i = 0$. The spatio-temporal evolution this oscillon is plotted in Fig.3.25b. Yang et al.[165], have studied the birth and interaction of oscillons born from a subcritical Hopf bifurcation in a reaction diffusion system.

3.6 Burst synchronization in two coupled photosensitive hyperbolic FHN neurons

In this section, we present results on the codimension-two bifurcation diagram and burst synchronization of system (2.12). Our results are based on the unique equilibrium of this system which is the unique real root of the equation

$$u^3 + 3u\frac{(1+b(\xi-1))}{b} + 3\frac{a-bu_s}{b} = 0, \tag{3.151}$$

The unique real root is guaranteed under the constraints

$$\begin{aligned} D &= \frac{-108(1+b(\xi-1))^3 - 243b(a-bu_s)^2}{b^3} < 0, \\ b &> 1, \\ \xi &> \frac{b-1}{b}, \end{aligned} \tag{3.152}$$

where D is the discriminant of Eq.(3.151), defined according to lemma 1.

3.6.1 Numerical analysis

Codimension-two analysis of the photosensitve neuron

We compute numerically, the codimension-two bifurcations of Eq.(2.12) on the ξ, u_s plane. All detected bifurcations and continuations of system (2.12) were performed performed using MATCONT [106]. We begin the codimension-two analysis of the system by studying the primary bifurcation curve, taking u_s as the primary bifurcation parameter. Starting from the unique steady state and detecting the Hopf bifurcations induced by u_s, we continue this curve in the (u_s, ξ) plane as a function of τ. The Codimension-two bifurcation diagram as a function of τ is displayed in Fig.3.26. Parameter set used for this figure was $a = 0.7$, $b = 1.5$, $\varepsilon = 0.08$, and $\xi = 0.4$. GH_1 and GH_2 are nondegenerate Bautin bifurcation points with $l_2(0) < 0$. Fig.3.27 shows the time series of the potential in different regions of the codimension-two plane. To initiate bursting mechanisms, we fix $u_s = u_0 + A\sin\omega t$, as a time-periodic sinusoidal output from the phototube. Here, u_0, specifies the center of oscillation of u_s, while A specifies the amplitude of oscillation from this center; ω being the speed of oscillation. Assuming ξ is held fixed, two main bursting mechanisms are possible, displayed in Fig.3.28 with parameter set as $a = 0.7$, $\varepsilon = 0.08$, $\tau = 0.1$, and $b = 1.5$. Note that as the parameter τ increases in Fig.3.26, the Bautin points shift towards the left of the plane in the region with $\xi < 0$, corresponding to negative resistances. As such for positive ξ, the incidence of elliptic bursting within this range may reduce as τ increases, leaving only Hopf-Hopf bursting as the only bursting mode. We observe that when the frequency of the photocurrent increases, independent of the type of burst, the interburst interval decreases while the number of spikes within each burst decreases. Note that the number of spikes within each burst and the temporal evolution of the latter is believed to be a mechanism for temporal information encoding in neurons [38].

Synchronization of elliptic bursters

In this subsection, we consider the synchronization of two elliptic bursters coupled via different coupling schemes. It is known that two main modes of synchronization are possible for coupled bursters: spike synchronization within bursts and burst synchronization[76]. Both types of synchronization can be achieved with relative ease in elliptic bursters, compared to other types of bursters such as circle-circle bursters. It has been shown [76] that for weakly coupled elliptic bursters, spike synchronization depends crucially on the interspike frequencies and coupling scheme between the bursters. For weakly coupled elliptic bursters,

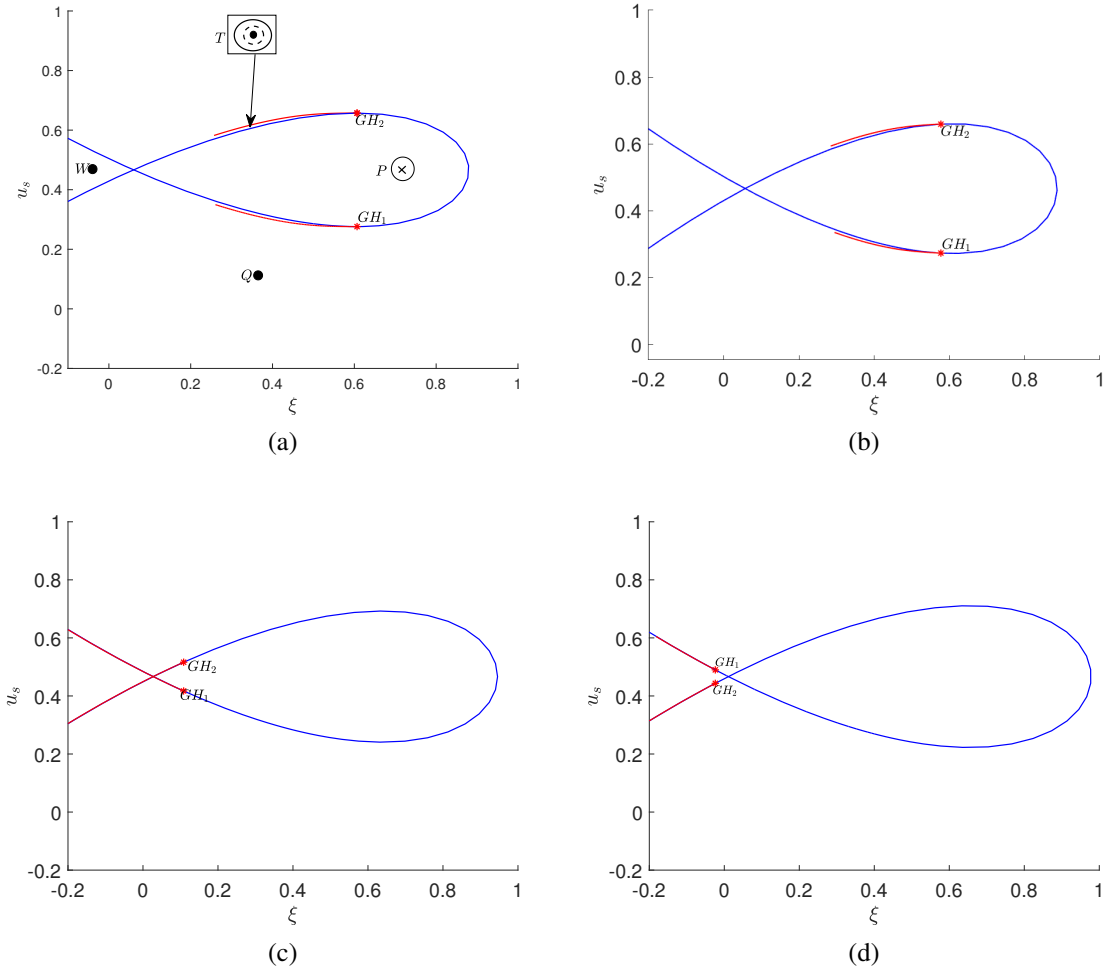

Figure 3.26 Codimension-two plane (ξ, u_s) of system (2.12), depicting different domains; W, T, Q, and P, with qualitatively distinct dynamics for (a) $\tau = 0$, (b) $\tau = 0.1$, (c) $\tau = 1$, and (d) $\tau = 1.5$. Filled circles (crosses) denote stable (unstable) fixed points. Uninterrupted (dashed) circles denote stable (unstable) periodic orbits. $GH_{1,2}$ are nondegenerate Bautin bifurcation points. Red(blue) curve corresponds to limit point of cycles (Hopf).

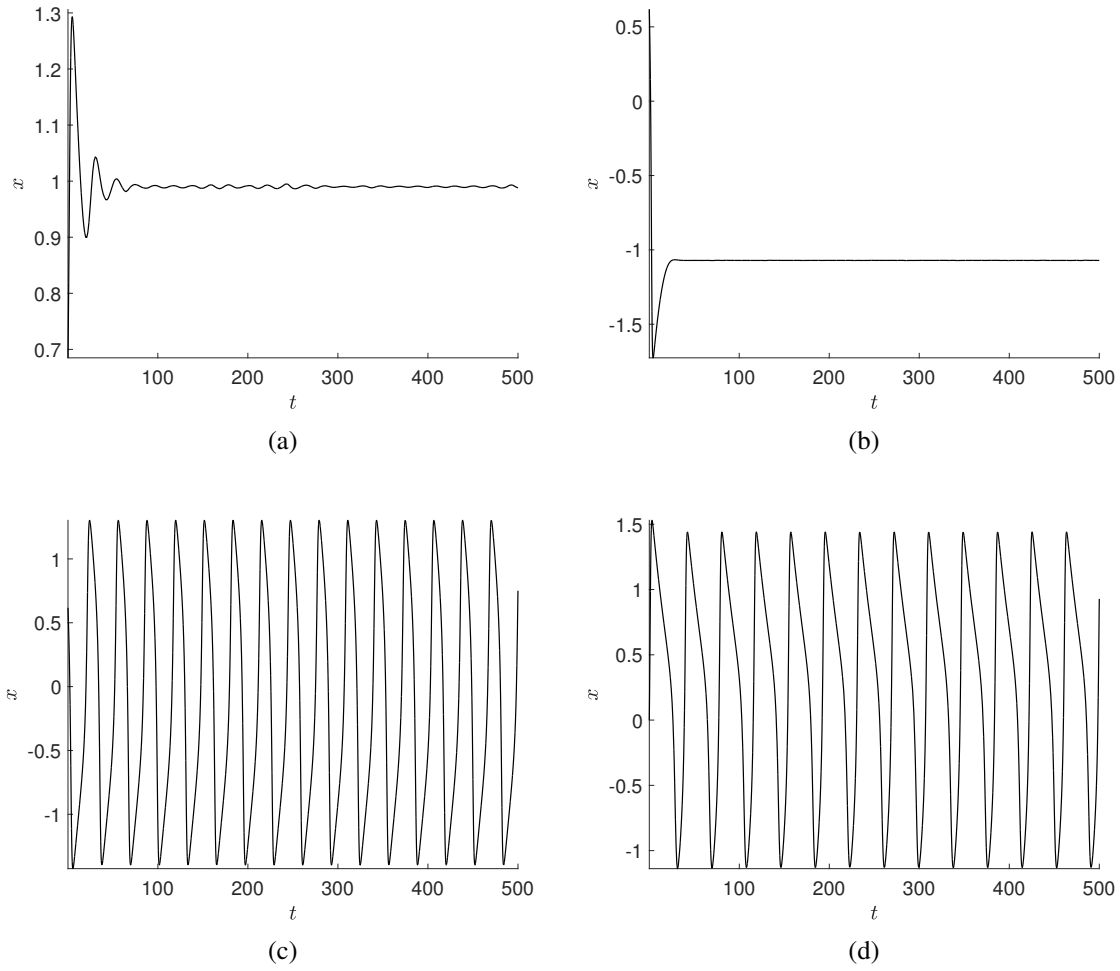

Figure 3.27 Time series of membrane potential of system (2.12) in different regions of the (ξ, u_s)-codimension-two plane with (ξ, u_s) in: (a) W, (b) Q, (c) P, and (d) T. The remaining parameters were set as $a = 0.7$, $\varepsilon = 0.08$, $\tau = 0.1$, and $b = 1.5$.

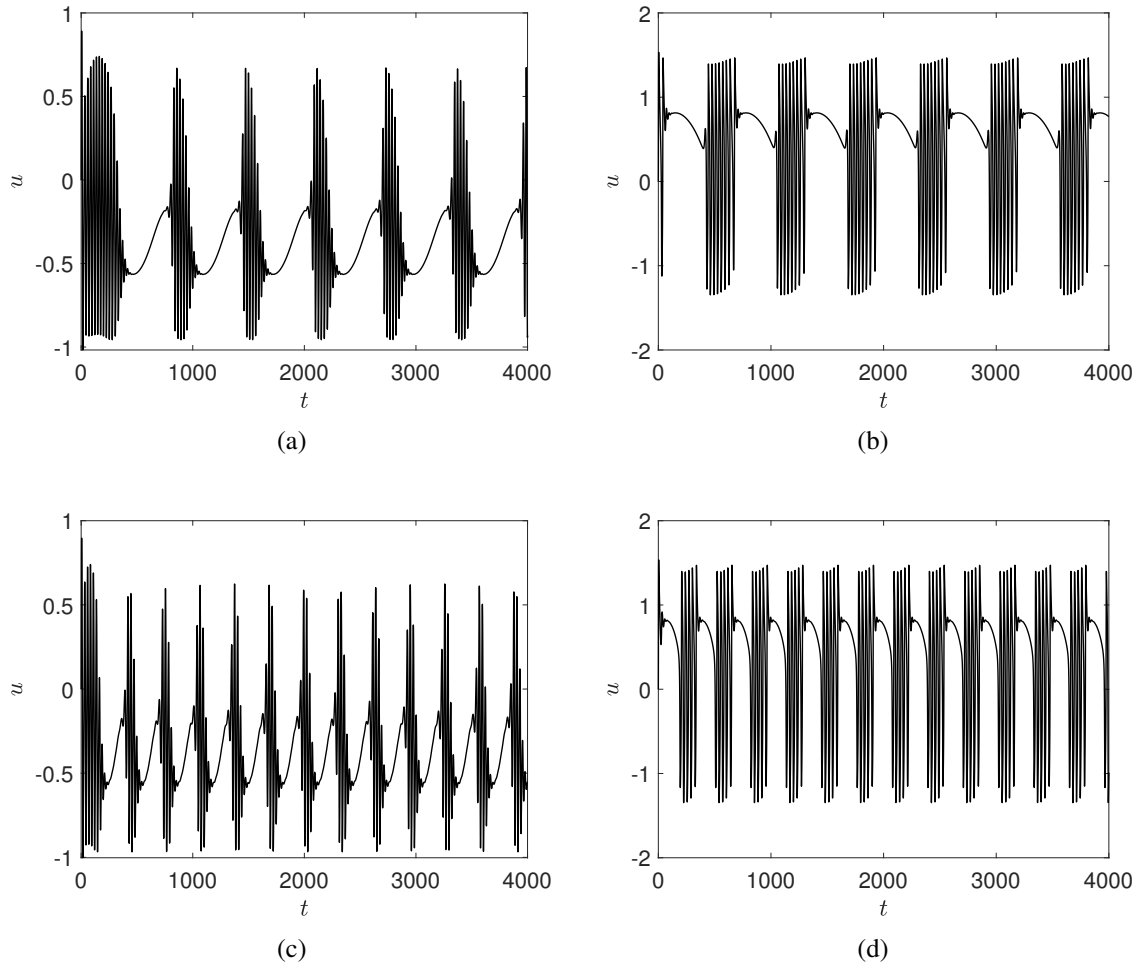

Figure 3.28 Two types of bursting mechanisms of system (2.12) for periodic photocurrents : Hopf-Hopf (left column) and SubHopf-Fold bursting (right column) with (a) $u_s = 0.3 + 0.1\sin 0.01t$, $\xi = 0.7$, (b) with $u_s = 0.6 + 0.1\sin 0.01t$, $\xi = 0.4$, (c) $u_s = 0.3 + 0.1\sin 0.02t$, $\xi = 0.7$, and (d) $u_s = 0.6 + 0.1\sin 0.02t$, $\xi = 0.4$.

spike synchronization may occur only if the frequencies of the two oscillators are very close. For excitatory (resp. inhibitory) coupling, the predominant mode of spike synchronization is in-phase (anti-phase). On the other hand, burst synchronization depends on whether the intrinsic oscillator is a resonator or integrator. The former may experience burst synchronization independent sign of the synapse while the latter may synchronize only for excitatory coupling [29]. Another feature common to elliptic bursters is their ability to experience instantaneous burst synchronization due to the slow passage effect[166].

Let us first consider synchronization between two photosensitive elliptic bursters coupled via gap junctions:

$$\begin{aligned} \tau\ddot{u}+\dot{u}_i &= u_i(1-\xi)-\frac{u_i^3}{3}-y_i+u_{s,i}+\alpha_{i,j}(u_j-u_i),\\ \dot{y}_i &= \varepsilon(x_i+a-by_i), \end{aligned} \tag{3.153}$$

where, $j=1,2$, and $\alpha_{i,j}$, represents the coupling between burster i and j, with $\alpha_{i,j}=\alpha_{j,i}$=$\alpha$, and $u_{s,i}=A_i\sin\omega_i t$. Different values of A, ω and initial conditions are chosen for the two neurons and the effect of α on the synchronization is studied. Furthermore, we define as error of synchronization the quantity:

$$e_s=\sqrt{(u_2-u_1)^2+(w_2-w_1)^2+(v_2-v_1)^2}. \tag{3.154}$$

Fig.3.29 shows the results of synchronization in the presence of gap coupling as a function of the coupling strength. It can be observed that as α increases so does the degree of burst and spike synchronization. Initial conditions used for the simulations were $(u_1,w_1,v_1,u_2,w_2,v_2)$=$(0,0.5,4,4,0,0)$ while other parameters were $u_{s1}=0.6+0.1\sin 0.01t$, $u_{s2}=0.6+0.2\sin 0.02t$, $\xi=0.4$, $\tau=0.1$, $a=0.7$, $\varepsilon=0.08$, and $b=1.5$. Burst synchronization appears almost instantaneously once the coupling is sufficiently strong and is accompanied by in-phase spike synchronization as expected. Furthermore, for moderate coupling strengths, the coupled system fires with a burst period greater than that of the uncoupled systems. Similar observations were made in coupled neurons [167]. At strong coupling strengths, synchronized bursts occur in two distinct phases.

Next we consider two bursters coupled via excitiatory or inhibitory synaptic coupling [168, 169] as follows

$$\begin{aligned} \dot{x}_i &= x_i(1-\xi)-\frac{x_i^3}{3}-y_i+u_{s,i}+s_{i,j}u_j,\\ \dot{y}_i &= \varepsilon(x_i+a-by_i). \end{aligned} \tag{3.155}$$

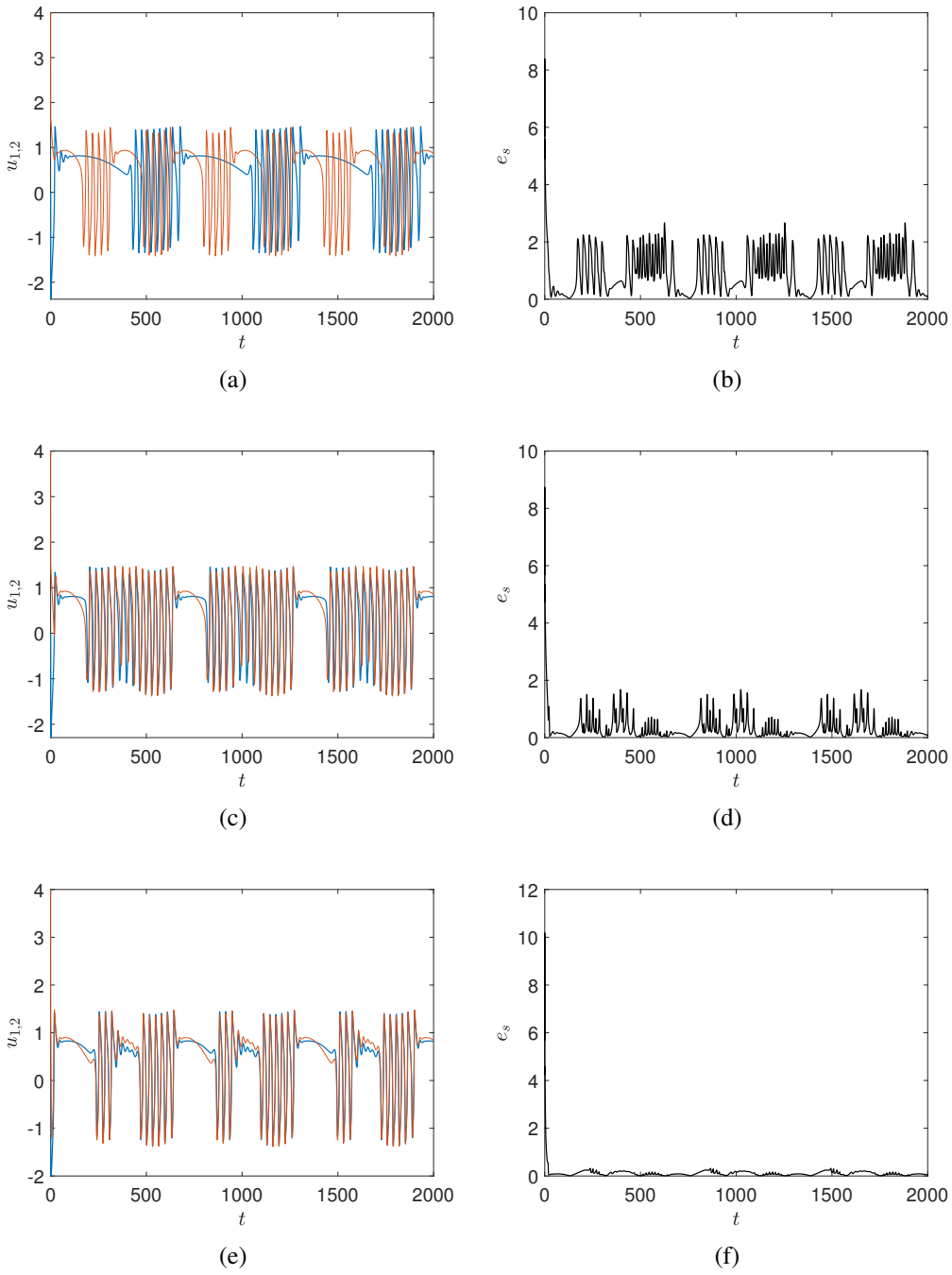

Figure 3.29 Evolution of synchronization (Left column) and error of synchronization (right column) of two elliptic photosensitive bursters (red and blue lines) coupled via electrical synapse as a function of coupling strength : (a) $\alpha = 0$, (b) $\alpha = 0.1$, and (c) $\alpha = 0.5$.

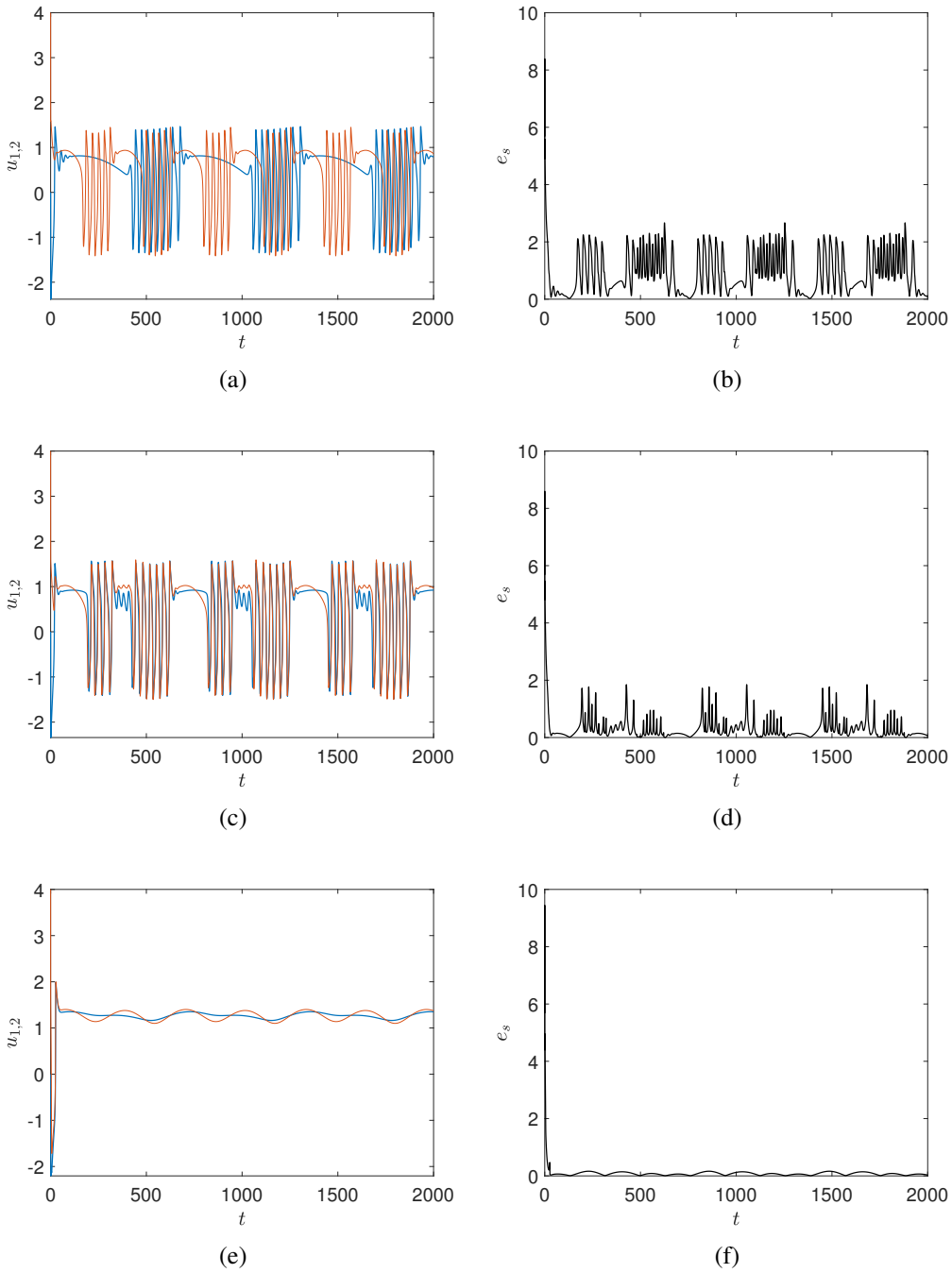

Figure 3.30 Evolution of synchronization (left column) and error of synchronization (right column) of two photosensitive bursters (red and blue lines) coupled via excitatory synapse as a function of coupling strength : (a) $s = 0$, (b) $s = 0.1$, and (c) $s = 0.5$.

where $j = 1,2$, and $s_{i,j}$ represents the sign and strength of the synaptic coupling. Here, we consider $s_{i,j} = s_{j,i} = s$. For excitatory (resp. inhibitory) coupling, $s > 0$ (resp. $s < 0$). Fig.3.30 and Fig.3.31 show synchronization between the neurons coupled respectively via excitatory and inhibitory coupling respectively. For Fig.3.30, initial conditions were $(u_1, w_1, v_1, u_2, w_2, v_2)$=$(0, 0.5, 4, 4, 0, 0)$ while system parameters were $u_{s1} = 0.6 + 0.1\sin 0.01t$, $u_{s2} = 0.6 + 0.2\sin 0.02t$, $\xi = 0.4$, $\tau = 0.1$, $a = 0.7$, $\varepsilon = 0.08$, and $b = 1.5$. For Fig.3.31,initial conditions were $(u_1, w_1, v_1, u_2, w_2, v_2)$=$(0, 0.5, 4, 4, 0, 0)$ while other parameters were $u_{s1} = 0.6 + 0.1\sin 0.01t$, $u_{s2} = 0.6 + 0.2\sin 0.02t$, $\xi = 0.4$, $\tau = 0.1$, $a = 0.7$, $\varepsilon = 0.08$, and $b = 1.5$. For excitatory coupling, moderately strong coupling is sufficient to achieve in-phase spike and burst synchronization while higher couplings result in amplitude death[170, 171]. Note that for this coupling strength, bursting occurs in two phases, similar to the case with gap junction coupling. When using an inhibitory coupling, moderate coupling strength yields anti-phase spike synchronization while destroying the bursts in both neurons. Higher inhibitory coupling strengths resulted in amplitude death, similar to excitatory coupling. The occurrence of amplitude death induced by coupling, among other factors, has been observed in other dynamical systems[172]. For example, Ozden et al.[173] studied coupling-induced amplitude death in a system of consisting of a biological neuron coupled to an electrical one. Generally speaking, amplitude death may provide a pathway through which unwanted oscillations, in this case bursting between neurons, may be terminated.

3.7 Conclusion

Generally speaking, models of nerve pulse propagation fall into two main categories: Those which try as much as possible to account for all main electrophysiological parameters and those which try to reduce the process to its essential features. The HH model leans towards the first category while the classical FHN falls into the second category. The hyperbolic FHN model on which the results presented in this chapter are based, takes the classical FHN a little step closer towards the first category by adding to it some details of physiological and physical relevance. It does so by realizing that finite speeds of propagation in a network of spatially coupled neurons, necessarily induces propagation delays. These delays vary with the length of the axon, the presence (lack) of myelination and the distance between the interacting units of a system [174]. These delays can be as small as a few milliseconds as well as over hundreds of milliseconds, and are especially relevant in non-local interactions. As such they can be regarded as a new bifurcation parameter which can significantly affect the dynamics of the system. Several approaches have been adopted to to model these delays: The adoption of a second temporal derivative which we have explored in

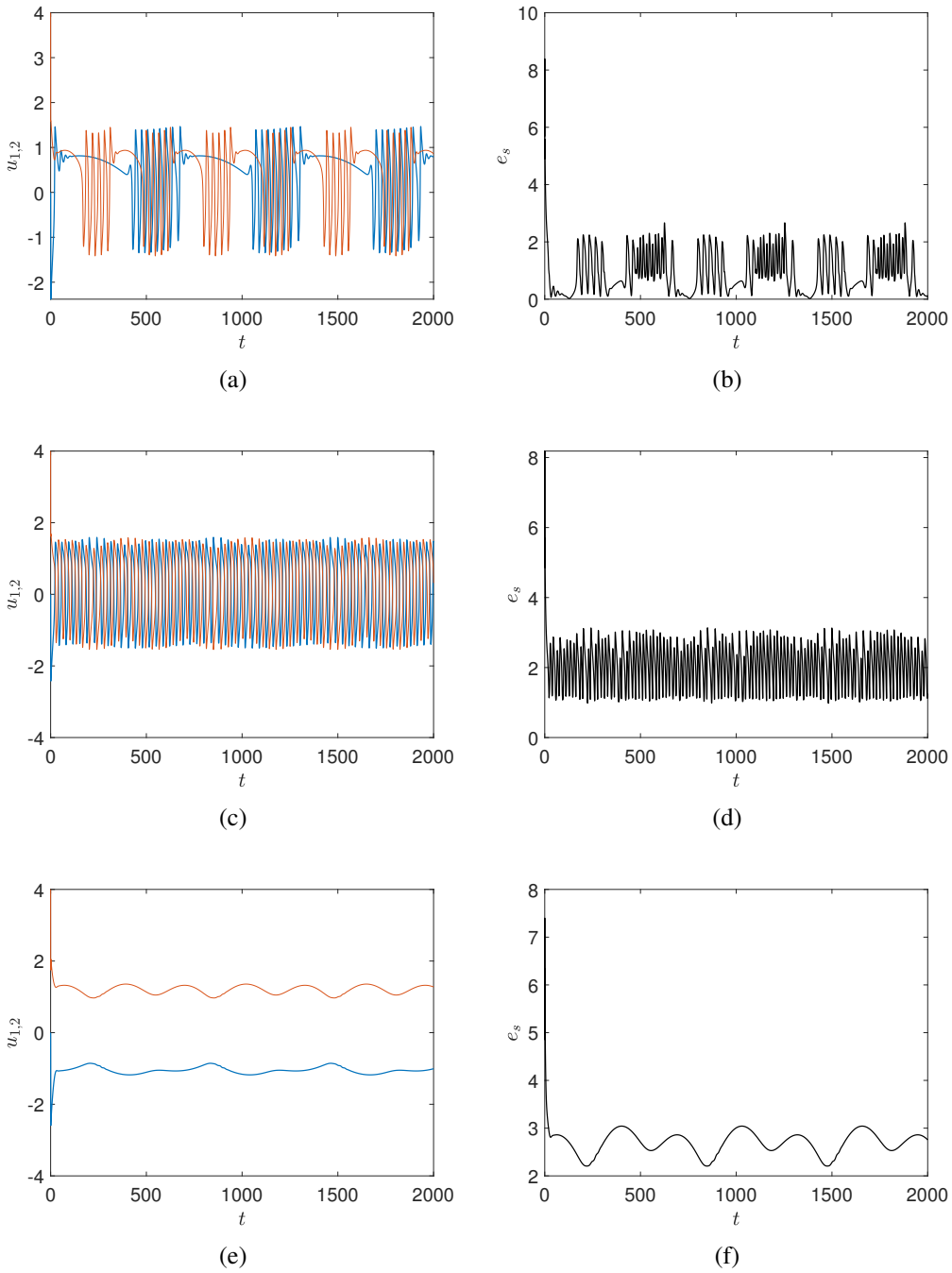

Figure 3.31 Evolution of synchronization (left column) and error of synchronization (right column) of two photosensitive bursters (red and blue lines) coupled via inhibitory synapse as a function of coupling strength : (a) $s = 0$, (b) $s = -0.1$, and (c) $s = -0.5$.

this thesis, the space dependent delays common in neural fields[175] as well as the addition of a constant delay[59].

By varying the relaxation time as the main bifurcation parameter, the results presented in this chapter have demonstrated the presence of Hopf bifurcations induced by the relaxation time, and pitchfork bifurcations, induced by negative diffusion. These bifurcations have been shown to not only exist for the continuous model but also for the corresponding discrete versions of the model. The Hopf bifurcations induced homogeneous oscillations in the absence of diffusion and traveling waves in the presence of diffusive effects. Having a structure similar to that of Maxwell's propagation of electromagnetic waves, the hyperbolic FHN supports damped traveling waves below the threshold and periodic waves at threshold of the relaxation time. For both types of waves the square of the wave speed varied inversely with the relaxation time.

Being a partial differential equation model and model in its own right, the hyperbolic FHN also possesses solitary wave solutions. Two of such solutions: the front wave and the oscillon have been constructed using analytical techniques. We showed that the amplitude of the front wave scales inversely with increases in relaxation time, contrary to that of the oscillon which increases with an increase in τ. Furthermore, these two waves admit a maximum speed corresponds to $\tau = 0$. We predict that this maximum speed correspond to the speed of the solitary waves in the classical FHN model.

By adjusting the intrinsic properties of the hyperbolic FHN photosensitive neuron and the properties of the photocurrent, we have established regions within codimension-two parameter space, corresponding to tonic spiking, quiescence, and bistability. We have, via the unfolding in the neighborhood of the Bautin bifurcation, explained the origin of bursting in the photosensitive neuron and have identified two possible modes of bursting. Focusing on elliptic bursting, we studied two coupled elliptic bursters under electrical and synaptic couplings of excitatory and inhibitory types. For electrical and excitatory coupling, spike and burst synchronization prevailed at moderately strong coupling. For both coupling schemes, an increase in coupling strength increased the bursting period, while synchronized bursting occurred in two distinct phases. When using an inhibitory coupling, moderately strong coupling destroyed bursting while maintaining anti-phase synchronized spiking. For both excitatory and inhibitory couplings, higher values of coupling strengths led to amplitude death.

General conclusion and outlook

General conclusion

In this thesis we have addressed the effect of the time of relaxation or delay due to finite speed effect, on time-periodic oscillations and traveling waves of a hyperbolic FHN model. Different bifurcations and their implications have been explored. Various critical values and parameter ranges over which these bifurcations may be observed have been calculated. To establish the nature of these bifurcations and other useful information in the neighborhood of local bifurcations, we made extensive use of the center manifold theory, normal form analysis, and other dimensional reduction techniques. We have shown that for small values of the relaxation time the hyperbolic FHN model behaves very much like the classical FHN model, conserving most of its essential bifurcations. However, new and interesting dynamics are observable at large values of this delay. We have also made use of the hyperbolic model to study the origin of bursting and synchronization in a hyperbolic photosensitive FHN neuron.

In Chapter 1, we reviewed the properties of the neuron concerning its function in generating and propagating action potentials. This was followed by a brief review of neural coupling and coupling schemes in biological neurons. Following, was a review of two members of the family of conductance-based models: the classical HH model and its lower-dimensional counterpart— the FHN model. After a review of the essential features of the latter, we discussed briefly, classical methods in modeling delays in coupled neurons followed by a review of delays due to the finite speed of propagation due to Cattaneo and its consequences. We concluded that chapter by reviewing the topological properties of the Hopf, pitchfork, fold, Bautin bifurcations, and many other relevant codimension-one and -two bifurcations. Detailed analysis of the Bautin bifurcation and the types of bursting dynamics around such points was conducted.

In Chapter 2, we present a review and brief description of the models and methods used throughout this thesis. The hyperbolic FHN model and its photosensitive variant are presented in the early sections of the chapter. This is followed by a review of the analytical and numerical methods relevant to this thesis. Under analytical methods, we reviewed the

center manifold theory (a keystone method to this thesis), normal form reductions, multiple-scale reductions, and methods for exact solitary wave solutions such as the $G'/G-$ expansion and the direct integration method. Under numerical methods, we reviewed the method of finite differences and its application to the discretization of the hyperbolic FHN models.

In Chapter 3, we present the main findings of this thesis in four different parts. In the first part of the results (sections 3.2 and 3.3), we demonstrated the existence of nonlinear oscillations in the hyperbolic FHN model, emerging from Hopf bifurcations when the relaxation constant, exceeds a certain threshold. For each Hopf bifurcation of a specific wavenumber (k), we computed the direction of the Hopf bifurcation also known as the first Lyapunov coefficient. We demonstrated that the dominant mode at the Hopf bifurcation is the mode $k = 0$ which is stable against long-wave side-band instability. By varying the relaxation time with the external stimulation current, we constructed the codimension-two bifurcation diagram for the hyperbolic system showing regions of spiking of multiple periods (periods-one, -two, three, and -four.), bursting, chaotic motion, and even post-inhibitory spiking. Below the threshold, we showed that the hyperbolic model behaves similarly to the classical FHN model. For periodic waves ($k > 0$), we demonstrate that the square of the wave speed is inversely proportional to the relaxation time. The wave speed is shown to be unbounded in the limit $\tau \to 0$, in good agreement with our expectations and theoretical predictions. We also showed that pitchfork bifurcations lead to time stationary instabilities, induced by a negative diffusion constant, and independent of the relaxation time. In the second part of our results (Section 3.4) dedicated to the numerical bifurcation analysis of the discrete versions of the hyperbolic FHN model, we show that the dynamics of the continuous models are preserved by their discrete counterparts. Thus, we can generalize the results obtained with the continuous models to the corresponding discrete models. Part three of our results (Section 3.5) is dedicated to the analysis of the front and oscillon solutions of the hyperbolic FHN model. We showed that the wave speed of fronts and oscillons generally increases as $\tau \to 0$ but stays finite at $\tau = 0$, corresponding to the maximum speed of the solitary waves. Furthermore, we showed that the amplitude of the front wave scales inversely with the relaxation time contrary to that of the oscillon wave which varies directly with relaxation time. In the fourth and last part of our results (Section 3.6), we discussed the hyperbolic photosensitive FHN in the context of bursting and burst synchronization built around a Bautin bifurcation (elliptic bursting). We showed that at higher values of the relaxation time, elliptic bursting may be destroyed under certain parameter ranges. Furthermore, when considering gap junction coupling between two elliptic bursters, we observed that an increase in coupling strength favors stronger burst and spike synchronization. However, for excitatory

and inhibitory coupling, although synchronization may be achieved for moderate coupling strengths, bursting and spiking may be destroyed at higher values of the coupling strengths.

In summary, our study has shown that the addition of the relaxation time, may lead to periodic waves, which propagate at finite speeds. The addition of this term does not significantly change the dynamics of the classical FHN model, provided that this delay does not exceed some critical values which we have established via various analytical and numerical techniques. Below criticality, only damped periodic waves are observed as expected due to the hyperbolic nature of the modified model. Beyond critical values of the relaxation time, oscillatory waves may propagate and new dynamics may be observed. For example, higher values of this time may affect the occurrence of elliptic bursting in the neuron. The qualitative and quantitative nature of the delay-induced bifurcations is preserved by the corresponding discrete models. For soliton propagation (fronts and oscillons), a maximum speed exists for which such waves may be observed—in good agreement with results reported in recent similar studies.

We summarized some noteworthy similarities and differences between the hyperbolic and classical FHN models in Table (3.2).

Outlook

The results presented in this thesis provide a sufficient overview of the dynamics of the hyperbolic FHN and the effect of the relaxation time on the dynamics of the waves propagating on the system. These results also demonstrate that the relaxation time can have an impact on other variants of the hyperbolic FHN model. An example of such an impact was observed in section 3.6 when using a photosensitive variant. These results are by no means exhaustive in the sense that other studies relevant to the hyperbolic model could be conducted as extensions of these results. To name a few possibilities:

In this study, we have not explored the effect of noise on the stability of synchrony and burst synchrony in a network of more than two neurons. We predict that noise will reduce the slow passage effect as noted in [77]. As such, burst synchronization may no longer be instantaneous once the coupling is sufficiently strong. The simulations above have considered coupled neurons driven by different photocurrents with different intensities and frequencies. Under such conditions, synchronization still prevailed under moderate to strong coupling. Thus we can expect that for neurons driven by nearly identical photocurrents, synchronization may be possible at much lower coupling strengths. Furthermore, most of the results obtained here may carry over to large networks of coupled bursters with nearest neighbor diffusive coupling and elliptic bursters built around a global Bautin point.

Property/attribute	Classical FHN	Modified FHN
Model description/control parameters.	Two dimensional parabolic ODE/ four control parameters.	Two dimensional hyperbolic system/ five control parameters.
Recovery variable	Not considered as an internal variable.	Considered as an internal variable with memory effects.
Velocity of wave system	Assumes infinite velocity without delay.	Velocity is finite with delay.
Waves at non-oscillatory points	Does not support waves at non-oscillatory points.	Supports damped waves at non-oscillatory points.
Frequency of oscillations	Frequency does not depend on τ.	Frequency depends on τ .
Hopf bifurcations	Subcritical and superciritcal	supercritical and subcritical Hopf
Nature of Canard explosions	Subcritical	Subcritical

Table 3.2 Some noteworthy comparisons of the modified model and the classical model based on a few attributes.

Another way in which these results could be extended is by considering the control of the oscillations induced by τ, using an external periodic signal. This could be achieved by applying methods such as frequency response and Arnold-tongues at the threshold of the parameter τ. The control of unwanted oscillations in neurons is a technique frequently used for example in the treatment of epilepsy.

Bibliography

[1] S. A. Campbell. Time delays in neural systems. In *Handbook of brain connectivity*, pages 65–90. Springer, 2007.

[2] J. Milton, J. L. Cabrera, T. Ohira, S. Tajima, Y. Tonosaki, C. W. Eurich, and S. A. Campbell. The time-delayed inverted pendulum: implications for human balance control. *Chaos: An Interdisciplinary Journal of Nonlinear Science*, 19(2):026110, 2009.

[3] S. G. Waxman. Axonal conduction and injury in multiple sclerosis: the role of sodium channels. *Nature Reviews Neuroscience*, 7(12):932–941, 2006.

[4] G. G. Gregoriou, S. J. Gotts, H. Zhou, and R. Desimone. High-frequency, long-range coupling between prefrontal and visual cortex during attention. *science*, 324(5931): 1207–1210, 2009.

[5] F. M. Atay and A. Hutt. Neural fields with distributed transmission speeds and long-range feedback delays. *SIAM Journal on Applied Dynamical Systems*, 5(4):670–698, 2006.

[6] A. S. Etémé, C. B. Tabi, and A. Mohamadou. Long-range patterns in hindmarsh–rose networks. *Communications in Nonlinear Science and Numerical Simulation*, 43: 211–219, 2017.

[7] P. Dayan and L. F. Abbott. *Theoretical neuroscience: computational and mathematical modeling of neural systems*. Computational Neuroscience Series, 2001.

[8] J. Wu, S. A. Campbell, and J. Bélair. *Time-Delayed Neural Networks: Stability and Oscillations*, pages 1–8. Springer New York, New York, NY, 2013. doi: 10.1007/978-1-4614-7320-6_513-1.

[9] M. Madadi Asl, A. Valizadeh, and P. A. Tass. Dendritic and axonal propagation delays may shape neuronal networks with plastic synapses. *Frontiers in Physiology*, 9:1849, 2018.

[10] J. K. Hale and S. M. V. Lunel. *Introduction to functional differential equations*, volume 99. Springer Science & Business Media, 2013.

[11] S. Das and A. Chatterjee. Multiple scales without center manifold reductions for delay differential equations near hopf bifurcations. *Nonlinear Dynamics*, 30(4):323–335, 2002.

[12] T. Erneux. *Applied delay differential equations*, volume 3. Springer Science & Business Media, 2009.

[13] T. Faria and L. T. Magalhães. Normal forms for retarded functional differential equations with parameters and applications to hopf bifurcation. *Journal of differential equations*, 122(2):181–200, 1995.

[14] A. Vanderbauwhede and G. Iooss. Center manifold theory in infinite dimensions. In *Dynamics reported*, pages 125–163. Springer, 1992.

[15] M. Haragus and G. Iooss. *Local bifurcations, center manifolds, and normal forms in infinite-dimensional dynamical systems*. Springer Science & Business Media, 2010.

[16] R. E. Plant. A fitzhugh differential-difference equation modeling recurrent neural feedback. *SIAM Journal on applied mathematics*, 40(1):150–162, 1981.

[17] J. Jia, H. Liu, C. Xu, and F. Yan. Dynamic effects of time delay on a coupled fitzhugh–nagumo neural system. *Alexandria Engineering Journal*, 54(2):241–250, 2015.

[18] J. Bélair, S. A. Campbell, and P. van den Driessche. Frustration, stability, and delay-induced oscillations in a neural network model. *SIAM Journal on Applied Mathematics*, 56(1):245–255, 1996.

[19] N. Bessonov, A. Beuter, S. Trofimchuk, and V. Volpert. Dynamics of periodic waves in a neural field model. *Mathematics*, 8(7):1076, 2020.

[20] R. Spigler. More around cattaneo equation to describe heat transfer processes. *Mathematical Methods in the Applied Sciences*, 43(9):5953–5962, 2020.

[21] G. Maugin and J. Engelbrecht. A thermodynamical viewpoint on nerve pulse dynamics. *Journal of Non-Equilibrium Thermodynamics*, 19(1):9–23, 1994.

[22] W. Likus and V. A. Vladimirov. Solitary waves in the model of active media, taking into account effects of relaxation. *Reports on Mathematical Physics*, 75(2):213–230, 2015.

[23] A. Gawlik, V. Vladimirov, and S. Skurativskyi. Existence of the solitary wave solutions supported by the modified fitzhugh–nagumo system. *Nonlinear Analysis: Modelling and Control*, 25(3):482–501, 2020.

[24] A. Gawlik, V. Vladimirov, and S. Skurativskyi. Solitary wave dynamics governed by the modified fitzhugh–nagumo equation. *Journal of Computational and Nonlinear Dynamics*, 15(6), 2020.

[25] A. Hodgkin and A. Huxley. A quantitative description of membrane current and its application to conduction and excitation in nerve. *Bulletin of mathematical biology*, 52(1-2):25–71, 1990.

[26] E. M. Izhikevich. Simple model of spiking neurons. *IEEE Transactions on neural networks*, 14(6):1569–1572, 2003.

[27] E. M. Izhikevich. Resonate-and-fire neurons. *Neural networks*, 14(6-7):883–894, 2001.

[28] J. Baladron, D. Fasoli, O. Faugeras, and J. Touboul. Mean-field description and propagation of chaos in networks of hodgkin-huxley and fitzhugh-nagumo neurons. *The Journal of Mathematical Neuroscience*, 2(1):1–50, 2012.

[29] E. M. Izhikevich. Neural excitability, spiking and bursting. *International journal of bifurcation and chaos*, 10(06):1171–1266, 2000.

[30] P. E. Greenwood and L. M. Ward. *Stochastic neuron models*, volume 1. Springer, 2016.

[31] B. Lindner and L. Schimansky-Geier. Analytical approach to the stochastic fitzhugh-nagumo system and coherence resonance. *Physical review E*, 60(6):7270, 1999.

[32] B. A. Guimfack, C. B. Tabi, A. Mohamadou, and T. C. Kofané. Stochastic dynamics of the fitzhugh-nagumo neuron model through a modified van der pol equation with fractional-order term and gaussian white noise excitation. *Discrete & Continuous Dynamical Systems-S*, page 0, 2018.

[33] J. Wei and S. Ruan. Stability and bifurcation in a neural network model with two delays. *Physica D: Nonlinear Phenomena*, 130(3-4):255–272, 1999.

[34] D. Fan and L. Hong. Hopf bifurcation analysis in a synaptically coupled fhn neuron model with delays. *Communications in Nonlinear Science and Numerical Simulation*, 15(7):1873–1886, 2010.

[35] M. C. Cross and P. C. Hohenberg. Pattern formation outside of equilibrium. *Reviews of modern physics*, 65(3):851, 1993.

[36] Y. Kuramoto. *Chemical oscillations, waves, and turbulence*. Courier Corporation, 2003.

[37] C. Börgers. *An introduction to modeling neuronal dynamics*, volume 66. Springer, 2017.

[38] F. Zeldenrust, W. J. Wadman, and B. Englitz. Neural coding with bursts—current state and future perspectives. *Frontiers in computational neuroscience*, 12:48, 2018.

[39] J. Huguenard. Low-threshold calcium currents in central nervous system neurons. *Annual review of physiology*, 58(1):329–348, 1996.

[40] M. S. Cembrowski, S. M. Logan, M. Tian, L. Jia, W. Li, W. L. Kath, H. Riecke, and J. H. Singer. The mechanisms of repetitive spike generation in an axonless retinal interneuron. *Cell reports*, 1(2):155–166, 2012.

[41] J. L. Hindmarsh and R. Rose. A model of neuronal bursting using three coupled first order differential equations. *Proceedings of the Royal society of London. Series B. Biological sciences*, 221(1222):87–102, 1984.

[42] C. A. Del Negro, C.-F. Hsiao, S. H. Chandler, and A. Garfinkel. Evidence for a novel bursting mechanism in rodent trigeminal neurons. *Biophysical journal*, 75(1):174–182, 1998.

[43] J. Guckenheimer and Y. A. Kuznetsov. Bautin bifurcation. *Scholarpedia*, 2(5):1853, 2007.

[44] J. P. Keener and J. Sneyd. *Mathematical physiology*, volume 1. Springer, 1998.

[45] R. J. Butera Jr, J. Rinzel, and J. C. Smith. Models of respiratory rhythm generation in the pre-botzinger complex. i. bursting pacemaker neurons. *Journal of neurophysiology*, 82(1):382–397, 1999.

[46] R. FitzHugh. Impulses and physiological states in theoretical models of nerve membrane. *Biophysical journal*, 1(6):445–466, 1961.

[47] C. Rocsoreanu, A. Georgescu, and N. Giurgiteanu. *The FitzHugh-Nagumo model: bifurcation and dynamics*, volume 10. Springer Science & Business Media, 2012.

[48] E. M. Izhikevich and R. FitzHugh. Fitzhugh-nagumo model. *Scholarpedia*, 1(9):1349, 2006.

[49] T. Kanamaru. Van der pol oscillator. *Scholarpedia*, 2(1):2202, 2007.

[50] V. Volterra. Sur la théorie mathématique des phénomenes héréditaires. *Journal de mathématiques pures et appliquées*, 7:249–298, 1928.

[51] O. J. Smith. Feedback control systems. 1958.

[52] D. Beamish, S. Bhatti, J. Wu, and Z. Jing. Performance limitations from delay in human and mechanical motor control. *Biological cybernetics*, 99(1):43–61, 2008.

[53] S. A. Campbell, I. Ncube, and J. Wu. Multistability and stable asynchronous periodic oscillations in a multiple-delayed neural system. *Physica D: Nonlinear Phenomena*, 214(2):101–119, 2006.

[54] C. Cattaneo. A form of heat-conduction equations which eliminates the paradox of instantaneous propagation. *Comptes Rendus*, 247:431, 1958.

[55] A. Compte and R. Metzler. The generalized cattaneo equation for the description of anomalous transport processes. *Journal of Physics A: Mathematical and General*, 30 (21):7277, 1997.

[56] K. D. Lewandowska and T. Kosztołowicz. Application of generalized cattaneo equation to model subdiffusion impedance. *Acta Physica Polonica B*, 39(5), 2008.

[57] A. Hutt, M. Bestehorn, and T. Wennekers. Pattern formation in intracortical neuronal fields. *Network: Computation in Neural Systems*, 14(2):351–368, 2003.

[58] P. C. Bressloff. Spatiotemporal dynamics of continuum neural fields. *Journal of Physics A: Mathematical and Theoretical*, 45(3):033001, 2011.

[59] L. Glass and M. C. Mackey. *From clocks to chaos: The rhythms of life*. Princeton University Press, 1988.

[60] D. Jou, J. Casas-Vázquez, and G. Lebon. Extended irreversible thermodynamics. In *Extended Irreversible Thermodynamics*, pages 41–74. Springer, 1996.

[61] C. L. McTaggart and K. Lindsay. Nonclassical effects in the bénard problem. *SIAM Journal on Applied Mathematics*, 45(1):70–92, 1985.

[62] M. Zakari and D. Jou. Equations of state and transport equations in viscous cosmological models. *Physical Review D*, 48(4):1597, 1993.

[63] T. Ruggeri, A. Muracchini, and L. Seccia. Shock waves and second sound in a rigid heat conductor: A critical temperature for naf and bi. *Physical review letters*, 64(22): 2640, 1990.

[64] T. Insperger and G. Stépán. Semi-discretization method for delayed systems. *International Journal for numerical methods in engineering*, 55(5):503–518, 2002.

[65] T. Dong, W. Xu, and X. Liao. Hopf bifurcation analysis of reaction–diffusion neural oscillator system with excitatory-to-inhibitory connection and time delay. *Nonlinear Dynamics*, 89(4):2329–2345, 2017.

[66] X.-P. Yan and C.-H. Zhang. Hopf bifurcation in a delayed lokta–volterra predator–prey system. *Nonlinear Analysis: Real World Applications*, 9(1):114–127, 2008.

[67] E. Niebur. Neuronal cable theory. *Scholarpedia*, 3(5):2674, 2008.

[68] W. Kaminski. Hyperbolic heat conduction equation for materials with a nonhomogeneous inner structure. 1990.

[69] S. G. Krantz and H. R. Parks. *The implicit function theorem: history, theory, and applications*. Springer Science & Business Media, 2012.

[70] A. Andronov and E. Leontovich. Some cases of dependence of limit cycles on a parameter. *Uchenye zapiski Gorkovskogo Universiteta*, 6:3–24, 1937.

[71] E. Hopf. Abzweigung einer periodischen lösung von einer stationären lösung eines differentialsystems. *Ber. Math.-Phys. Kl Sächs. Akad. Wiss. Leipzig*, 94:1–22, 1942.

[72] V. García-Morales and K. Krischer. The complex ginzburg–landau equation: an introduction. *Contemporary Physics*, 53(2):79–95, 2012.

[73] G. Iooss and A. Mielke. Time-periodic ginzburg-landau equations for one dimensional patterns with large wave length. *Zeitschrift für angewandte Mathematik und Physik ZAMP*, 43(1):125–138, 1992.

[74] Y. A. Kuznetsov. *Elements of applied bifurcation theory*, volume 112. Springer Science & Business Media, 2013.

[75] Z. Song and J. Xu. Bursting near bautin bifurcation in a neural network with delay coupling. *International Journal of Neural Systems*, 19(05):359–373, 2009.

[76] E. M. Izhikevich. Synchronization of elliptic bursters. *SIAM review*, 43(2):315–344, 2001.

[77] A. K. a. Azad and P. Ashwin. Within-burst synchrony changes for coupled elliptic bursters. *SIAM Journal on Applied Dynamical Systems*, 9(1):261–281, 2010.

[78] Y. A. Kuznetsov and H. G. Meijer. *Numerical bifurcation analysis of maps: from theory to software*, volume 34. Cambridge University Press, 2019.

[79] P. Anderson and G. O. Mackie. Electrically coupled, photosensitive neurons control swimming in a jellyfish. *Science*, 197(4299):186–188, 1977.

[80] T. H. Nelson, Y. I. Kim, and M. Kim. Photosensitivity of a bursting pacemaker neuron inaplysia californica. *Brain research*, 105(3):583–587, 1976.

[81] Y. Liu, W.-j. Xu, J. Ma, F. Alzahrani, and A. Hobiny. A new photosensitive neuron model and its dynamics. *Frontiers of Information Technology & Electronic Engineering*, 21:1387–1396, 2020.

[82] P. Agostini and G. Petite. Photoelectric effect under strong irradiation. *Contemporary physics*, 29(1):57–77, 1988.

[83] D. Brust. Band-theoretic model for the photoelectric effect in silicon. *Physical Review*, 139(2A):A489, 1965.

[84] J. Guckenheimer and P. Holmes. *Nonlinear oscillations, dynamical systems, and bifurcations of vector fields*, volume 42. Springer Science & Business Media, 2013.

[85] Z. Mei. *Numerical bifurcation analysis for reaction-diffusion equations*, volume 28. Springer Science & Business Media, 2013.

[86] S. Wiggins. *Introduction to applied nonlinear dynamical systems and chaos*, volume 2. Springer Science & Business Media, 2003.

[87] J. Carr. Center manifold. *Scholarpedia*, 1(12):1826, 2006.

[88] J. Carr. *Applications of centre manifold theory*, volume 35. Springer Science & Business Media, 2012.

[89] A. Kelley. Stability of the center-stable manifold. *Journal of Mathematical Analysis and Applications*, 18(2):336–344, 1967.

[90] P. G. Drazin and R. S. Johnson. *Solitons: an introduction*, volume 2. Cambridge university press, 1989.

[91] J. Zhang, X. Wei, and Y. Lu. A generalized (g'/g)-expansion method and its applications. *Physics Letters A*, 372(20):3653–3658, 2008.

[92] M. Wang, X. Li, and J. Zhang. The (g'/g)-expansion method and travelling wave solutions of nonlinear evolution equations in mathematical physics. *Physics Letters A*, 372(4):417–423, 2008.

[93] G. Griffiths and W. E. Schiesser. *Traveling wave analysis of partial differential equations: numerical and analytical methods with MATLAB and Maple*. Academic Press, 2010.

[94] J. Hietarinta. Introduction to the hirota bilinear method. In *Integrability of nonlinear systems*, pages 95–103. Springer, 1997.

[95] W. E. Schiesser and G. W. Griffiths. *A compendium of partial differential equation models: method of lines analysis with Matlab*. Cambridge University Press, 2009.

[96] A. Shabat and V. Zakharov. Exact theory of two-dimensional self-focusing and one-dimensional self-modulation of waves in nonlinear media. *Soviet physics JETP*, 34(1): 62, 1972.

[97] H. Leblond. The reductive perturbation method and some of its applications. *Journal of Physics B: Atomic, Molecular and Optical Physics*, 41(4):043001, 2008.

[98] C. B. Tabi, A. S. Etémé, and A. Mohamadou. Frequency mode excitations in two-dimensional hindmarsh–rose neural networks. *Physica A: Statistical Mechanics and its Applications*, 474:186–198, 2017.

[99] F. M. Kakmeni, E. M. Inack, and E. Yamakou. Localized nonlinear excitations in diffusive hindmarsh-rose neural networks. *Physical Review E*, 89(5):052919, 2014.

[100] C. B. Tabi, A. S. Etémé, A. Mohamadou, and T. Kofané. Unstable discrete modes in hindmarsh–rose neural networks under magnetic flow effect. *Chaos Solit. Fract.*, 123: 116–123, 2019.

[101] L.-A. Ranvier. Lecons sur l'histologie du systeme nerveux, par ml ranvier, recueillies par m. *Weber. F. Savy, Paris*, 1878.

[102] H. J. Hupkes and B. Sandstede. Traveling pulse solutions for the discrete fitzhugh–nagumo system. *SIAM Journal on Applied Dynamical Systems*, 9(3):827–882, 2010.

[103] C. E. Elmer and E. S. Van Vleck. Spatially discrete fitzhugh–nagumo equations. *SIAM Journal on Applied Mathematics*, 65(4):1153–1174, 2005.

[104] J. Foweraker, D. Brown, and R. Marrs. Discrete-time stimulation of the oscillatory and excitable forms of a fitzhugh–nagumo model applied to the pulsatile release of luteinizing hormone releasing hormone. *Chaos: An Interdisciplinary Journal of Nonlinear Science*, 5(1):200–208, 1995.

[105] E. J. Doedel. Auto: A program for the automatic bifurcation analysis of autonomous systems. *Congr. Numer*, 30(265-284):25–93, 1981.

[106] A. Dhooge, W. Govaerts, and Y. A. Kuznetsov. Matcont: a matlab package for numerical bifurcation analysis of odes. *ACM Transactions on Mathematical Software (TOMS)*, 29(2):141–164, 2003.

[107] H. Uecker, D. Wetzel, and J. D. Rademacher. pde2path-a matlab package for continuation and bifurcation in 2d elliptic systems. *Numerical Mathematics: Theory, Methods and Applications*, 7(1):58–106, 2014.

[108] Q. Din, S. Khaliq, and P. Rawalakot. Flip and hopf bifurcations of discrete-time fitzhugh–nagumo model. *Open J. Math. Sci.*, 2(1):209–220, 2018.

[109] A. Weber et al. Deciding hopf bifurcations by quantifier elimination in a software-component architecture. *Journal of Symbolic Computation*, 30(2):161–179, 2000.

[110] S. Mazumder. *Numerical methods for partial differential equations: finite difference and finite volume methods*. Academic Press, 2015.

[111] J. E. Marsden and M. McCracken. *The Hopf bifurcation and its applications*, volume 19. Springer Science & Business Media, 2012.

[112] B. D. Hassard, B. Hassard, N. D. Kazarinoff, Y.-H. Wan, and Y. W. Wan. *Theory and applications of Hopf bifurcation*, volume 41. CUP Archive, 1981.

[113] R. FitzHugh. Mathematical models of threshold phenomena in the nerve membrane. *The bulletin of mathematical biophysics*, 17(4):257–278, 1955.

[114] R. R. Llinás. The intrinsic electrophysiological properties of mammalian neurons: insights into central nervous system function. *Science*, 242(4886):1654–1664, 1988.

[115] M. Wechselberger. Canards. *Scholarpedia*, 2(4):1356, 2007.

[116] M. Feingold, D. L. Gonzalez, O. Piro, and H. Viturro. Phase locking, period doubling, and chaotic phenomena in externally driven excitable systems. *Physical Review A*, 37 (10):4060, 1988.

[117] Y. Horikawa. Period-doubling bifurcations and chaos in the decremental propagation of a spike train in excitable media. *Physical Review E*, 50(2):1708, 1994.

[118] J. Wright and R. Kydd. The electroencephalogram and cortical neural networks. *Network: Computation in Neural Systems*, 3(3):341–362, 1992.

[119] P. L. Nunez and B. A. Cutillo. *Neocortical dynamics and human EEG rhythms*. Oxford University Press, USA, 1995.

[120] J. D. Murray. *Mathematical biology: I. An introduction*, volume 17. Springer Science & Business Media, 2007.

[121] F. H. Busse. *Evolution of spontaneous structures in dissipative continuous systems*, volume 55. Springer Science & Business Media, 1998.

[122] C. B. Tabi, A. S. Etémé, and T. C. Kofané. Unstable cardiac multi-spiral waves in a fitzhugh–nagumo soliton model under magnetic flow effect. *Nonlinear Dynamics*, pages 1–16, 2020.

[123] A. Mvogo, C. N. Takembo, H. E. Fouda, and T. C. Kofané. Pattern formation in diffusive excitable systems under magnetic flow effects. *Physics Letters A*, 381(28): 2264–2271, 2017.

[124] C. N. Takembo and H. P. E. Fouda. Effect of temperature fluctuation on the localized pattern of action potential in cardiac tissue. *Scientific Reports*, 10(1):1–12, 2020.

[125] Q. Zheng and J. Shen. Pattern formation in the fitzhugh–nagumo model. *Computers & Mathematics with Applications*, 70(5):1082–1097, 2015.

[126] N. Iqbal, R. Wu, and B. Liu. Pattern formation by super-diffusion in fitzhugh–nagumo model. *Applied Mathematics and Computation*, 313:245–258, 2017.

[127] A. N. Landge, B. M. Jordan, X. Diego, and P. Müller. Pattern formation mechanisms of self-organizing reaction-diffusion systems. *Developmental Biology*, 460(1):2–11, 2020.

[128] Z. Jing, Y. Chang, and B. Guo. Bifurcation and chaos in discrete fitzhugh–nagumo system. *Chaos, Solitons & Fractals*, 21(3):701–720, 2004.

[129] E. Kwessi, S. Elaydi, B. Dennis, and G. Livadiotis. Nearly exact discretization of single species population models. *Natural Resource Modeling*, 31(4):e12167, 2018.

[130] E. Kwessi and L. J. Edwards. A nearly exact discretization scheme for the fitzhugh–nagumo model. *Differential Equations and Dynamical Systems*, pages 1–23, 2021.

[131] M. M. Islam and M. S. Hasan. A study on exact solution of the telegraph equation by (g/g)-expansion method. *African Journal of Mathematics and Computer Science Research*, 11(7):103–108, 2018.

[132] G. Ebadi and A. Biswas. Application of the g'/g-expansion method for nonlinear diffusion equations with nonlinear source. *Journal of the Franklin Institute*, 347(7): 1391–1398, 2010.

[133] S. K. Elagan, M. Sayed, and Y. S. Hamed. An innovative solutions for the generalized fitzhugh-nagumo equation by using the generalized...-expansion method. *Applied Mathematics*, 2(4):470, 2011.

[134] N. Akhmediev and A. Ankiewicz. *Dissipative solitons: from optics to biology and medicine*, volume 751. Springer Science & Business Media, 2008.

[135] V. K. Vanag and I. R. Epstein. Stationary and oscillatory localized patterns, and subcritical bifurcations. *Physical review letters*, 92(12):128301, 2004.

[136] Y. Liu, Y. Xu, and J. Ma. Synchronization and spatial patterns in a light-dependent neural network. *Communications in Nonlinear Science and Numerical Simulation*, 89: 105297, 2020.

[137] G. V. Osipov, J. Kurths, and C. Zhou. *Synchronization in oscillatory networks*. Springer Science & Business Media, 2007.

[138] A. S. Etémé, C. B. Tabi, and A. Mohamadou. Firing and synchronization modes in neural network under magnetic stimulation. *Communications in Nonlinear Science and Numerical Simulation*, 72:432–440, 2019.

[139] C. N. Takembo, A. Mvogo, H. P. E. Fouda, and T. C. Kofané. Effect of electromagnetic radiation on the dynamics of spatiotemporal patterns in memristor-based neuronal network. *Nonlinear Dynamics*, 95(2):1067–1078, 2019.

[140] B. Ermentrout and J. D. Drover. Nonlinear coupling near a degenerate hopf (bautin) bifurcation. *SIAM Journal On Applied Mathematics*, 63(5):1627–1647, 2003.

[141] J. Schwarz, G. Dangelmayr, A. Stevens, and K. Bräuer. Burst and spike synchronization of coupled neural oscillators. *Dynamical Systems*, 16(2):125–156, 2001.

[142] F. C. Hoppensteadt and E. M. Izhikevich. *Weakly connected neural networks*, volume 126. Springer Science & Business Media, 2012.

[143] E. N. Davison, Z. Aminzare, B. Dey, and N. Ehrich Leonard. Mixed mode oscillations and phase locking in coupled fitzhugh-nagumo model neurons. *Chaos: An Interdisciplinary Journal of Nonlinear Science*, 29(3):033105, 2019.

[144] P. Saha and S. H. Strogatz. The birth of period three. *Mathematics Magazine*, 68(1): 42–47, 1995.

[145] J. Bechhoefer. The birth of period 3, revisited. *Mathematics magazine*, 69(2):115–118, 1996.

[146] T. Insperger. On the approximation of delayed systems by taylor series expansion. *Journal of Computational and Nonlinear Dynamics*, 10(2), 2015.

[147] D. Desmaisons, J.-D. Vincent, and P.-M. Lledo. Control of action potential timing by intrinsic subthreshold oscillations in olfactory bulb output neurons. *Journal of Neuroscience*, 19(24):10727–10737, 1999.

[148] B. V-GHAFFARI, M. Kouhnavard, and T. Kitajima. Biophysical properties of subthreshold resonance oscillations and subthreshold membrane oscillations in neurons. *Journal of biological systems*, 24(04):561–575, 2016.

[149] M. M. Asl, A. Valizadeh, and P. A. Tass. Dendritic and axonal propagation delays determine emergent structures of neuronal networks with plastic synapses. *Scientific reports*, 7(1):1–12, 2017.

[150] G. Teschl. *Ordinary differential equations and dynamical systems*, volume 140. American Mathematical Soc., 2012.

[151] K. MacEwan and D. G. Leaist. Incongruent diffusion (negative main mutual diffusion coefficient) for a ternary mixed surfactant system. *The Journal of Physical Chemistry B*, 106(40):10296–10300, 2002.

[152] S. Emmanuel, A. Cortis, and B. Berkowitz. Diffusion in multicomponent systems: a free energy approach. *Chemical physics*, 302(1-3):21–30, 2004.

[153] E. L. Cussler. *Multicomponent diffusion*, volume 3. Elsevier, 2013.

[154] B. Ambrosio. Hopf bifurcation in an oscillatory-excitable reaction–diffusion model with spatial heterogeneity. *International Journal of Bifurcation and Chaos*, 27(05): 1750065, 2017.

[155] X.-P. Yan, Y.-J. Ding, and C.-H. Zhang. Dynamics analysis in a gierer–meinhardt reaction–diffusion model with homogeneous neumann boundary condition. *International Journal of Bifurcation and Chaos*, 29(09):1930025, 2019.

[156] D. Henry. *Geometric theory of semilinear parabolic equations*, volume 840. Springer, 2006.

[157] I. S. Aranson and L. Kramer. The world of the complex ginzburg-landau equation. *Reviews of modern physics*, 74(1):99, 2002.

[158] B. Matkowsky and V. A. Volpert. Stability of plane wave solutions of complex ginzburg-landau equations. *Quarterly of applied mathematics*, 51(2):265–281, 1993.

[159] M. Cross and H. Greenside. *Pattern formation and dynamics in nonequilibrium systems*. Cambridge University Press, 2009.

[160] B. Janiaud, A. Pumir, D. Bensimon, V. Croquette, H. Richter, and L. Kramer. The eckhaus instability for traveling waves. *Physica D: Nonlinear Phenomena*, 55(3-4): 269–286, 1992.

[161] S. Shwetanshumala. Temporal solitons of modified complex ginzberg landau equation. *Progress In Electromagnetics Research*, 3:17–24, 2008.

[162] K. Nozaki and N. Bekki. Exact solutions of the generalized ginzburg-landau equation. *Journal of the Physical Society of Japan*, 53(5):1581–1582, 1984.

[163] B. Ermentrout. Neural networks as spatio-temporal pattern-forming systems. *Reports on progress in physics*, 61(4):353, 1998.

[164] G. F. Achu, S. M. Tchouobiap, F. M. Kakmeni, and C. Tchawoua. Periodic soliton trains and informational code structures in an improved soliton model for biomembranes and nerves. *Physical Review E*, 98(2):022216, 2018.

[165] L. Yang, A. M. Zhabotinsky, and I. R. Epstein. Jumping solitary waves in an autonomous reaction–diffusion system with subcritical wave instability. *Physical Chemistry Chemical Physics*, 8(40):4647–4651, 2006.

[166] S. M. Baer, T. Erneux, and J. Rinzel. The slow passage through a hopf bifurcation: delay, memory effects, and resonance. *SIAM Journal on Applied mathematics*, 49(1): 55–71, 1989.

[167] A. Sherman and J. Rinzel. Rhythmogenic effects of weak electrotonic coupling in neuronal models. *Proceedings of the National Academy of Sciences*, 89(6):2471–2474, 1992.

[168] M. Masoliver and C. Masoller. Sub-threshold signal encoding in coupled fitzhugh-nagumo neurons. *Scientific reports*, 8(1):1–10, 2018.

[169] R. M. Amro, B. Lindner, and A. B. Neiman. Phase diffusion in unequally noisy coupled oscillators. *Physical review letters*, 115(3):034101, 2015.

[170] G. Saxena, A. Prasad, and R. Ramaswamy. Amplitude death: The emergence of stationarity in coupled nonlinear systems. *Physics Reports*, 521(5):205–228, 2012.

[171] K. Konishi. Amplitude death induced by dynamic coupling. *Physical Review E*, 68 (6):067202, 2003.

[172] R. E. Mirollo and S. H. Strogatz. Amplitude death in an array of limit-cycle oscillators. *Journal of Statistical Physics*, 60(1):245–262, 1990.

[173] I. Ozden, S. Venkataramani, M. Long, B. Connors, and A. Nurmikko. Strong coupling of nonlinear electronic and biological oscillators: Reaching the "amplitude death" regime. *Physical review letters*, 93(15):158102, 2004.

[174] H. A. Swadlow and S. G. Waxman. Axonal conduction delays. *Scholarpedia*, 7(6): 1451, 2012.

[175] A. Hutt. Generalization of the reaction-diffusion, swift-hohenberg, and kuramoto-sivashinsky equations and effects of finite propagation speeds. *Physical Review E*, 75 (2):026214, 2007.

List of publications

This work is supported by results originally documented in the following peer-reviewed publications:

— **Tah, Forwah Amstrong**, Conrad Bertrand Tabi, and Timoléon Crépin Kofané. "Hopf bifurcations on invariant manifolds of a modified Fitzhugh–Nagumo model." Nonlinear Dynamics 102, no. 1 (2020): 311-327.

— **Tah, Forwah Amstrong**, Conrad Bertrand Tabi, and Timoléon Crépin Kofané. "Pattern formation in the Fitzhugh–Nagumo neuron with diffusion relaxation." Chaos, Solitons & Fractals 147 (2021): 110974.

Appendix A

Nonlinear coefficients of the CGL

A.1 Derivation of coefficients of the CGL and solvability

Using Eq.(2.72), Eq.(2.3) can be transformed as

$$\Big(q+\frac{\partial y(z,\bar{z},\alpha,\mu^2)}{\partial z}\Big)\frac{\partial z}{\partial t}+\Big(\bar{q}+\frac{\partial y(z,\bar{z},\alpha,\mu^2)}{\partial \bar{z}}\Big)\frac{\partial \bar{z}}{\partial t}=(\mu^2\tilde{D}\Delta+\tilde{A})(zq+\bar{z}\bar{q}+y(z,\bar{z},\alpha,\mu^2))$$
$$+F(U_0+zq+\bar{z}\bar{q}+y(z,\bar{z},\alpha,\mu^2)) \tag{A.1}$$

Substituting Eq. (2.73) and the Taylor series expansion of $y(z,\bar{z},\alpha,\mu^2)$ about the point $(0,0,0,0)$ into Eq(A.1) and comparing terms of like order, we obtain:

$$\mathscr{O}(\alpha):\mathscr{L}y_{0010}=0. \tag{A.2}$$

$$\mathscr{O}(\alpha\mu^2):\mathscr{L}y_{0011}+\frac{\partial}{\partial\alpha}\tilde{D}\Big|_{\alpha=0}\Delta y_{0010}=0. \tag{A.3}$$

$$\mathscr{O}(z^2):(\mathscr{L}-2i\omega)y_{2000}=-\frac{1}{2}B(q,q). \tag{A.4}$$

$$\mathscr{O}(z\mu^2):(\mathscr{L}-i\omega)y_{1001}=(f_3-\tilde{D}|_{\alpha=0}\Delta)q. \tag{A.5}$$

$$\mathscr{O}(z\alpha):(\mathscr{L}-i\omega)y_{1010}=f_1q-B(q,y_{0010})-\frac{\partial\tilde{A}}{\partial\alpha}\Big|_{\alpha=0}q. \tag{A.6}$$

$$\mathscr{O}(z\bar{z}):\mathscr{L}y_{1100}=-B(q,\bar{q}). \tag{A.7}$$

$$\mathscr{O}(z^2\bar{z}):(\mathscr{L}-i\omega)y_{2100}=-f_2q-B(q,y_{1100})-B(\bar{q},y_{2000})-\frac{1}{2}C(q,q,\bar{q}). \tag{A.8}$$

Note that the operators $y_{i,j,k,l}$ represents the coefficient of the term $z^i\bar{z}^j\alpha^k\mu^{2l}$ in the Taylor series expansion of $y(z,\bar{z},\alpha,\mu^2)$. Eqs.(A.2, A.3, A.4 and A.7) are solvable by inverse

operations while Eqs.(A.5, A.6, and A.8) can be solved using the adjoint p. Note that $y_{0010} = 0$, $y_{0011} = 0$ in this case and the expressions f_1, f_2 and f_3 are easily obtained.

A.2 Complex nonlinear coefficients of the CGL

For $\tilde{p} = 1$, w have the following coefficients:

$$\Omega = \Omega_r + i\Omega_i \tag{A.9}$$

with

$$\begin{aligned}\Omega_r = -\tau\omega_r + \frac{\varepsilon(-2b\varepsilon\omega_r - 2\omega_r\omega_i)}{2\left[(b^2\varepsilon^2 + 2b\varepsilon\omega_i + \omega_i^2 - \omega_r^2)^2 + (-2b\varepsilon\omega_r - 2\omega_r\omega_i)^2\right]} \\ \Omega_i = -\frac{1}{2} - \tau\omega_i + \\ \frac{\varepsilon(b^2\varepsilon^2 + 2b\varepsilon\omega_i + \omega_i^2 - \omega_r^2)}{2\left[(b^2\varepsilon^2 + 2b\varepsilon\omega_i + \omega_i^2 - \omega_r^2)^2 + (-2b\varepsilon\omega_r - 2\omega_r\omega_i)^2\right]}\end{aligned} \tag{A.10}$$

Using these equations, the nonlinear coefficient Q can be written as

$$Q_r = \frac{\Omega_r}{2|\Omega|^2} \tag{A.11}$$

$$Q_i = \frac{-\Omega_i}{2|\Omega|^2} \tag{A.12}$$

The components of the complex number η can be expressed as

$$\eta_r = \frac{\varepsilon(\varepsilon b + \omega_i)(b^2\varepsilon^2 + 2b\varepsilon\omega_i + \omega_i^2 - 3\omega_r^2)}{(b^2\varepsilon^2 + 2b\varepsilon\omega_i + \omega_i^2 + \omega_r^2)^3} \tag{A.13}$$

$$\eta_i = \frac{\varepsilon\omega_r(3b^2\varepsilon^2 + 6b\varepsilon\omega_i + 3\omega_i^2 - \omega_r^2)}{(b^2\varepsilon^2 + 2b\varepsilon\omega_i + \omega_i^2 + \omega_r^2)^3} \tag{A.14}$$

These equations can be used to simplify the expression of P as follows:

$$P = 4Q^3k^2(\tau + \eta_r + i\eta_i) - Q \tag{A.15}$$

from which we obtain the components P_r and P_i:

$$P_r = \left[(\tau + \eta_r)(-12Q_rQ_i^2 + 4Q_r^3) - \eta_i(-4Q_i^3 + 12Q_r^2Q_i)\right]k^2 - Q_r \tag{A.16}$$

$$P_i = \left[(\tau + \eta_r)(12Q_r^2Q_i - 4Q_i^3) + \eta_i(-12Q_rQ_i^2 + 4Q_r^3)\right]k^2 - Q_i \tag{A.17}$$

Appendix B

Notations for function spaces

The following are some notations for function spaces used in some sections of this thesis:

— $\mathscr{C}^2(\Omega, \mathbb{C}^3)$ represents the space of twice continuously differentiable complex-valued vector functions on Ω, whose first derivative with respect to x vanish at $x = 0$ and $x = \ell$. On this space we define a norm

$$||\psi|| = \left(\frac{1}{\kappa} \int_\Omega \sum_{|j|\leq 2} |D^j \psi|^2 dx \right)^{\frac{1}{2}}.$$

where $\kappa = 1 + k^2 + k^4$, $\kappa > 0$, and D^j, $|j| \leq 2$, is the distributive derivative operator.

— $H^2(\Omega)$ is a second order Sobolev space in $L^2(\Omega)$ with the inner product $\langle U, V \rangle_{H^2} = \frac{1}{\kappa} \sum_{|j|\leq 2} \langle D^j U, D^j V \rangle_{L^2}$. So $H^2(\Omega)$ is the completion of $\mathscr{C}^2(\Omega, \mathbb{C}^3)$ under its associated norm.

— $H^1(\Omega)$ is the first order Sobolev space in $L^2(\Omega)$ with inner product $\langle U, V \rangle = \sum_{|j|\leq 1} \langle D^j U, D^j V \rangle$.

— $L^2(\Omega)$ is the space of complex-valued square-integrable functions on Ω with the scalar product $\langle f, g \rangle_{L^2} = \sum_{i=1}^3 \int_\Omega \bar{f}_i(x) g_i(x) dx$.